Department of Precision and Microsystems Engineering

Dynamics of a machine tool cross-slide

Milan Vermeulen

Report no : 2020-22
Coach : Dr. G. J. Verbiest
Professor : Prof. Dr. P. G. Steeneken
Specialisation : Engineering Dynamics
Type of report : M. Sc. Thesis
Date : July 2020

Dynamics of a machine tool cross-slide

M. P. Vermeulen

M.Sc. Thesis

TU Delft

Dynamics of a machine tool cross-slide

by

M. P. Vermeulen

to obtain the degree of Master of Science
at the Delft University of Technology,
to be defended publicly on Wednesday July 29, 2020 at 14:00 PM.

Student number:	4368541
Project duration:	September 1, 2019 – July 29, 2020
Thesis committee:	Prof. Dr. P. G. Steeneken
	Dr. G. J. Verbiest
	Dr. S. H. HosseinNia
	Ir. B. De Wolf
	Ir. B. De Veer

An electronic version of this thesis is available at http://repository.tudelft.nl/.

TU Delft

Preface

When I started my bachelor in mechanical engineering, already six years ago, one of the first things I learned was how to use a conventional turning machine. Since then I have always been fascinated by the great possibilities these machines offer to create complex (cylindrical) metal parts with micrometer accuracy.

Therefore, it was an honour to perform my master project within Hembrug Machine Tools, a company in Haarlem manufacturing CNC controlled hard turning machines based on hydrostatic bearings. For a full year I studied, modeled and optimised the dynamic behaviour of the slides assembly.

I would like to express my gratitude to all Hembrug staff for their support during my thesis project, especially my daily supervisor Ir. Bart de Wolf. Also I would like to thank Dr. Gerard Verbiest for his patience advice and guidance through the research process.

M. P. Vermeulen
Delft, July 2020

Abstract

Within a great variety in high tech industry there is an increasing demand for complex shaped turning workpieces with diameters up to a meter and accuracy within microns. Examples are bearings in off-shore wind energy and high precision applications. For the production of these parts CNC controlled turning machines are used. A motorized spindle rotates a clamped workpiece that gets shaped by a machine tool. The cutting tool is placed on top of two stacked ball-screw drives. The ball-screw drives allow for two translational degrees of freedom of the machine tool.

This thesis is focused on the dynamics of the stacked ball-screw drives, the so called cross-slides. First, the relevant eigenfrequencies are measured and simulated. Based on the eigenfrequencies, plant transfer functions are determined. When implementing the control elements, the closed loop behaviour has been simulated and compared with experimental data.

The influence of disturbances, for example non-stationary cutting forces, has been studied. Also, discrepancy of movement of the slides with respect to movement of the machine tool has been characterized with frequency dependence. It has been measured experimentally with multiple accelerometers at different positions. It has also been simulated using dynamic substructering, modelling the ball-screw drive partly with analytical expressions and partly with a dynamic finite element model.

With all the gained knowledge a design cycle of optimal (stacked) ball-screw drives design has been proposed. The design cycle allows for both geometrical changes as well as for the selection of varies control strategies. Using the cycle several designs have been created, with the goal to find a design with maximised closed loop position control usable frequency bandwidth. In the x direction an increase from 40 to 110 Hz was realized, in the z-direction an increase from 50 to 90 Hz was realized. Also, the influence of design changes on the disturbance response and the costs have been indicated. When selecting specific requirements the proposed design cycle could be used for optimal design.

Contents

1

Introduction

Within a great variety of industries there is a demand for turned workpieces, with large diameter and length in the order of a meter and tolerances within microns. Examples are bearings in offshore wind energy and high precision applications. The company Hembrug Machine Tools in Haarlem manufactures hard turning machines based on hydrostatic bearings. A workpiece is clamped in the machine and rotated by a motorized spindle. The workpiece gets shaped by a turning tool. The turning tool typically has two controllable degrees of freedom. One radial degree of freedom (x-direction) and one axial degree of freedom (z-direction) with respect to the clamped (cylindrical) workpiece. These degrees of freedom are provided by two slides, orientated orthogonal to each other. Each slide is supported by two guiding rails with hydrostatic bearings. A picture of a machine is shown in fig. 1.1. Besides machines with a horizonal orientation of the workpiece also a vertical orientation is possible. This concept is mainly applied for larger diameters. The machines are Computer Numerically Controlled. (CNC)

Figure 1.1: A general overview of a horizontal turning machine from the company Hembrug.

A general layout of the two slides including the turning tool, tool changer and slide assembly is shown in fig. 1.2 for a Hembrug 100 CNC. The 100 CNC is a popular machine from the company Hembrug. The subassembly shown in fig. 1.2 is attached to a large block of granite. On the same block of granite the spindle is attached. When modelling the machine, this block of granite will be considered as a fixed world, suspended by rubber blocks in a frame. The suspension prevents outside vibrations entering the assembly, which allows for assuming that forces either come from the the material turning tool contact, servo motors, friction or gravity. The z-guiding is mounted to the granite. The z-slide is connected to the z-guiding by hydrostatic bearings. Its position (in z-direction) is controlled by a ball screw. On one end the screw is connected to a servo motor, along its length the screw is connected with the slide via a ball screw nut. To eliminate play, there is a preload between the ballscrew and nut, causing slight hysteresis. Perpendicular to the z-slide the x-guiding is attached. The x-slide is connected to

the x-guiding by hydrostatic bearings, similar to the connection of the z-slide to the z-guiding. The two guidings allow for two controllable degrees of freedom. Via a number of components, the turning tool is connected to the x-slide. The changer disk allows for mounting up to 16 different turning tools. When rotating the disk, different turning tools are brought into position for the turning process. Rotating the disk only occurs when the tool is out of contact with the workpiece. A hirth coupling allows for a stiff and precise connection between the changer disk and changer block and blocks rotation of the changer disk during turning operation.

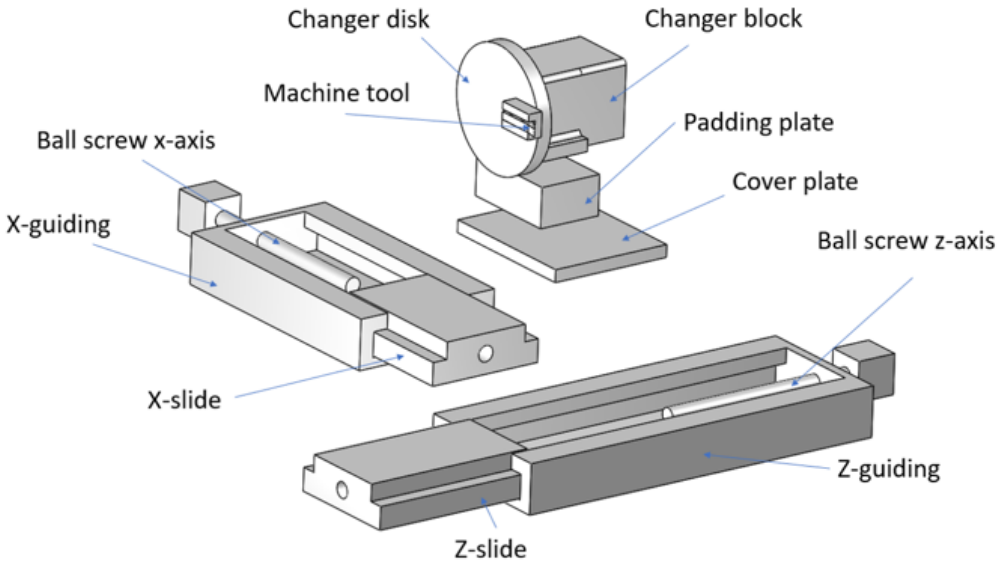

Figure 1.2: A general layout of the two slides including a turning tool, toolholder and ball screws.[12]

Not shown in figure 1.2 is the measurement system, which consists of two linear encoders and two rotary encoders. The measurement system measures four values, which are the position of the z-slide with respect to the z-guiding, the position of the x-slide with respect to the x-guiding and the rotational speed of both motor shafts. This means that many deflections can not be detected by the measurement system. Also not shown in fig. 1.2 is the weight compensation mechanism to balance gravity force, only applied when the block of granite is orientated under a nonzero angle with respect to the ground. Each axis is controlled separately using the Siemens© Sinumerik 840D sl control package. The control scheme is shown in fig. 1.3. [28] The control consists of two main feedback loops. A proportional integral controlled feedback loop that controls the speed of the motor shaft and a proportional controlled feedback loop that controls the position of the slide.

This chapter consists of 8 paragraphs. The first paragraph is devoted to the current understanding of turning tool dynamics. Paragraphs 2-5 is devoted to general modelling techniques. It starts with the determination of hydrostatic damping and stiffness, allowing for the determination of rigid body modes (vibration type 1) and eigenmodes (vibration type 2). (Later in the thesis the machine will be modelled as pieces of material connected via springs and dampers representing the hydrostatic bearings. This allows for the determination of rigid body modes and eigenmodes.) In paragraph 5 the concept of a transfer function is introduced. Paragraphs 6-8 are devoted to turning machine specific modelling. It starts with modelling the cutting forces, it introduces ball screw drive dynamics and it contains a classification of vibrations that can happen in machine tool structures, namely free, forced and self-exited (chatter) vibrations. Also, it introduces ball screw drive load side disturbance response. In the second chapter the machine will theoretically be modelled using the techniques described in chapter one. In the third chapter the execution of experimental results and its comparison with theoretical data will be given. In chapter 4 the gained knowledge will be used to formulate a design cycle that can be used for the optimisation and evaluation of ball-screw drives design.

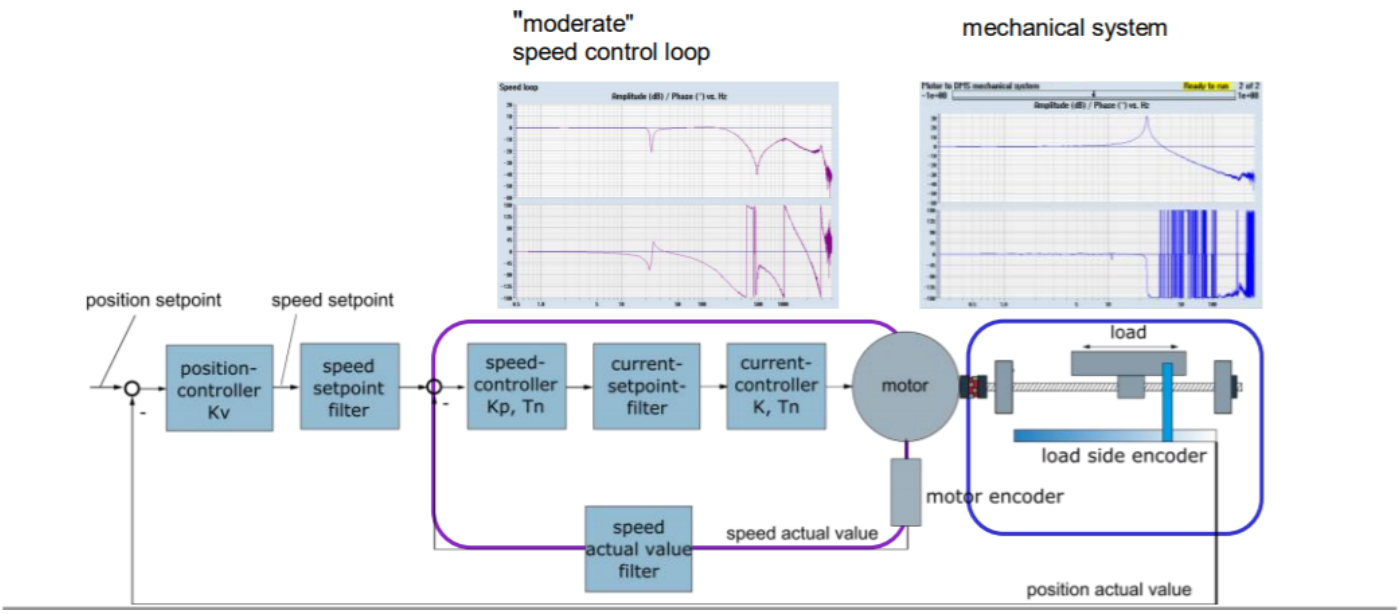

Figure 1.3: Siemens© Sinumerik 840D sl control scheme. The figure consists of two feedback loops. A third feedback loop, used for current control (capturing the current controller and the motor), is not shown in the figure.

1.1. Current understanding of turning tool dynamics

When designing a new turning machine, the full dynamics are not known until the machine has been built. This results in limited frequency bands for which motor torque can be transferred to the turning tool position, due to a lack of phase margin or gain margin. A lack of phase margin accounts for a delay between actual value and setpoint value. A lack of gain margin accounts for a decreased amplitude in actual value with respect to setpoint value. Also, it is unknown if the response measured at the linear encoders is a good representation of the turning tool position. Similarly, the (anti-)resonance frequencies and corresponding eigenmodes and damping ratio's are not known until building the machine has been built. It is a hypotheses that knowledge allows for redesigning the turning machine to maximise the frequency bands for which motor torque can be transferred to the turning tool position. Furthermore cutting parameters are currently usually optimised in a trial and error fashion. Typically, the frequency of the spindle and higher orders are seen as a variation in cutting force. Therefore, it is important to mismatch spindle frequencies and its higher orders with resonance frequencies. The first step is to get a better understanding of the turning machine dynamics. This allows for optimal design with maximised usable frequency bands, disturbances with minimal influence and knowledge about the discrepancy between movement of the slide and movement of the turning tool as a final goal.

1.2. Modelling hydrostatic damping and stiffness

A hydrostatic bearing consists of two surfaces in front of each other with a continuous volume flow of pressurized oil. Perpendicular (out of plane) to the surface the bearings experience both damping and stiffness. When the surfaces slide along each other (in plane), only damping is experienced. Around the edges of one of the bearing planes there is a wall allowing for a small gap with respect to the other bearing plane. A cross sectional view of a hydrostatic bearing is shown in fig. 1.4. A three dimensional exploded view of a hydrostatic bearing is shown in fig. 1.5. Fig. 1.6 provides hydrostatic bearing dimensions. The highest pressure in the system is the pump pressure. With a pressure control system the pump pressure is reduced to a lower value. It is assumed that all wall dimensions are much larger than the gap height. The non-linearity in of the pressure distribution in the gap is neglected.

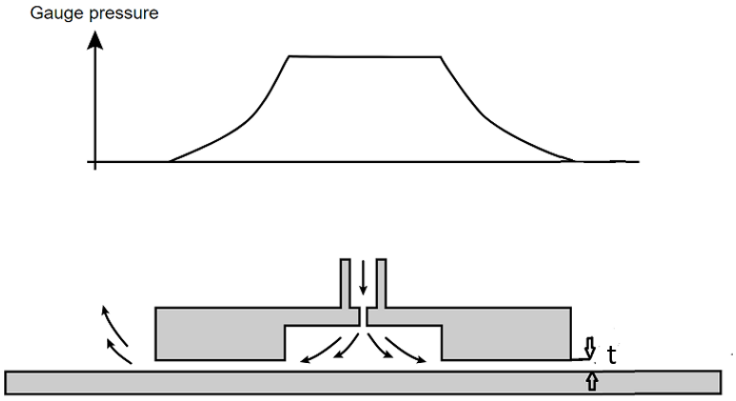

Figure 1.4: A cross sectional view of a hydrostatic bearing, including a typical pressure distribution. The arrows indicate the flow direction.[4]

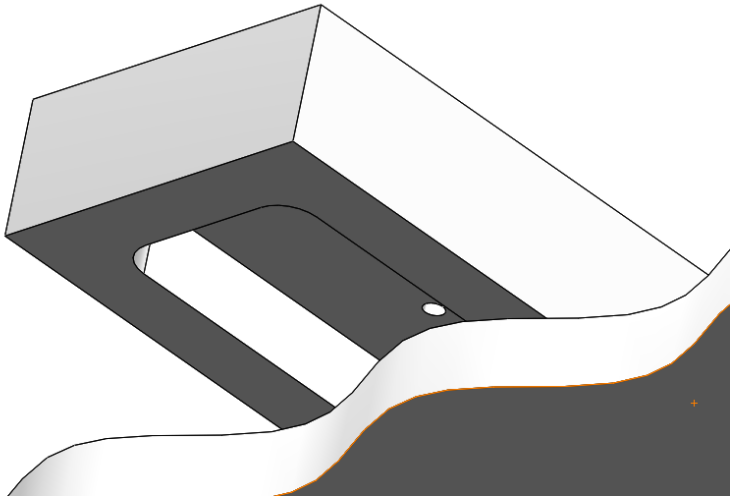

Figure 1.5: A three dimensional exploded view of a hydrostatic bearing.

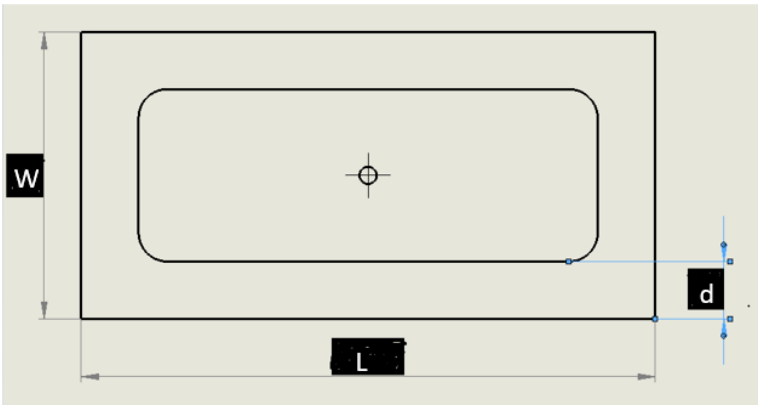

Figure 1.6: A two dimensional model showing hydrostatic bearing dimensions. Typical values for W and L are in the order of 0.1 m and typical dimensions for d are in the order of 0.01 m.

The following parameters describe the geometry and the fluid flow of a hydrostatic bearing (the recess pressure describes the highest pressure in the bearing) as indicated in fig. 1.4 and fig. 1.6:

bearing width	W	[m]
bearing length	L	[m]
wall tickness	d	[m]
gap heigth	t	[m]
pump pressure	P_p	[Pa]
pressure ratio	β	[-]
viscosity	η	[Pas]
recess pressure	$R_p = p_p{}^*\beta$	[Pa]

Based on these numbers additional information about the bearings can be determined, namely the effective area (A_e) eq. 1.1, the nominal bearing force (F) eq. 1.2, the outflow length (L_{of}) eq. 1.3, the outflow resistance (R) eq. 1.4, the volume flow (q) eq. 1.5, out of plane stiffness (λ) eq. 1.6, out of plane damping coefficient eq. (C_{oop}) 1.7 and the in plane damping coefficient eq. (C_{ip}) 1.8. [25]

$$A_e = (L-d)*(b-d) \quad [m^2] \tag{1.1}$$

$$F = R_p * A_e \quad [N] \tag{1.2}$$

$$L_{of} = 2L + 2W - 4d \quad [m] \tag{1.3}$$

$$R = \frac{12\eta d}{L_{of} t^3} \quad [\frac{Pa\,s}{m^3}] \tag{1.4}$$

$$q = \frac{R_p}{R} \quad [m^3/s] \tag{1.5}$$

$$\lambda = 3\frac{F}{t}(1-\beta) \quad [N/m] \tag{1.6}$$

$$C_{oop} = A_e^2 \frac{P_p}{q}\beta(1-\beta) \quad [Ns/m] \tag{1.7}$$

$$C_{ip} = \frac{2Ld + 2(W-2d)d}{t}\eta \quad [Ns/m] \tag{1.8}$$

An important advantage of hydrostatic bearings in the absence of sliding friction.

1.3. Rigid body dynamics

One way of modelling the system shown in figure 1.2 is to consider the hydrostatic bearings as combined springs and dampers and considering the other parts as rigid bodies. This means there are two rigid bodies, of which one is connected to the fixed world, each body having 6 degrees of freedom. The time responses of these bodies can be calculated using Lagrange dynamics [23], starting with the calculation of the Lagrangian in eq. (1.9)

$$L_i = \frac{d}{dt}(\frac{\partial T}{\partial \dot{x}_i}) - \frac{\partial T}{\partial x_i} + \frac{\partial V}{\partial x_i} - Q_i \tag{1.9}$$

i=1...n n number of degrees of freedom
T=kinetic energy
V=potential energy
Q=non-conservative forces (including damping forces)

Mass (M), damping (C) and stiffness (K) matrices can be calculated using eq. (1.10). Each Lagrange equation provides information for one line in the mass, damping and stiffness matrices. The mass, damping and stiffness matrices are therefore of square size, equaling the number of degrees of freedom. The matrices are calculated around the equilibrium positions, meaning that $\ddot{x} = 0, \quad \dot{x} = 0 \quad x = x_{eq}$.

$$M = \frac{\partial L_i}{\partial \ddot{x}_j} \qquad C = \frac{\partial L_i}{\partial \dot{x}_j} \qquad K = \frac{\partial L_i}{\partial x_j} \tag{1.10}$$

j=1...n n number of degrees of freedom
Given the mass, damping and stiffness matrices, the corresponding vector of eigenfrequencies can be calculated using eq. (1.11).

$$\mathrm{DET}(K - \omega^2 M) = 0 \tag{1.11}$$

Each eigenfrequency has a corresponding mode shape vector q_i, which can be calculated using eq. (1.12) .

$$(K - \omega_i^2 M) q_i = 0 \tag{1.12}$$

The mode shape vectors can be assembled in a matrix. The first column in the mode shape matrix represents the mode shape corresponding to the lowest eigenfrequency and so on, as shown in eq. (1.13).

$$Q = [q_1 q_2 \ldots] \tag{1.13}$$

When calculating the time response the set of differential equations in eq. (1.14) has to be solved, with f the vector of external forces.

$$M\ddot{x} + C\dot{x} + Kx = f \tag{1.14}$$

Eq. (1.14) is a set of coupled differential equations. When solving analytical, a common approach is to decouple the equations, by rewriting the set of differential equations in normal coordinates, shown as a vector η as shown in eq. (1.15).

$$(Q^T M Q)\ddot{\eta} + Q^T C Q \dot{\eta} + Q^T K Q \eta = Q^T f \tag{1.15}$$

The result is a set of uncoupled second order differential equations in normal coordinates, which allow for calculating the time responses in normal coordinates. Using eq. (1.16) below the time responses can be calculated in generalized coordinates.

$$X = Q\eta \tag{1.16}$$

The larger the number of degrees of freedom, the larger the set of equations becomes. It is common to solve the problem numerically with a software package instead of analytically.

1.4. Vibration due to material elasticity

Later in this thesis deflection of the slides assembly due to finite material stiffness will be modeled using software. To illustrate the principles behind these models a classical one dimensional Euler-Bernoulli beam will be studied. The beam has boundary conditions at two sides.

1.4.1. Free vibrations

Free structural vibrations occur when a structure experiences an impact force, for example an impulse. For a one dimensional Euler-Bernoulli beam the equation to be solved (applying boundary conditions) is given by Euler [17] and shown in eq. (1.17).

$$EI\frac{\partial^4 v}{\partial x^4} + \mu\frac{\partial^2 v}{\partial t^2} = 0 \tag{1.17}$$

With E the Youngs modulus, I, the cross sectional moment of inertia, μ the mass per unit length, v(x,t) is the deflection of the beam at position x and time t. Any damping, both internal and external is neglected.

1.4.2. Forced vibrations

When a structure experiences a driving force, forced vibrations occur. The formula to be solved is given by Abu-Hilal [7] and shown in eq. (1.18)

$$EI\frac{\partial^4 v}{\partial x^4} + \mu\frac{\partial^2 v}{\partial t^2} = p(x,t) \tag{1.18}$$

p(x,t) denotes the load per unit length at position x and time t. Any damping, both internal and external is neglected.

For a given p(x,t) the response v(x,t) can be calculated using boundary conditions, as discussed in the next subsection. In real life, elastic bodies are three dimensional and can have complex geometrical shapes and boundary conditions. In these cases it is preferred to use a software package to calculate responses instead of analytical solutions.

1.4.3. Boundary conditions

When solving eq. (1.17) and eq. (1.18) boundary conditions have to be applied. Euler [17] provides a table of common boundary conditions, which can be aplied for x=0 or x=L. Selected boundary conditions are shown in eq. (1.19) - (1.23). The ±sign in eq. (1.22) and eq. (1.23) denotes the the left side, respectively the right side of the beam.

$$\text{free end} \qquad EI\frac{\partial^2 v(x,t)}{\partial x^2} = 0 \quad and \quad EI\frac{\partial^3 v(x,t)}{\partial x^3} = 0 \tag{1.19}$$

$$\text{supported end} \qquad v(x,t) = 0 \quad and \quad EI\frac{\partial^2 v(x,t)}{\partial x^2} = 0 \tag{1.20}$$

$$\text{clamped end} \qquad v(x,t) = 0 \quad and \quad EI\frac{\partial v(x,t)}{\partial x} = 0 \tag{1.21}$$

$$\text{linear spring} \qquad EI\frac{\partial^2 v(x,t)}{\partial x^2} = 0 \quad and \quad EI\frac{\partial^3 v(x,t)}{\partial x^3} = \pm k v(x,t) \tag{1.22}$$

$$\text{torsional spring} \qquad EI\frac{\partial^3 v(x,t)}{\partial x^3} = 0 \quad and \quad EI\frac{\partial^2 v(x,t)}{\partial x^2} = \pm k\frac{\partial v(x,t)}{\partial x} \tag{1.23}$$

1.4.4. Solving vibration equations

When solving eq. (1.17) and eq. (1.18) an infinite number of solutions exists. Each solution represents an eigenmode of the structure. An eigenmode is a natural characteristic of the structure representing the structure's deformation shape at certain resonant frequencies. An eigenmode has no longer a time dependency because it represents the maximum positions reached by a vibrating structure, it provides no information when these values are reached. The sum of all eigenmodes (including a weight factor to each eigenmode) represents the response of the structure. As an example the first four eigenmodes of a beam supported by linear springs at each end will be studied, see fig. 1.7. The boundary conditions given in eq. 1.2 will be used. The first four normal modes are shown in 1.8, given by Euler [17]. The values used are EI = 8000 Nm^2, μ = 3000 kg/m, L = 1 m and k = 1000 N/m (both ends are supported by a linear spring).

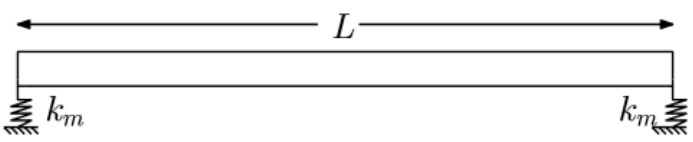

Figure 1.7: A model of a beam supported by linear springs at each end.

.

When studying a specific mode shape, points with zero amplitude and points with maximum amplitude can be found. (With respect to the undeformed shape of the structure.) The points with zero amplitude are called a node, the points with maximum amplitude are called an antinode. The values

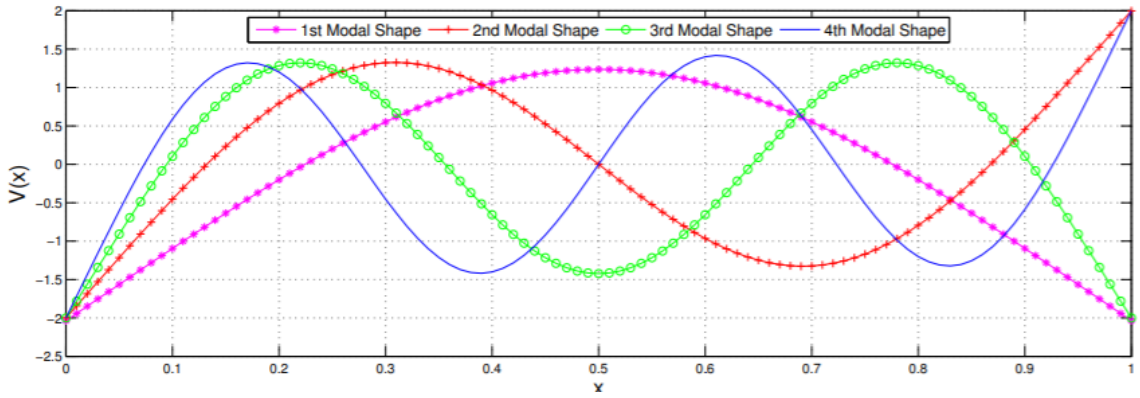

Figure 1.8: The first four modeshapes of an Euler Bernoulli beam supported by linear springs on both ends, with x the axial position and V(x) the lateral deflection [15]. The modes are scaled in such a way that the maximum deviation from the equilibrium position is 2 [-] for all mode shapes.

of V(x) are arbitrary, the resultant deflection of a vibrating beam is a linear combination of all vibration modes.

1.5. Transfer function

For a better understanding of the relationship between the input u(t) of a dynamical system, for example force, torque or current and output y(t), for example position, velocity or acceleration the concept of a transfer function is very powerfull. [3] Calculating a transfer function starts with a transformation to the Laplace domain. The transformation from a function in the time domain f(t) to a function in the Laplace domain F(s) is given in eq. (1.24).

$$F(s) = \int_0^\infty e^{-st} f(t) dt \tag{1.24}$$

Given the output function Y(s) and the input function U(s) (both in the Laplace domain) the transfer function can be calculated using eq. (1.25).

$$H(s) = \frac{Y(s)}{U(s)} \tag{1.25}$$

For a one dimensional mass spring damper as shown in fig. 1.9 the transfer function between the input force F and output displacement x is known exactly and given in eq. (1.26). Eq. (1.26) is a transfer function describing single input, single output.

$$H(s) = \frac{1}{ms^2 + cs + k} \tag{1.26}$$

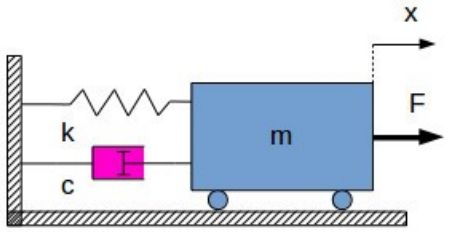

Figure 1.9: A graphical representation of a single degree of freedom mass spring damper system representing rigid body motion.

For a single degree of freedom the eigenfrequency ω_n [hz] and the damping ratio ζ [-] is given in eq. (1.27).

$$\omega_n = \frac{1}{2 * \pi}\sqrt{\frac{k}{m}} \qquad \zeta = \frac{c}{2\sqrt{km}} \tag{1.27}$$

Given a transfer function in the Laplace domain a bode plot can be constructed. The construction of a bode plot based on a transfer function is outside the scope of this thesis. The bode plot for a single degree of freedom system is shown in fig. 1.10.

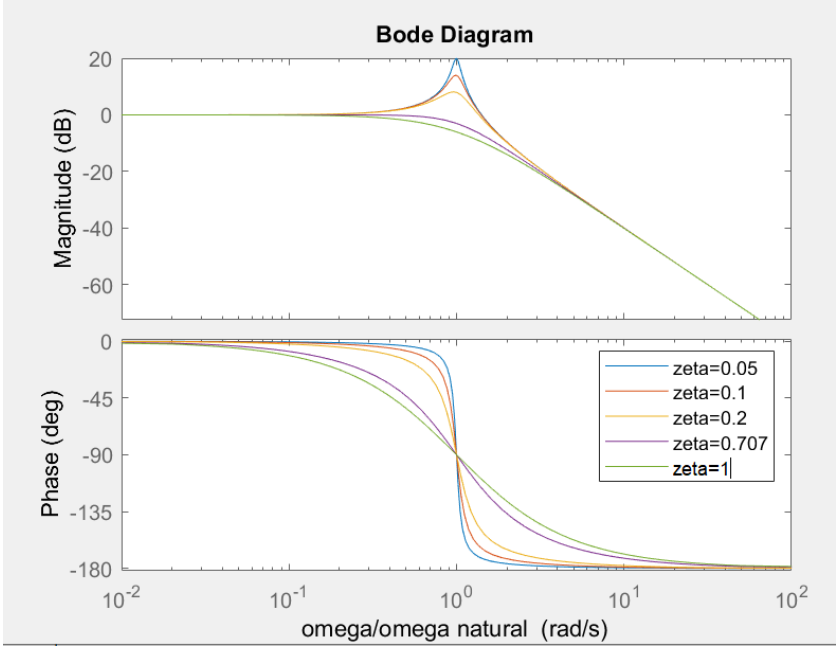

Figure 1.10: A bode plot for the one degree of freedom mass spring damper problem. The magnitude diagram shows a peak for low damping ratio's at the natural frequency. Around the natural frequency the phase drops from 0 towards minus 180 degrees. The lower zeta, the higher the peak in gain. For a multiple degree of freedom system the maximum number of peaks that can be found equals the number of degree of freedom. For multiple degree of freedom systems, each peak has it's own damping ratio.

For more complex transfer functions, exact (analytical) transfer functions are no longer available. Transfer functions can be estimated using algorithms, which require input and output data, for example in the time or the frequency domain. The input and output data can be determined either experimentally, as discussed later, or by Finite Element simulations using a CAD model. Matlab© has coded a nonlinear least-squares search method for estimating transfer functions in the s-domain. [5] The function is called tfest. By default the algorithm uses an Instrument Variable (IV) method to initialize the estimable variables.

In cases of multiple input multiple output (MIMO) a matrix of transfer functions has to be described [33]. The general layout of a transfer matrix in combination with input and output data is shown in eq. (1.28). The matlab algorithm tfest is able to determine a matrix of transfer functions.

$$\text{Output vector} = \text{transfer matrix} * \text{input vector} \tag{1.28}$$

For a case of a system with two inputs (u and w), and two outputs (y and z) the transfer function is shown in eq. 1.29.

$$\begin{Bmatrix} y \\ z \end{Bmatrix} = \begin{bmatrix} G_{uy} & G_{wy} \\ G_{uz} & G_{wz} \end{bmatrix} \begin{Bmatrix} u \\ w \end{Bmatrix} \tag{1.29}$$

A graphical representation of the input and output together with the transfer functions is shown in fig. 1.11. The G matrix is a symmetric matrix. For the two dimensional case, $G_{wy} = G_{uz}$.

When assuming linear structural dynamics two main consequences apply.[33]

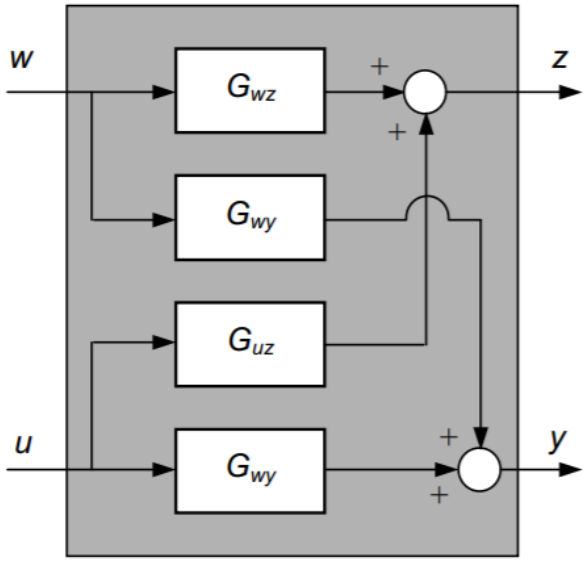

Figure 1.11: Graphical represenation of a multiple input multiple output system including cross coupling.[18]

1. Multiplying the input with a factor α, results in an output multiplied with a factor α too.
2. If two or more excitation patterns are applied simultaneously then the response thus produced will be equal to the sum of the responses caused by each excitation individual. In this case the principle of linear superposition applies.

Consequence (2) makes the experimental determination of the frequency response matrix in eq. (1.28) much easier in case of multiple inputs and outputs, since excitations do not have to be applied simultaneously and measurements do not have to be performed simultaneously.
Apart from resonance frequencies, also anti-resonance frequencies can be found in a bode plot, an example is shown in fig. 1.12.
Apart from constructing a bode plot based on a transfer function in the Laplace domain, it is also possible to apply a Fourier transform on a (transfer) function in the time domain. The Fourier transform is given in eq. (1.30). The Fourier transform returns a complex valued function with the frequency [rad/s] as its variable. Plotting its phase and magnitude versus frequency gives a bode plot.

$$F(\omega) = \frac{1}{\sqrt{2\pi}} \int_{-\infty}^{\infty} f(t) e^{-i\omega t} dt \tag{1.30}$$

A transfer function capturing just the dynamics of a structure represents the plant transfer function. The plant transfer function multiplied with the controller is called the open loop transfer function. The closed loop transfer function includes a feedback loop and is usually most interesting. An example of a typical closed loop block scheme is shown in fig. 1.13. The closed loop transfer function describes the relation from input r(s) to output y(s).

1.6. Modelling forces

As stated at the beginning of the chapter, forces come from both the servo motors as well as the turning tool - material contact.

1.6.1. Forces on the turning tool

Determining the forces is fairly complex because the chip formation process varies with different cutting parameters. It is known that the forces can be determined when the tool feed [mm / revolution], the cutting velocity (workpiece radius [mm] *rotational speed [rad/s]), the depth of the turning tool into the workpiece and the material properties (of both the workpiece material and the turning tool) are known.

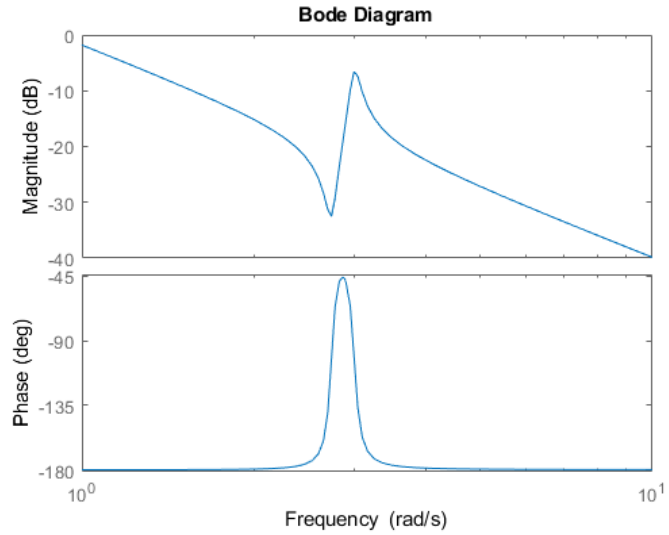

Figure 1.12: A bode plot containing one resonance and one anti-resonance frequencies. A Local maximum in the magnitude represents a resonance frequency, related to an eigenmode and eigenfrequency of the structure. A resonant frequency is related to a sudden decrease in phase. A local minimum in the magnitude represents an anti-resonance frequency, associated with a sudden increase in phase.

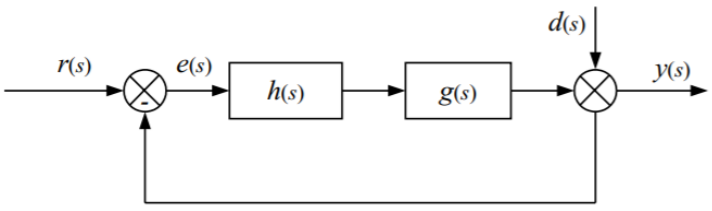

Figure 1.13: Closed loop control of a plant. The reference signal R(s) minus the actual value gives the error that should be corrected. h(s) represents the control system and g(s) represents the plant to be controlled. d(s) is a disturbance and y(s) is the system output. The disturbance d(s) can also be located at other locations, depending on the physics of the system.[9]

[22] Also the geometry of the turning tool is of influence. The relationship between these parameters and the cutting force is non-linear and relationships are often determined experimentally by performing experiments and curve fitting. [24] A graphical interpretation of the chip formation for an axial cutting process (on the opposite of radial cutting process) is shown in fig. 1.14. The net cutting force can be decomposed in a main cutting force, a radial cutting force and a feed force, as shown in fig. 1.15.

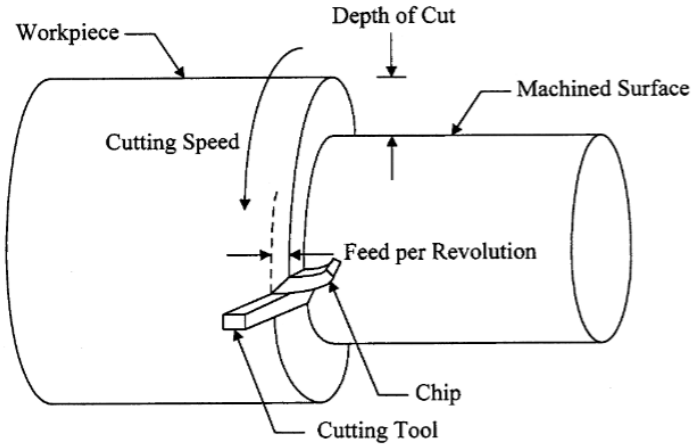

Figure 1.14: A graphical interpretation of a chip formation process, with the process parameters indicated.

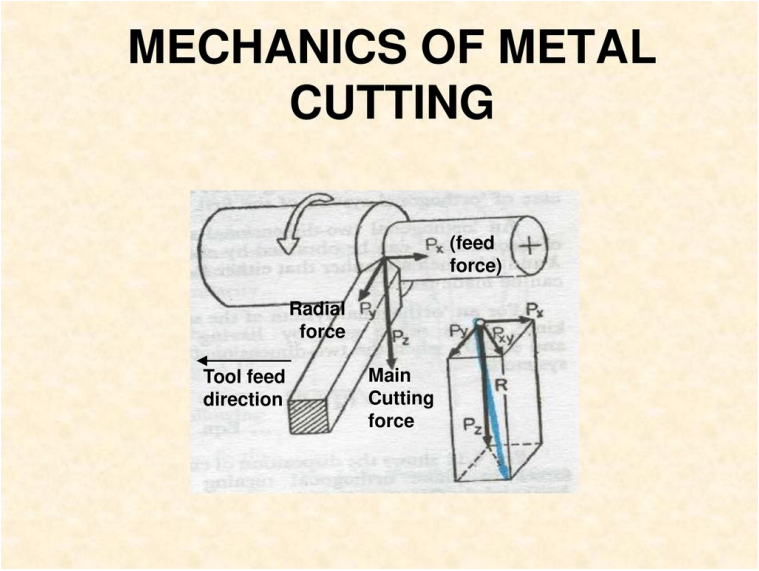

Figure 1.15: The net force (denoted as R) can be decomposed in a radial force, a feed force and an main cutting force. [2]

A common approach in determining the cutting forces is to plot the instantaneous chip area (tool feed times depth off cut) versus the net cutting force or one of its components for a given rotational speed and, a given workpiece material and a given turning tool. A typical diagram is shown in fig. 1.16.

Experiments have shown that for tool cutting edge angles around 90 degrees, the force in the non-cut direction is close to zero. (E. a. in case of an axial feed direction the radial force is close to zero and in case of a radial feed direction, the axial force is close to zero.)[1]

1.6.2. Servo motor torque

The servo motor transfers an electrical current into a torque. The relation between the electrical current and the torque is specified by the torque constant, with units [Nm/A]. Electrical current can not be applied instantaneously on a motor. An electrical motor has an electrical time constant (usually expressed in

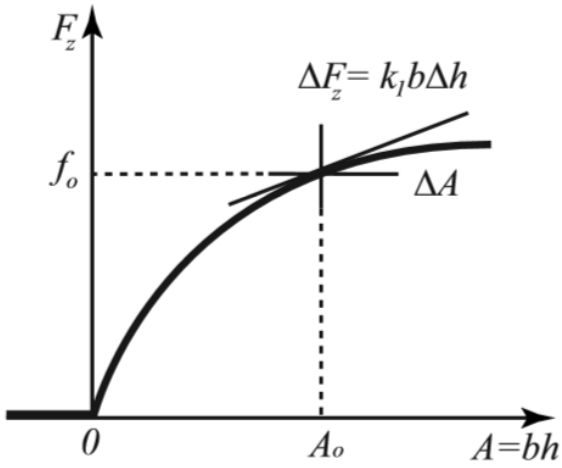

Figure 1.16: A cutting force (component) versus the instantaneous chip area. For a small variation in cutting force around a specific area, a linearization is applied by determining a value of k_1. For more accurate results, or results for a larger difference in area, a non-linear relationship for instantaneous cutting area and cutting force has to be determined [24].

milliseconds) determining how fast a current can decrease or increase. Also the current controller can not change the current instantaneously. Also, it takes a finite time before the current created in the current controller reaches the motor, due to finite cable length. However, usually the electrical time constant of the motor is the dominant factor in the electrical circuit. [29]

Another effect when applying current on an electrical motor is the effect of torque ripple, a periodic increase or decrease in torque depending on the angular position of the motor shaft. Torque ripples are caused by the physics of the motor and many solutions exist to minimize the influence the torque ripples. [6]

1.7. Dynamics of a ball screw drive

A stacking of two ball screw drives forms the basis for a slides assembly. A general model of a ball screw drive is shown in fig. 1.17. [10] The model starts with a motor. The motor is connected to the ball screw by a bellow coupling. The screw is axially fixed by a bearing. Both the motor and the bearing are connected to the side plate. (The plates at the beginning and at the end of the x- and z-guidings.) The screw is in contact with a preloaded nut allowing for linear movement of the table (slide). Sometimes there is an axially free bearing at the end of the ball screw. A ball screw drive consists of two encoders, namely a linear encoder at the table and a rotary encoder at the motor axis.

1.7.1. Transfer functions

For the determination of transfer functions the starting point is a simplified two mass model shown in fig. 1.18. [16] m_1 [kg] represents the rotary inertia I which is converted to an equivalent translating mass using eq. 1.31 with l [m] the lead of the screw.

$$m1 = I * (\frac{2\pi}{l})^2 \tag{1.31}$$

m_2 [kg] is the mass of the slide including its attached components, k [N/m] is the drive stiffness (based on the side plate, the axially fixed bearings, the screw and the stiffness of the nut) c is the viscous friction in the nut, usually estimated as a percentage of the stiffness of the nut. u is the input torque, converted to an input force based on the lead of the screw. x_1 and x_2 are shaft and table position, d_1 and d_2 are disturbances and b_1 and b_2 are viscous friction acting on the moving elements. (b_1 and b_2 are usually neglected (set to zero).)

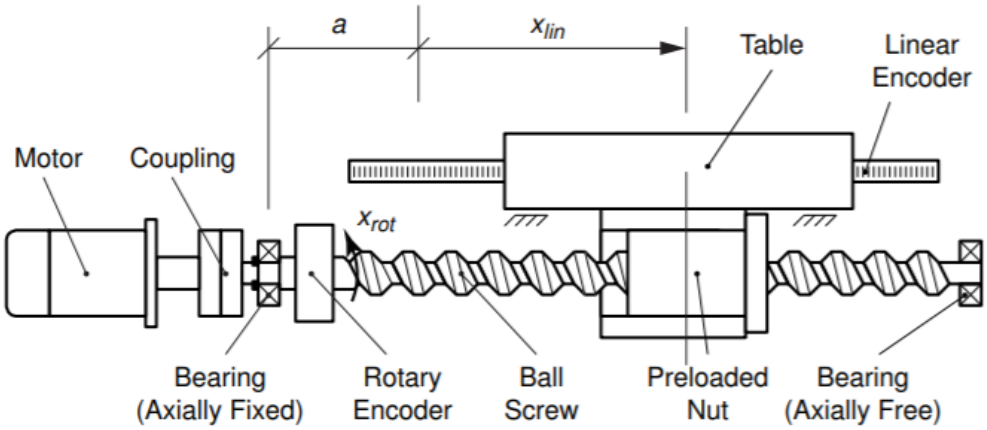

Figure 1.17: A graphical two dimensional overview of a ball screw drive.

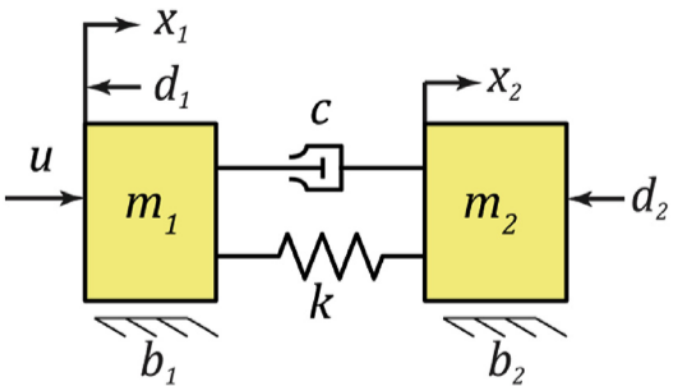

Figure 1.18: A two mass model of a ball screw drive

1.7.2. Transfer function motor torque to shaft position

The transfer function from motor torque (u) to motor shaft position (x_1)TF_{mtsp} using the two mass model is given in eq. 1.32.

$$TF_{mtsp} = \frac{(m_2 s^2 + cs + k)}{m_1 m_2 s^4 + c(m_1 + m_2)s^3 + k(m1 + m2)s^2} \tag{1.32}$$

The transfer function in eq. 1.32 contains a resonant frequency ω_r (also called structural resonance frequency) and an anti resonant frequency ω_{ar} (also called locked rotor frequency), given in eq. 1.33 and eq. 1.34.

$$\omega_r = \frac{1}{2\pi}\sqrt{\frac{k(m_1 + m_2)}{m_1 m_2}} \tag{1.33}$$

$$\omega_{ar} = \frac{1}{2\pi}\sqrt{\frac{k}{m_2}} \tag{1.34}$$

Eq. 1.32 considers only one eigenfrequency. To include also the second and third eigenfrequency (arising from torsional modes) eq. 1.32 can be rewriten and extended, as shown in eq.1.35. [11]

α_1, α_2 and α_3 represent a scalar value associated with the modeshape. ξ is the damping factor of the particular eigenfrequency and ω is the eigenfrequency [rad/s].

$$TF_{mtsp,ex} = \left(\frac{\alpha_0}{s^2} + \frac{\alpha_1}{s^2 + 2\xi_1\omega_1 s + \omega_1^2} + \frac{\alpha_2}{s^2 + 2\xi_2\omega_2 s + \omega_2^2} + \frac{\alpha_3}{s^2 + 2\xi_3\omega_3 s + \omega_3^2}\right) \tag{1.35}$$

Eq. 1.35 can also be rewritten to eq. 1.36.

$$TF_{mtsp,ex} = (TF_{mtsp} + \frac{\alpha_2}{s^2 + 2\xi_2\omega_2 s + \omega_2^2} + \frac{\alpha_3}{s^2 + 2\xi_3\omega_3 s + \omega_3^2}) \tag{1.36}$$

1.7.3. Transfer function shaft position to table position

The transfer function from motor shaft position (x_1) to table position (x_2) is given in eq. 1.37.

$$TF_{sptp} = \frac{cs + k}{m_2 s^2 + cs + k} \tag{1.37}$$

The magnitude of the transfer function in eq. 1.37 is normalized for the 0 hZ frequency, meaning that the factor converting the rotaraty motion to lineair motion is not taken into account. For the frequency domain well below the torsional mode, the magnitude of the transfer functions is approximately 0 dB. The resonance frequency in eq. 1.37 equals the anti-resonance frequency in eq. 1.32. A transfer function toward speed or acceleration instead of position can be found by multiplying eq. 1.32 or eq. 1.37 by s (for speed) or s^2 (for acceleration).

1.7.4. Limitations on mass ratio

An important parameter for a ball screw drive design is the mass ratio p. This is the ratio between the translating mass and the equivalent rotary mass (1.31). The equation for p is given in 1.38.

$$p = \frac{m_2}{m_1} \tag{1.38}$$

In previous paragraphs PI velocity control and plant transfer functions have been introduced. This allows for the determination of closed loop speed control. The maximum achievable closed loop pole damping constant is limited by p. In fig. 1.19 the root locus of the closed loop speed control is shown for two different mass ratio's. The root locus is plotted for a variable proportional control parameter. (The integral control parameter is kept constant.) In grey a small mass ratio is shown. In black a large mass ratio is shown.

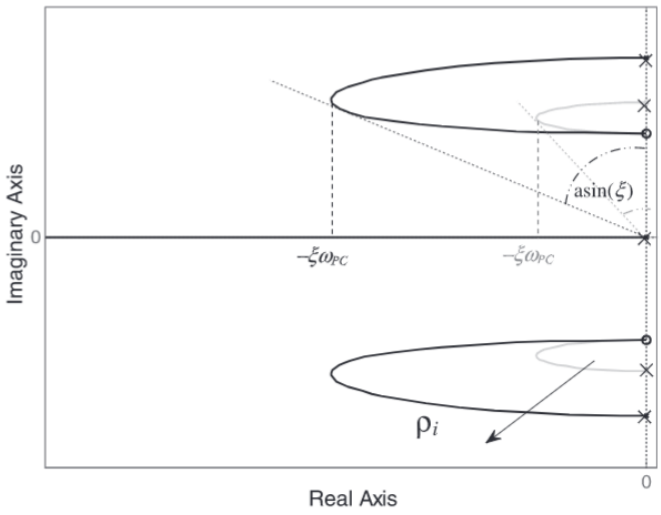

Figure 1.19: Root locus of the speed control: effect of the mass ratio on the closed loop pole damping and frequency. [13]

Well damped closed loop velocity control is required for robust control. Therefore, it is desirable to formulate a general lower bound for this ratio. In literature there is no agreement on what is an acceptable lower bound. According to [13] it should not be smaller than 0.5. According to [30] is should not be smaller that 0.1. A trade off may be made between either a large lead and a small screw diameter for well damping of closed loop poles or a small lead and a large screw diameter for high accuracy and a high locked rotor frequency. The advantages and disadvantages of a large lead and a large locked rotor frequency will be future explored in chapter 4.

1.8. Vibrations in machine (tool) structures

The cutting force, e.a. the force between turning tool and workpiece can cause three different types of vibrations. [19] Those are free, forced and self-excited vibrations, as illustrated in fig. 1.20. To provide a broad introduction into the field of turning tool vibrations all 3 vibrations will be discussed. However, for the remainder of this thesis only forced vibrations are taken into account.

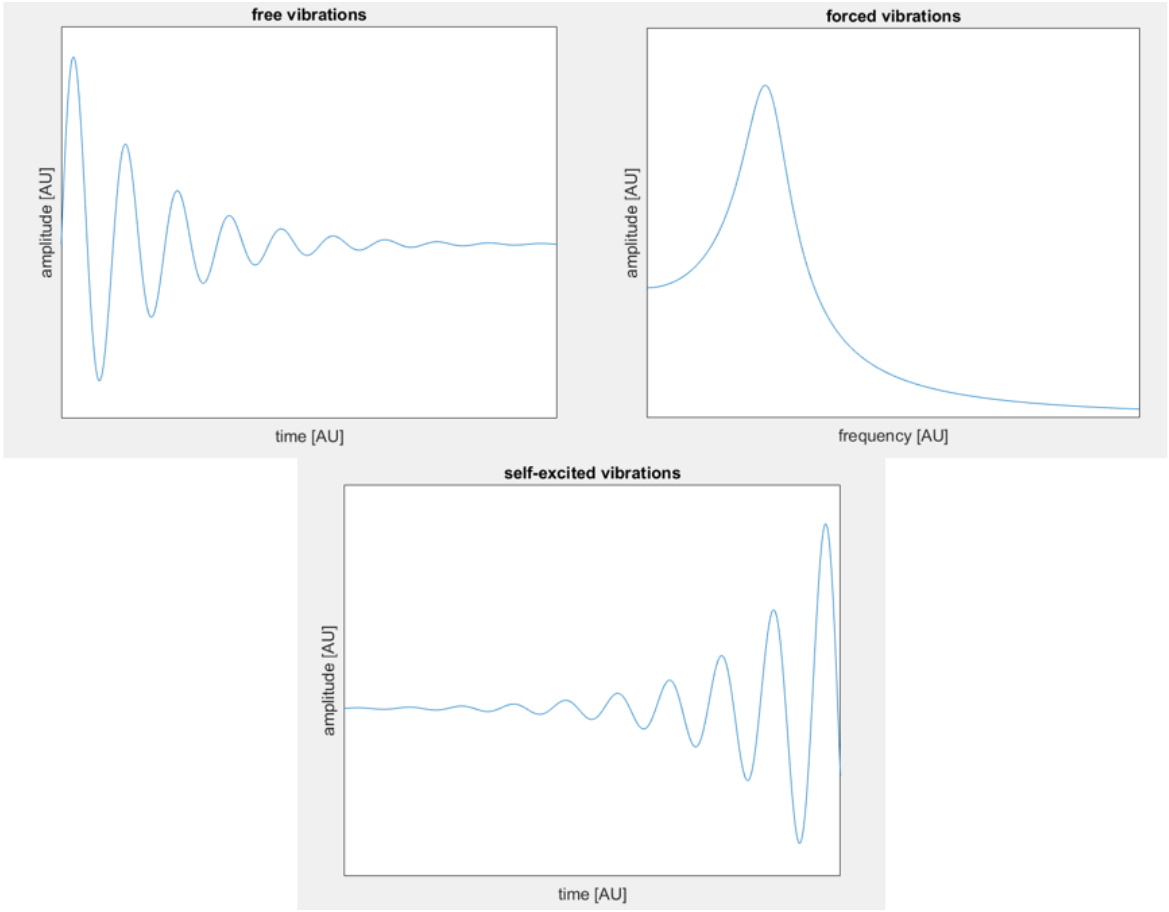

Figure 1.20: (a) free (time domain), (b) forced (frequency domain) and (c) self-excited (time domain) vibrations in a machine tool structures.

1.8.1. Free vibrations

Free vibrations occur after shock or impulse loading, for example when the turning tool strikes a hard grain. Due to damping, which is in practice always present, the amplitude decays with time. Often this type of vibration is neglected, since forced and self-excited vibrations are dominant.

1.8.2. Forced vibrations

Forced vibrations occur due to periodic excitation. The machine vibrates with the frequency of the excitation. When the excitation is close to or matches the natural frequency, the amplitude of the oscillation reaches large values in case of low damping. A common way to minimize the amplitude of free vibrations is to mismatch the eigenfrequency with the frequency of the excitation.

1.8.3. Self-excited vibrations

When the turning tool is in contact with the workpiece forces act on the turning tool. When the force on the tool is not constant, for example when the tool hits a hard grain, the tool starts vibrating with a natural frequency ω_n. The natural frequency is typically much larger than the spindle frequency. This results in a sinusoidal pattern called Outer Modulation. The next modulation, after one spindle rotation, is called Inner Modulation. [14]. A graphical interpretation of regenerative chatter for both axial and radial

turning is shown in fig. 1.21 When the phase angle is zero, as shown in fig. 1.22a, the cutting force is constant over the time. When the phase angle is nonzero, for example 0.5π (fig.1.22b) or π (fig. 1.22c), the cutting force is not constant over the time and the vibration amplitude may grow unbounded. This phenomenon is called regenerative chatter, meaning unstable turning. The phase angle β between the inner and outer modulation is a factor determining the stability. The vibration is stable if the amplitude of vibration remains bounded. The vibration is unstable if the vibration amplitude grows continuously and unbounded. A common way to start modelling regenerative chatter is to consider a rigid workpiece and a turning tool compliant in the feed direction and infinitely stiff in the plane perpendicular to the feed direction. Regenerative chatter is the relative movement between the turning tool and the workpiece. In this thesis introduction the focus will be on the displacement of the turning tool, by assuming a rigid workpiece and a compliant tool. Tool compliance can be improved by optimising the machine dynamics. The goal is optimising the machine for general purposes, not for specific workpieces. However it is known that when the workpiece has low stiffness, for example because it is thin-walled or it is long with respect to its diameter and possible only single-ended supported, workpiece deflection can cause regenerative chatter.

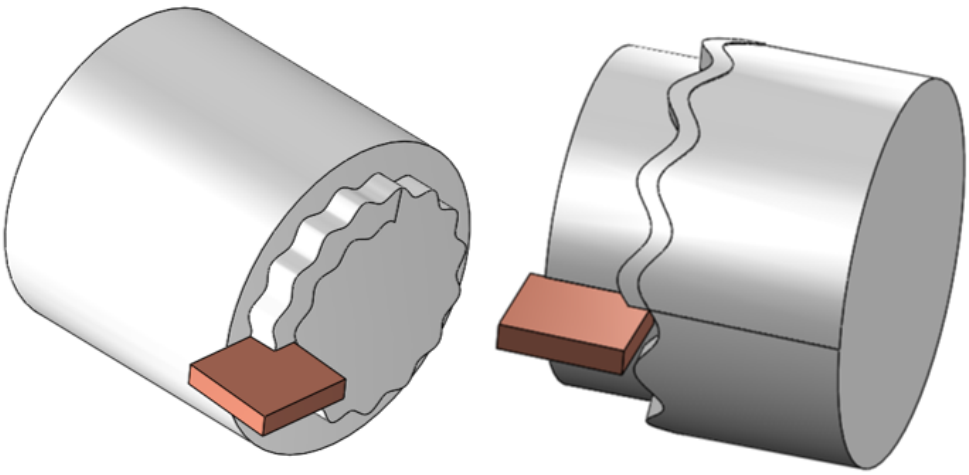

Figure 1.21: A model of a turning tool in contact with a workpiece. The direction of feed is (a) radial and (b) axial. The inner and outer modulation are both indicated.

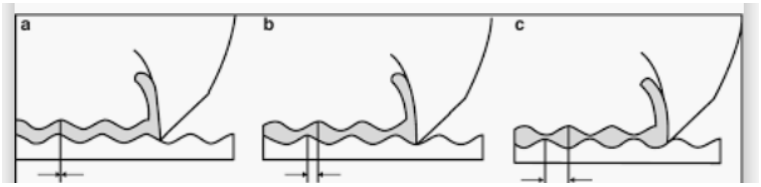

Figure 1.22: The inner and outer modulation, shown for three different phase angles, β=0, β=0.5π and β=π

A common way to model this process is to start with a classical mass spring damper approach, shown in eq. (1.39).

$$m\ddot{x} + c\dot{x} + kx = -F_x(A) \tag{1.39}$$

The next step is to look at the variation around the nominal modulation, writing the position of the turning tool in x direction as a nominal value plus a perturbation, as done in eq. (1.40).

$$x(t) = x* + \xi(t) \tag{1.40}$$

Considering a variation around a nominal position allows for calculating the variation of the chip thickness, with τ representing a time delay between the inner and outer modulation (the time of one spindle revolution), as done in eq. (1.41)

$$\Delta h = \xi(t) - \xi(t-\tau) \tag{1.41}$$

Using a linearization method to calculate the variation in cutting force based on a variation in chip thickness (eq. 1.42), allows for rewriting eq. (1.39) to eq. (1.43). k_1 is the cutting force coefficient as determined in fig. 1.16, h_0 is the nominal feed per revolution and w is the depth of cut (both indicated in fig. 1.14.)

$$\Delta F = k_1 h_0 w \Delta h \tag{1.42}$$

$$\ddot{\xi}(t) + 2\eta\omega_n\dot{\xi}(t) + \omega_n^2\xi(t) = -u(t)\frac{k_1 h_0 w}{m}(\xi(t) - \xi(t-\tau)) \tag{1.43}$$

During normal cutting conditions u(t) usually has a constant value of 1. During interrupted cutting conditions, u(t) represents a switching function, with a value of 1 when the tool is in contact with the material, and a value of zero when the tool is not in contact with the workpiece. η represents the damping ratio and ω_n the natural angular frequency. Eq. (1.43) represents a differential delay equation (DDE). Solving the equation results in either a bounded or an unbounded solution, respectively representing stable or unstable cutting. The values that can be adjusted by the operator of the machine to switch between stable and unstable cutting conditions are the feed per revolution h_0 [m], the depth of cut w and the spindle speed Ω_0. Determining the stability of a set of parameters allows for calculating a stability curves for different vales of h_0. An example is shown in fig. 1.23. [14] It should be noticed that the lines indicating the boundary between stable and unstable cutting regions remain the same shape when lowering h_0, but drop in the w direction, meaning that the value of w for which cutting is stable decreases.

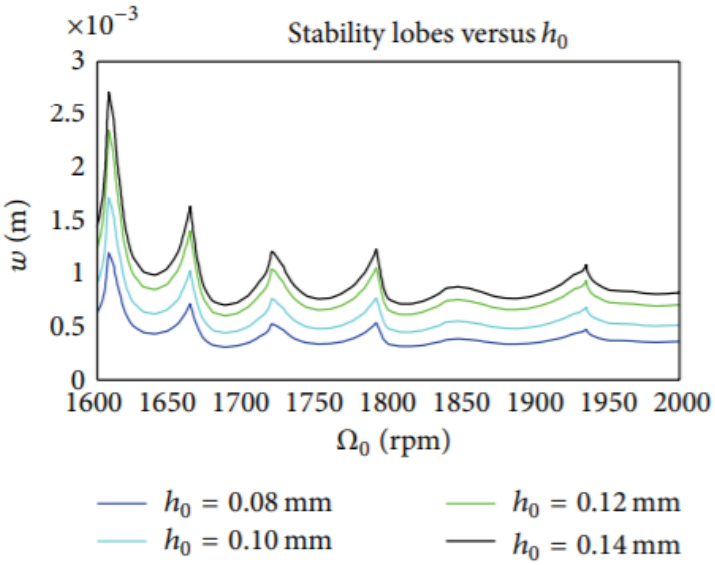

Figure 1.23: Diagram showing boundaries between stable and unstable cutting. The smaller h_0, the smaller the region for stable cutting.

Chatter is usually considered as a limitation for productivity. However, Hembrug reports also chatter problems when finish turning. Finish turning is the final step in the machine process. This can be explained by investigating fig. 1.23. The area for stable cutting gets smaller for decreasing feed rate. Little is known about the stability for very small values of h_0, which is of interest in finish turning, when h_0 can approach values of 0.01 mm. There are very few research works which considered compliance of tool–workpiece system and it is believed that the tool–workpiece compliance should always be considered to constitute a more realistic model. [27]

In real life, chatter can occur in three directions simultaneously [8], making the analysis much more complex. However, multidimensional chatter is outside the scope of this thesis.

For the remainder of this thesis, only forced vibrations will be studied.

2

Theoretical modelling

In this chapter the dynamics of the slides assembly will theoretically be modelled. The plant transfer function as well as the closed loop behaviour will be studied. The model starts with a determination of natural frequencies that can be found in the slides assembly. Consequently, an approach for dynamic substructuring will be proposed to determine a transfer function from motor torque to slide position and turning tool position. Once the open loop transfer function is known, the closed loop behaviour will be calculated. The closed loop behaviour will be studied considering usable frequency range and disturbance rejection.

2.1. Determination of natural frequencies

A model of a slides assembly has been created in SolidWorks 2019. The model has been converted to a finite element model to find its eigenfrequencies and mode shapes. The simplified model shown in fig. 1.2 is used as a base, but changes have been made to allow for extra details. Here, a trade-off has been made between accuracy of the model and the computational costs to find a solution. The model starts with a box for the z-slide. The box consists of a bottom plate, two linear guidings and two side plates, as shown in 2.1. At <confidential value> positions the slide is guided by hydrostatic bearings.

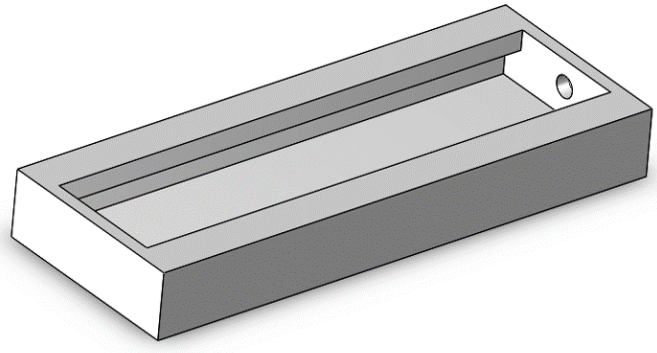

Figure 2.1: A model of the bottom plate, guidings and side plates of the z-box.

As explained in chapter one, the bottom surface of the bottom plate is fixed in the model. Each bearing related to the z-guiding has a stiffness of <confidential value> N/m and a preload of <confidential value> kN, calculated with the formulas presented in chapter one. The next step in building the assembly is to include the z-slide, shown in figure 2.2.

The slide is connected with the right side plate by a linear spring, representing the ball-screw. Modelling the screw by a linear spring has two main consequences. (1) torsional modes will not be found

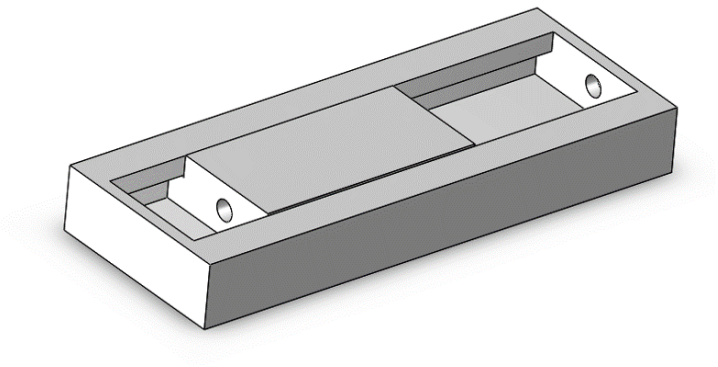

Figure 2.2: A model of the z-box and the z-slide.

(this will be discussed later) and (2) regarding axial vibrations, only the locked rotor frequency will be found and not the structural resonance frequency. The structural resonance frequency is always above the locked rotor frequency. Since the mass ratio is typically well below unity, the structural resonance frequency is close to the locked rotor frequency. Also, the mode shapes are very similar.

The stiffness of the spring is based on the bearings connecting the side plate with the screw, the screw itself and the nut connecting the slide with the screw. The next step in the assembly is to attach the x-box on the z-slide as shown in fig. 2.3. At <confidential value> locations the x-slide is guided by the x-guiding via hydrostatic bearings. Each bearing related to the x-guiding has a stiffness of <confidential value> N/m and a preload of <confidential value> Kn, calculated with the formulas in chapter one.

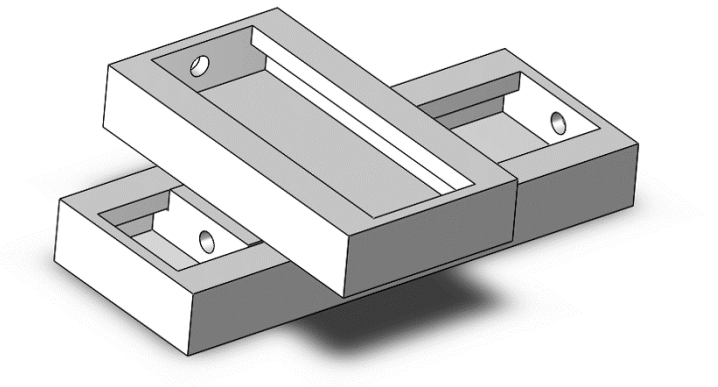

Figure 2.3: A model of the z-box, z-slide and x-box.

Similar to the z-direction, a slide will be included in the model and the screw will be represented by a linear spring, as shown in fig. 2.4.

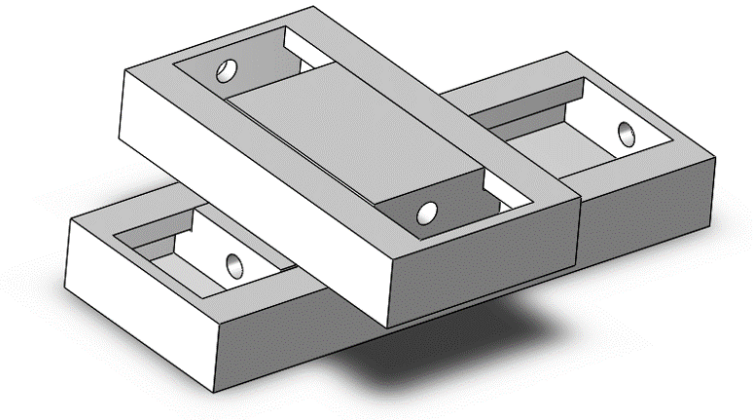

Figure 2.4: A model of the z-box, z-slide, x-box and x-slide.

Finally, a cover plate, padding block and tool changer are added to complete the model. The complete model is shown in fig. 2.5.

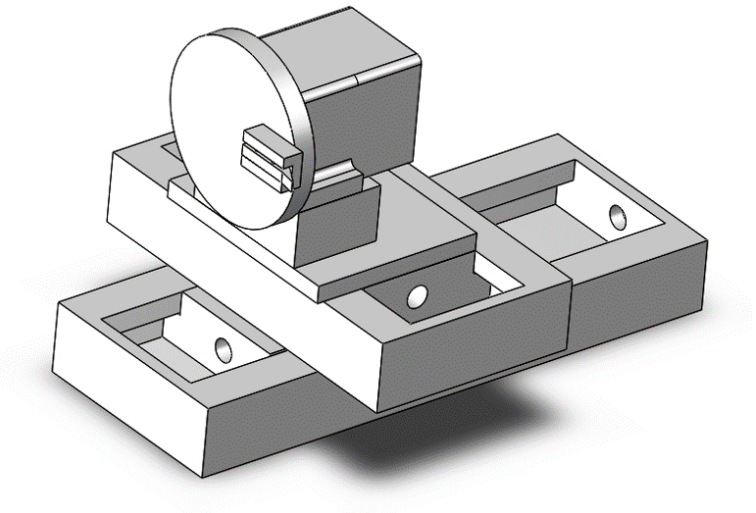

Figure 2.5: A complete model of the slides assembly.

2.1.1. First and second natural frequency (110 and 200 Hz)

As expected, the first and second natural frequency are the axial resonance frequencies of the x-axis and z-axis. These frequencies are recognized in the ball-screw drive plant transfer function as the locked rotor frequency in the transfer from motor torque to motor shaft position. In the plant transfer function from motor shaft position to table position these frequencies are the resonant frequencies. The relation in eq. 2.1 is valid. The first and second natural frequency are determined by the relevant stiffness (the combined stiffness of the side plate, the bearings, the srew and the nut) and the moving mass. The mode shapes are shown in 2.6 and 2.7. The properties of the first and second natural frequency are summarised in table 2.1.

$$f_{1,2} = \frac{1}{2\pi}\sqrt{\frac{k}{m_2}} \tag{2.1}$$

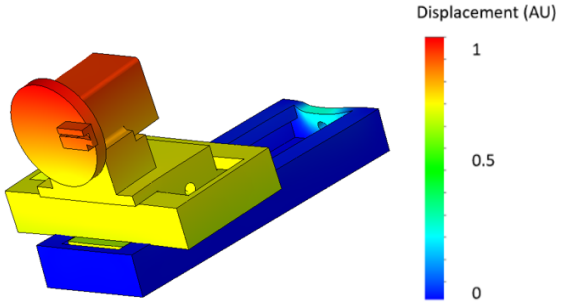

Figure 2.6: Mode shape of the first natural frequency.

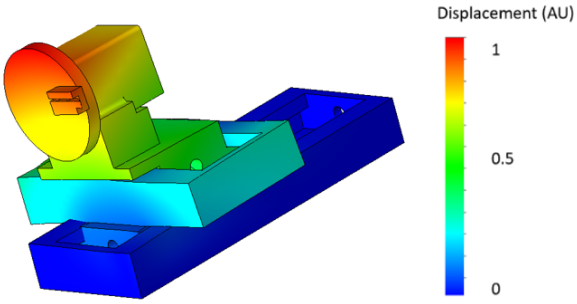

Figure 2.7: Mode shape of the second natural frequency.

Type of mode in simulation	Mainly rigid body mode
Appearance on rotary encoder	Yes, as a anti-resonance frequency
Appearance on linear encoder	Yes, as a resonance frequency
Appearance on turning tool	Yes

Table 2.1: Properties of the first and second natural frequency

2.1.2. Third natural frequency (300 Hz)

The third natural frequency is a bending eigenmode caused by the mass of the tool changer and the limited stiffness of the padding plate. In the simulation the parts (including the x-slide, cover plate and padding block) are modelled as if they are one piece of material instead of bolted together. Especially for this mode the simplification may lead to some error, because of incorrect connection modelling. The properties of the third eigenmode are shown in table 2.2.

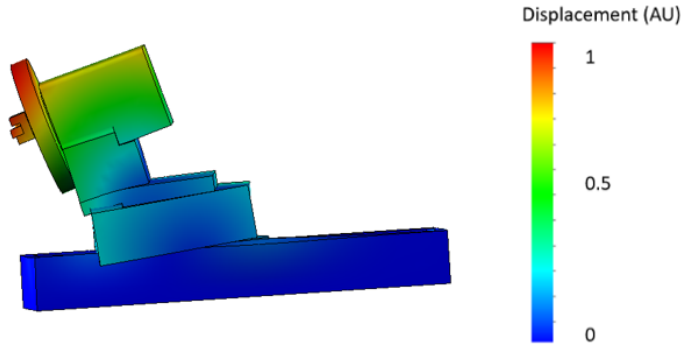

Figure 2.8: Mode shape of the third natural frequency.

Type of mode in simulation	Eigenmode (bending)
Appearance on rotary encoder	No
Appearance on linear encoder	No
Appearance on turning tool	Yes

Table 2.2: Properties of the third natural frequency.

Although in the finite element simulation appear many more natural frequencies, it is known from experimental measurements that the related modeshapes have a small amplitude. Therefor, these modes can be ignored.

2.1.3. Torsional modes of the screw

By modelling the screw as a spring, torsional modes of the screw can not be found. From literature it is known that these modes can be very important for the dynamics of a ball screw drive. Modelling these modes is fairly complex. An approximation of the mode shape and the natural frequency of a torsional eigenmode can be made by classical Euler-Bernoulli beam theory as introduced in paragraph 1.4. Neglecting the presence of the slide, eq. 2.2 provides an approximation for the natural frequencies of the torsional mode. The low mass ratio allows for neglecting the presence of the slide. G $[Pa]$ is the shear modulus (80 GPa for steel), $\rho[kg/m^3]$ is the material density (7850 kg/m^3 for steel), L $[m]$ the length of the screw and i 1...n is the number of the mode.

$$\omega_i = \frac{i}{2\pi}\sqrt{\frac{G\pi}{2\rho * L}} \tag{2.2}$$

The modeshapes M as a function of the axial coordinate x can be approximated by eq. 2.3. x is a normalised axial coordinate (0 at the beginning of the screw and 1 at the end of the screw). The maximum aplitude of the modeshape in eq. 2.3 is also normalized.

$$M(x)_i = sin(((-0.5 + i)\pi)x) \tag{2.3}$$

Based on a the material properties of steel and a screw length of 0.72 m in the z-direction and a screw length of 0.64 m in the x direction, the first and second torsional mode of the z-axis are expected around 750 and 1500 Hz. The torsional modes of the x-axis are expected around 800 en 1600 Hz.

2.2. Plant transfer functions

The determination of the relevant natural frequencies in the previous section already provides useful information about the ball screw drive. However, it is desired to go a step further and determine the transfer functions from motor current setpoint to actual motor current and from motor torque to motor shaft speed, slide position and turning tool position. The basis for the determination are the parameters given in table 2.3

	unit	value x	value z
Equivalent rotatory mass (m_1)	[kg]	$1.2*10^3$	$1.5*10^3$
Translating mass (m_2)	[kg]	$1.2*10^2$	$3.5*10^2$
Mass of the nut (m_{2a})	[kg]	1	1
Translating mass ex. nut (m_{2b})	[kg]	$1.2*10^2$	$3.5*10^2$
axial stiffness (k)	[N/m]	$1.6 * 10^8$	$1.6 * 10^8$
viscous damping screw nut interface (c)	[Ns/m]	$1.5 * 10^4$	$1.5 * 10^4$
lead (l)	[mm]	6	6

Table 2.3: Parameters used for the determination of the transfer function

The axial stiffness is a stiffness of four components in series, which are the side plate, the axially fixed bearings, the screw and the nut. The stiffness of the bearings is <confidential value> N/m and the stiffness of the nut is <confidential value> N/m. Both are catalog values. The stiffness of the screw is calculated as EA/L, being $560 * 10^6 N/m$ in x-direction and $380 * 10^6 N/m$ in z-direction for a reasonable effective length of 0.3 m, respectively 0.5 m. To determine the stiffness of the side plate, a finite element model has been made, shown in fig. <confidential supplement only> for the x-direction and shown in fig. <confidential supplement only> for the z-direction. The deformation pattern is fairly complex which makes it hard to assign a scalar value to the plate stiffness, however, a scalar value of <confidential value> N/m for the x-direction and a scalar of <confidential value> N/m for the z-direction seems reasonable. The axial stiffness is approximately $1.6 * 10^8 N/m$ for both the x- and z-axis.

2.2.1. Transfer function motor current setpoint to actual motor current

The plant transfer function from motor current setpoint to actual motor current is determined by the electrical time constant of the motor. The structural dynamics of the machine play a much more important role than the electrical time constant. Therefore, the closed loop current control (which consists of the tranfer from motor current setpoint to actual motor current, a PI controller and a feedback loop) will be approximated by a first order transfer function in the form of eq. 2.4 with τ the independent variable.

$$TF_{mcmt} = \frac{1}{\tau * s + 1} \tag{2.4}$$

2.2.2. Transfer function motor torque to motor shaft position

The transfer function from motor torque to motor shaft position has been defined in eq. 1.32, which is valid for frequencies below the torsional modes. The transfer function for the x-direction is given in 2.9 and the transfer function for the z-direction is given in 2.10. Considering higher order modes in a fully theoretical context is fairly complex since damping ratio's and relative amplitudes are hard to determine theoretically. In the next chapter, when fitting theoretical functions to experimental data, those modes will be included.

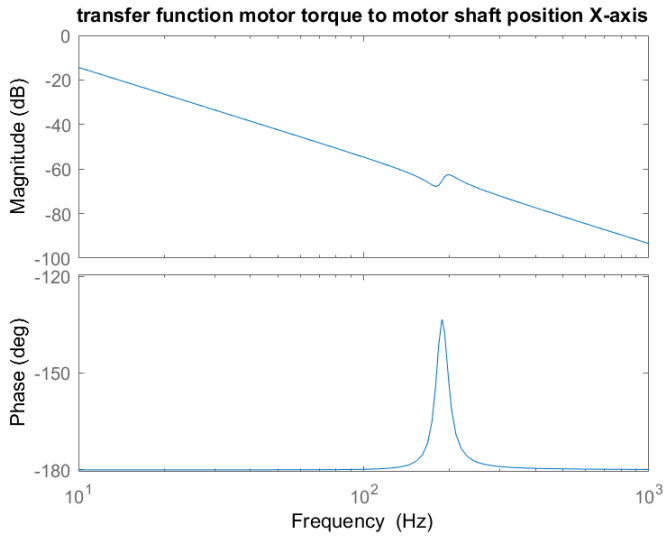

Figure 2.9: Bode diagram of the plant transfer function from motor torque to motor shaft speed in x-direction.

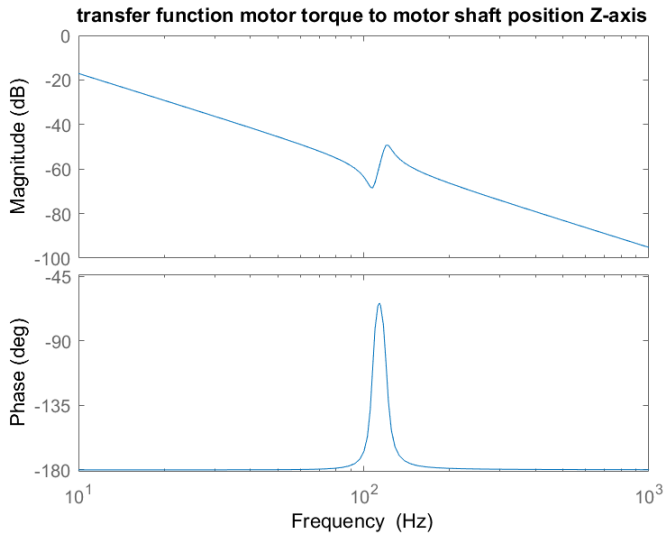

Figure 2.10: Bode diagram of the plant transfer function from motor torque to motor shaft speed in z-direction.

2.2.3. Transfer function motor shaft position to slide position

The transfer function from motor shaft position to slide position is determined in eq. 1.37. For the x-direction the transfer function is shown in fig. 2.11 and for the z-direction the transfer function is shown in fig. 2.12.

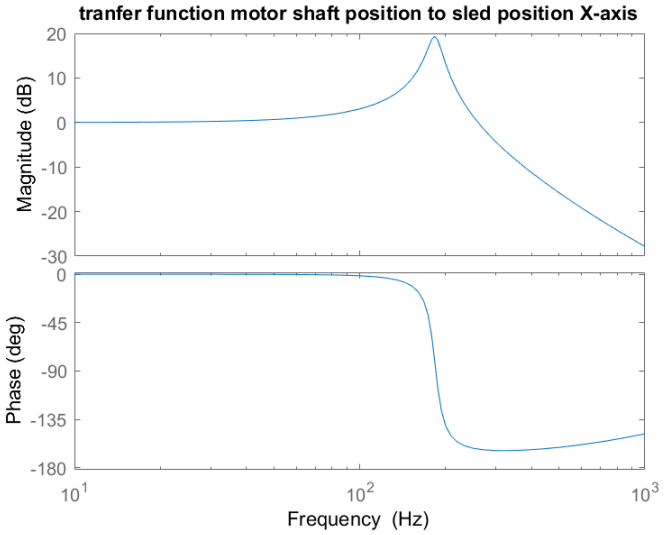

Figure 2.11: Bode diagram of the plant transfer function from motor shaft position to slide position in x-direction. The transfer function is normalised for low frequencies.

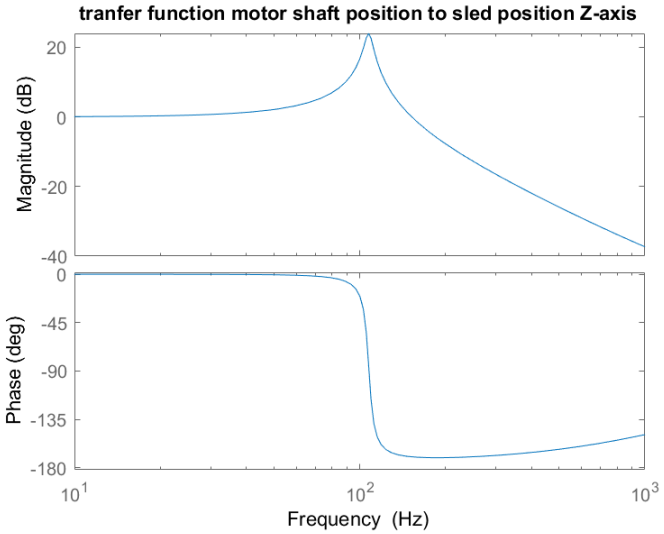

Figure 2.12: Bode diagram of the plant transfer function from motor shaft position to slide position in z-direction. The transfer function is normalised for low frequencies.

2.2.4. Transfer function motor torque to turning tool position using dynamic substructuring

The transfer functions so far describe the transfer up to the axial position of the slide. Studying the modeshape plots, it can be seen that movement of the slide is not an accurate representation for movement of the turning tool. Therefore, it is desired to formulate transfer functions from motor torque to turning tool position. It has been chosen to directly formulate a transfer function from motor torque to turning tool position, so no 'intermediate' stop at the motor shaft. This subsection starts with the formulation of a method to determine the transfer function from motor torque to turning tool position, followed by numerical results by applying the method.

2.2.4.1 Method for determining the transfer function from motor torque to turning tool position Considering the position of the turning tool, it is wished to include both classical (axial and torsional modes) and non-classical (e.a. non-axial rigid body and bending) modes in the transfer function. To include non-classical modes it is wished to use a dynamic finite element model. By trial and error, it

has been determined that modeling the contact of screw and nut in a dynamic finite element simulation is practically impossible due to the double curved contact surfaces. To overcome this limitation, a dynamic substructuring method is chosen. The screw and the nut will be described analytically, the slide including its attached components will be described by a finite element model. In literature substructures of ball screw drives are typically created by distinguishing rotating and translating components. However, with this choice the problem of the described modelling of the screw-nut interface can not be solved.

The principle of dynamic substructuring is shown in fig. 2.13. [31] Substructure A (shown on the left) is the excited substructure. It is excited at position u_1 and connected with substructure B (shown on the right) at position u_2. The response is measured at substructure B at position u_3.

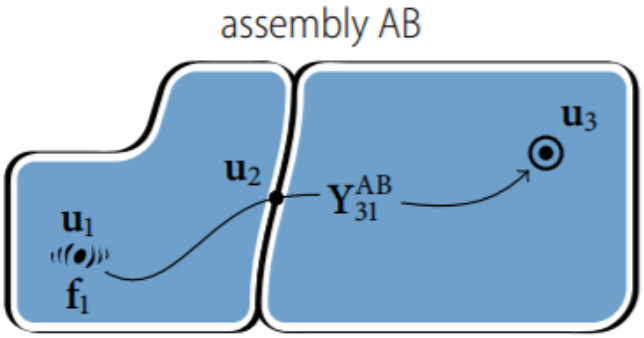

Figure 2.13: An illustration of the principle of dynamic substructuring. The transfer function of a structure AB excited at point u_1 and response measured at point u_3 can be determined by the transfer functions of substructure A and B separately.

The full transfer function Y_{31}^{AB} is determined in eq. 2.5.

$$Y_{31}^{AB} = Y_{32}^{B}(Y_{22}^{A} + Y_{22}^{B})^{-1}Y_{21}^{A} \tag{2.5}$$

Now, the relation in eq. 2.6 is valid.

$$u_3 = Y_{31}^{AB} * f_1 \tag{2.6}$$

The transfer function from motor torque to slide position (already given in the chapter one) will be used as a basis for the determination of the transfer function from motor torque to turning tool position. The used parameters are given in table 2.3 It can be verified that eq. 2.7 is valid.

$$m_2 = m_{2a} + m_{2b} \tag{2.7}$$

Substructuring the slides assembly, it has been chosen to consider the nut, screw, axially fixed bearings and side plate as substructure A and the table including its attached components and its guidings as substructure B. This is illustrated in fig. <confidential document only>.

Y_{21}^{A} can be seen as the transfer function from motor torque to motor shaft position ignoring the slide and its attached components. Y_{22}^{A} can be seen as the transfer function from a force on the nut to the position of the nut ignoring the slide and its attached components. Y_{22}^{B} can be seen as the transfer function from a force on the slide to the position of the slide (both at the position where the nut is connected), ignoring the nut and screw. Y_{32}^{B} can be seen as the transfer function from a force on the slide (at the position of the connection of the nut) to the position of the turning tool, ignoring the screw and the nut. Y_{21}^{A} and Y_{22}^{A} are determined analytically and given in 2.8 and 2.9. Y_{22}^{B} and Y_{32}^{B} will be determined with the finite element model.

$$Y_{21}^{A} = \frac{c * s + k}{m_1 m_{2a} * s^4 + c(m_1 + m_{2a}) * s^3 + k * (m_1 + m_{2a}) * s^2} \tag{2.8}$$

$$Y_{22}^{A} = \frac{m_1 * s^2 + c * s + k}{m_1 m_{2a} * s^4 + c(m_1 + m_{2a}) * s^3 + k * (m_1 + m_{2a}) * s^2} \tag{2.9}$$

Eq. 2.8 and 2.9 have been verified by using a transfer function $Y_{22}^B = Y_{32}^B = 1/(m2b*s^2)$ and applying formula 2.5. The outcome equals the transfer function from motor torque to slide position. This is correct since the classical ball screw drive theory considers the slide and its attached components as a one degree of freedom rigid body.

As an input timesignal, eq. 2.10 has been used. This is a sinc-function which has a constant frequency spectrum between values a [rad/s] and b [rad/s], with a > b. To allow for aligning the peak of the timesignal with the middle of the simulation time, there is a timeshift d, which equals half the simulation time.

$$F(t) = \frac{sin(a*(t-d))}{a(t-d)} - \frac{b}{a}\frac{sin(b*(t-d))}{b*(t-d)} \tag{2.10}$$

The use of a sinc function for the excitation of structures is common. [32] Since a full frequency band can be excited in one simulation, the sinc function allows for low computational time and less memory space needed. Function 2.10 with selected values a = 1000, b = 100 and d = 0.1 is shown in fig. 2.14. It is noticed that the timesignal has low values at the start and at the end of the simulation time. This allows for minimizing unwanted effects arising from starting conditions.

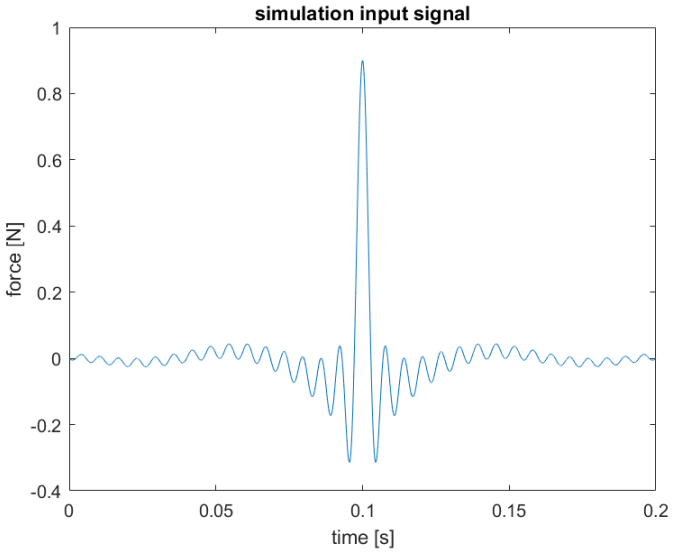

Figure 2.14: A graph of timesignal 2.10 for selected values of a, b and d.

For the finite element simulation the following parameter have to be chose properly:
Timestep: The high frequency content should be properly incorporated. According to the Nyquist criterion the maximum timestep should be no more than half the period of highest frequency in the input signal. (The lower the timestep, the more accurate the simulation is, but it also makes the simulation computationally more expensive.)
Length of the simulation: The low frequency content should be properly incorporated in the simulation. The length of the simulation should equal at least the signal period of the lowest frequency in the input signal. (The longer the simulation, the more accurate, but it also makes the simulation computationally more expensive.)
Meshsize: The meshsize should be chosen properly to allow for convergence. (The smaller the meshsize, the more accurate the results, but it also makes the simulation computationally more expensive.)

As a first step the finite element model will be prepared for simulation by removing the spring representing the screw. The input force is applied on the surface where the nut is normally attached. It is noticed that by removing the spring a floating structure is created. The finite element model may potentially simulate a 0 Hz eigenfrequency. To overcome this problem, a minimum value for b in the timesignal needs to be chosen properly. As a second step the simulation is performed and the displacement for each simulation step is recorded in the finite element model and exported to matlab. As a third step a transfer function will be determined using the algorithm tfest based on the time domain input and output data. As a fourth step, the assembly transfer function is determined by applying 2.5.

Applying eq. 2.5, the order of both the numerator and the denominator may be too high because of pool-zero cancellation not taking place. Poles and zeros do not automatically cancel because the transfer function is not exact (as a result of using finite elements as a basis). To overcome this problem, the matlab algorithm minreal will be used. Specifying a tolerance, the algorithm cancels poles and zeros that are within the tolerance to each other. It is assumed these poles and zeros would automatically cancel if the model would produce exact results.

2.2.4.2 Numerical results determining the transfer function from motor torque to turning tool position The earlier developed algorithm to estimate a transfer function from motor torque to turning tool position will be applied to the z-axis. The z-axis is interesting because the third mode (cover plate bending at 300 Hz) is only seen during excitation of the z-motor. From experimental measurements it is known that exciting the x-axis can show complex response at the turning tool, especially in the y-direction. It would be interesting to see if those effects are captured in the model. However, applying the algorithm to the x-axis is left for future work.

It has been chosen to study the transfer from 50 - 400 Hz. The lower bound is low enough to study the first eigenfrequency, and high enough to avoid incorrectly modelling a 0 Hz eigenfrequency. The upper bound is high enough to capture the third eigenfrequency, but it does not take into account the high frequency dynamics, for example the torsional modes. Eq. 2.10 has been used to create an input signal, with a = 2512 rad / s (400 Hz), b = 314 (50 Hz), d = 0.1 s and the timestep was 0.0003 s, so 334 simulation steps. Using a transfer function for $Y_{22}^B = 1/(m_{2b} * s^2)$, the transfer function for the excitation of the z-motor to turning tool position in y-direction is shown in red and the Z-direction is shown in blue in fig. 2.15. For comparison, the full analytical plant transfer function from motor torque to slide position in the z-direction is shown in yellow.

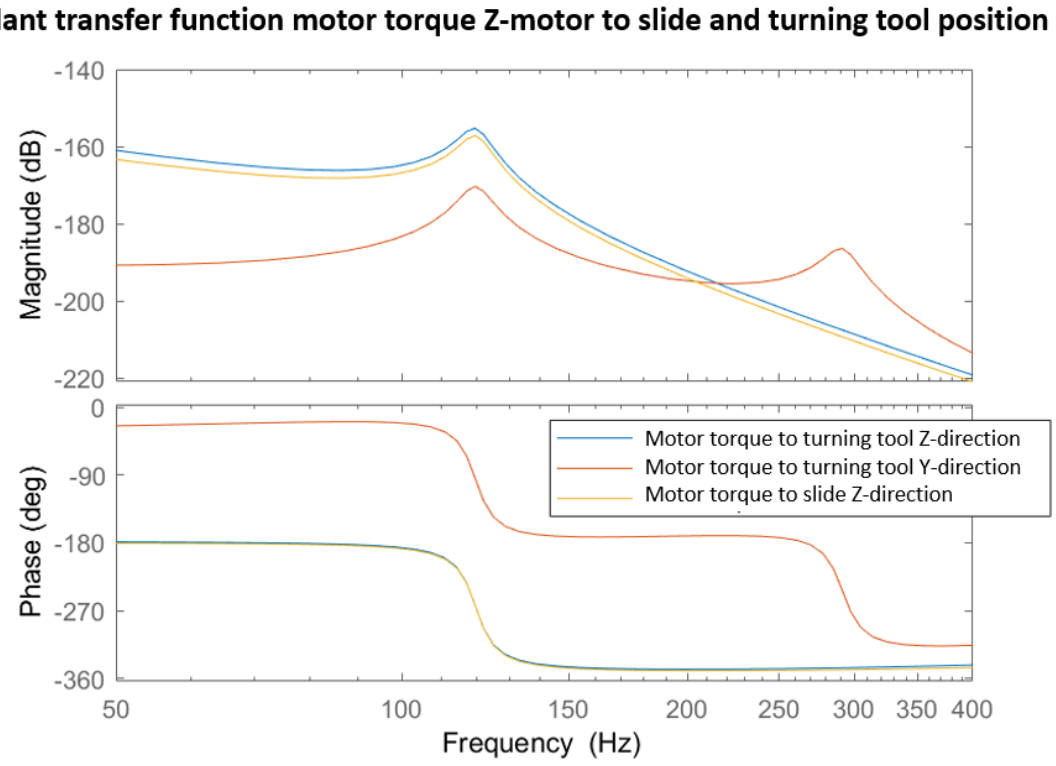

Figure 2.15: The plant transfer function from motor torque to turning tool position (y- and z-direction) has been assembled with the dynamic finite element model and analytical expressions. For comparison, the full analytical plant tranfer function from motor torque to slide position is shown in yellow.

The finite element model consisted of 44109 elements, 72155 nodes and 213,216 DOF. The simulation time was approximately 30 minutes and the output data was roughly 8 Gb, requiring the maximum RAM capacity of the computer. Due to the limited accuracy of the output data, only low order models

could be fitted. Therefore, the accuracy of the results is limited. However, conversion studies and more accurate dynamic simulation are left for future work.

The limited accuracy of the finite element model can be clearly seen comparing the blue and the yellow line. It is known from measurements that for the low frequency range, these lines should almost overlap, while for the higher frequency range the blue line should deviate from the yellow line. This effect could only be captured with a higher order model. However, the quality of the data derived with the simulation was not good enough to fit a high order model. To illustrate that this effect could potentially be captured with a model containing more elements and more simulation steps, the model has been runned twice more with one single excitation (50 and 100 Hz) frequency instead of a frequency band. For both excitation frequencies the ratio between the amplitude at the turning tool and the amplitude at the slide (linear encoder) has been calculated. For the increased excitation frequency, the ratio increased from 1.025 to 1.15, indicating that the effect of deviating response is captured with the model.

2.3. Closed loop model

To evaluate machine performance, it is wished to calculate the closed loop behaviour, e.a. the transfer from position setpoint to actual position. The closed loop position control will be calculated using a Simulink model. When decoupling the outer control (the position control loop), the simulink model can also be used for the determination of closed loop speed control. For the disturbance rejection it will be assumed that the load side disturbance is the most dominant (cutting forces disturbing the turning tool position). In literature good analytical approximations are available to predict the load side disturbance rejection. Therefore, the Simulink model will not be used to determine the load side disturbance rejection. In this section the closed loop behaviour is limited to the response that can be seen on the encoders. Although the encoders are not always a good representation for the turning tool position, the position of the turning tool itself can not be measured during operation and can not be fed back as a feedback signal.

2.3.1. Closed loop transfer function

The simulink model to determine the closed loop behaviour is shown in 2.16. It is based on the Siemens control scheme discussed in the introduction Both the x-axis and the z-axis are controlled using this scheme.

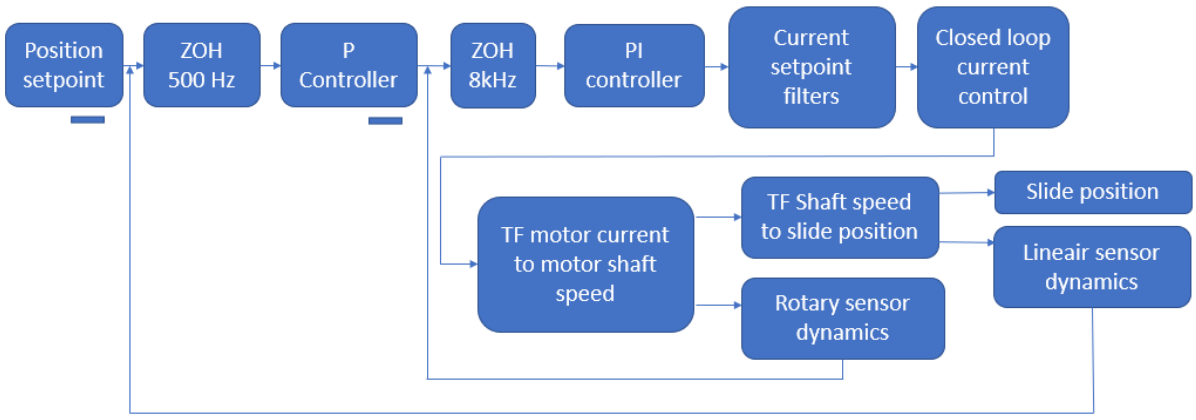

Figure 2.16: Simulink model for the determination of closed loop behaviour

The basis of the model is the innermost control loop, the closed loop current control. As described in the previous chapter, it is approximated with a low order transfer function. The unit of the current control is ampere [A]. The middle control loop is the speed control loop. The control elements are an 8 kHz drive frequency, a PI controller and current setpoint filters (a low pass filter and two notch filters to filter the torsional modes).The plant transfer function motor torque to motor shaft position contains a motor constant, describing a linear relationship between motor current and motor torque and a transfer function from motor torque to motor shaft speed, accounting for both the axial mode and the torsional modes. The rotatory sensor dynamics complete the speed control loop. The rotary sensor measures

the position of the motor axis. Using an Euler backward approximation it returns the speed of the motor shaft. The unit of the speed control is microradians per second [$m\mu/s$]. The outmost control loop is the position control. It consists of a P controller and a 500 Hz drive frequency. The mechanics consists of a transfer from motor shaft speed to slide position. This includes a gain representing the rotational to linear transformation based on the lead of the screw and a transfer functions accounting for the axial mode. The position of the slide is measured by the linear encoder. With a sensor delay the feedback loop is closed. The unit of the position control is millimeter [mm]. The operator can chose to have a feedback signal in the position control loop at 500 Hz (position drive frequency) or at 8 kHz (velocity drive frequency). This options is called Dynamic Stiffness Control (DSC). Using 500 Hz is called No DSC, 8 kHz is called Active DSC. Active DSC allows for an increased phase margin in the closed loop position control. Active DSC also allows for an increased proportional gain in the position controller leading to a smaller following error when moving with constant speed. Usually No DSC will be used, because active DSC creates difficulties creating a smootly declining magnitude plot in the closed loop position control. Also, active DSC requires a decreased proportional gain in the speed controller, decreasing the performance of the closed loop speed control.

The closed loop position control determined with the simulink model for both the x- and the z-axis is shown in fig. 2.17 and fig. 2.18. In the figures, the simulated response is shown in blue. The experimental response is shown in black. The experimental response is determined with the standard built-in machine function 'determine closed loop position control' without DSC. The control parameters are non-optimised.

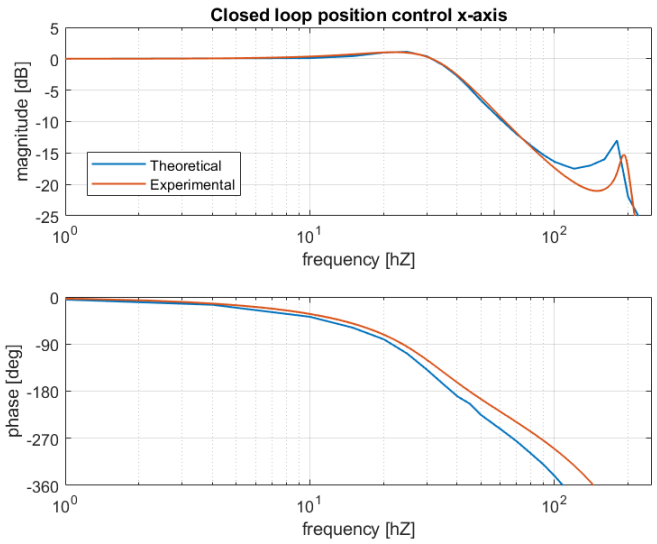

Figure 2.17: The simulated closed loop behaviour of the x-axis, compared with experimental data.

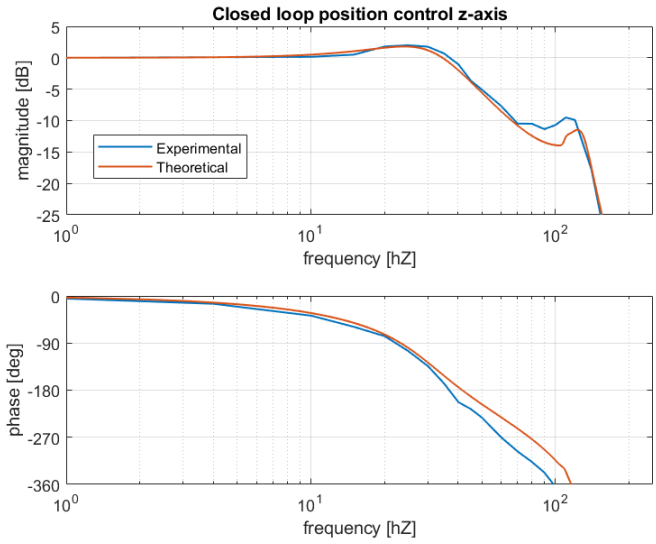

Figure 2.18: The simulated closed behaviour of the z-axis, compared with experimental data.

2.3.2. Disturbance rejection

The disturbance rejection with respect to non-stationary cutting forces will be described by a closed loop transfer function describing a transfer from cutting force to slide position. [21] This transfer function can be interpreted as the dynamic compliance of the slide and is given in 2.11. With its additional variables aa, G_{11}, G_{21}, G_{23} and L given in eq. 2.12 up to eq. 2.16. Except for the parameters given in table 2.3 three extra parameters will be used: k_{xp} (proportional gain position control), k_{vp} (proportional gain speed control) and k_{vi} (integral term speed control).

$$TF_{dr} = \frac{G_{23} + (k_{vp}s + k_{vi})(G_{11} * G_{23} - G_{13}G_{21})}{1 + L} \tag{2.11}$$

$$aa = m_1 m_2 s^4 + c(m_1 + m_2)s^3 + k(m_1 + m_2)s^2 \tag{2.12}$$

$$G_{11} = \frac{m_2 s^2 + cs + k}{aa} \tag{2.13}$$

$$G_{21} = G_{13} = \frac{cs + k}{aa} \tag{2.14}$$

$$G_{23} = \frac{m_1 s^2 + cs + k}{aa} \tag{2.15}$$

$$L = \frac{k_{vp} + k_{vi}}{s}(G_{11}s + G_{21}k_{px}) \tag{2.16}$$

A bode plot of the closed loop disturbance response of the z-axis is shown in fig. 2.19. For comparison the plant transfer function is shown in red. The frequency range could be divided in three regions. Region one is the low frequency range, roughly up to 80 Hz. Here, disturbing forces can be well suppressed by the control system. The second region is roughly from 80 to 130 Hz and marked blue in fig. 2.19. Here, the axial mode of the ball screw drive plays a role, the disturbance response reaches a maximum. The third region, roughly after 130 Hz is the region were the ball screw drive itself has very low compliance, so disturbing forces will not be problematic.

The spindle frequency (and with less amplitudes its higher orders) usually appears as a variation in cutting forces. Therefore, a spindle speed should be chosen such that the spindle frequency and its higher orders do not coincide with the second region. The same concept of disturbance rejection also plays a role in the x-axis. However, since the axial mode of the x-axis is much higher than the axial mode in the z-axis, the disturbance rejection in the z-axis is considered to be most important. However, for special cases, for example extremely high spindle frequencies or multiple cutting interruptions in one revolutions, the disturbance rejection in the x-axis may become significant.

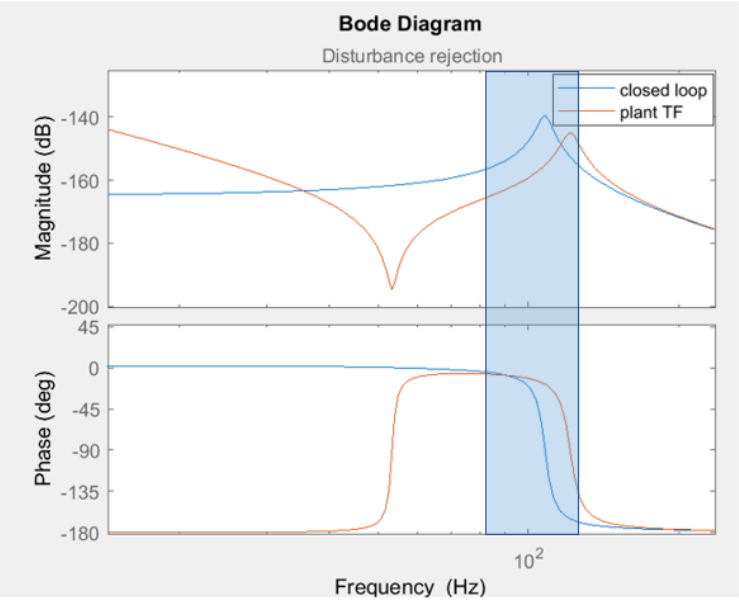

Figure 2.19: A bode diagram of the closed loop disturbance response of a Z-slide, e.a. the slide dynamic compliance.

Unfortunately no literature was found that includes discrete models for disturbance rejection. Therefore the effect of drive frequencies and time delays in the feedback loops is not taken into account. Likely this will not lead to a large discrepancy because after the axial mode the closed loop disturbance rejection closely follows the plant transfer function, indicating that the control is no longer a factor in the disturbance rejection. It is at this region where the drive frequencies and time delays are of greatest importance. The presented model considers only a one-axis configuration. No models where found in literature that study multi-axis disturbance rejection.

3

Experimental results

Two types of experimental measurements have been performed. First natural frequencies are analysed by electromechanical shakers and accelerometers (Paragraph 3.1). Second, transfer functions from motor torque to slide and motor shaft have been determined (paragraph 3.2). In paragraph 3.3 movement of the turning tool with respect to movement of the slide in the direction of excitation is studied. The analysis of the experimental measurement and the comparison with theoretical simulations and calculations is done in paragraph 3.4. In paragraph 3.5 the response toward non-stationary cutting forces is studied.

3.1. Determination of eigenfrequencies

The determination of eigenfrequencies is done with the use of the servomotors as a shaker. When using the servomotors as a shaker the motor works with a constant angular speed with an additional torque. The additional torque as a time signal can be written using eq. 3.1.

$$T(t) = \sum_{n=1}^{n=1000} \alpha_n sin(7.8\pi nt) \tag{3.1}$$

Eq. 3.1 implies a signal with peaks in the frequency spectrum spaced by 3.9 Hz. 3.9 Hz is not an exact number, it is an approximation of the exact value.

The motor torque has been measured during the shaking of the motor. The frequency spectrum of the motor torque is shown in fig. 3.1. This frequency spectrum determines which values have to be used for α_n.

For a better understanding of the relation between the motor torque described in eq. 3.4 and the frequency spectrum in fig. 3.1, fig. 3.2 provides a zoom in of fig. 3.1. Sharp peaks at specified frequencies can clearly be distinguished.

During the shaking of the motor the response of the system is measured using accelerometers. While exciting the x-motor, response is measured at the x-slide in x direction and on the machine tool in x-, y- and z-position. While exciting the z-motor, response is measured at the z-slide in z-position and at the turning tool in x-, y- and z-direction. The locations of the accelerometers are shown in fig. <confidential supplement only>. Eight different series of measurements are performed, summarized in table 3.1.

Each serie of measurements contains of 9 individual measurements, performed at different combinations of x- and z-slide positions. These positions are indicated in table 3.2.

The resonance frequencies found with the shaker tests will be discussed below. The full results can be found in appendix A.

For each individual measurement (72 in total) a frequency spectrum of the accelerometer has been calculated. For each individual measurement, the peaks (both the frequency (Hz) and the amplitude (mm/s^2)) are extracted. For good comparison, the amplitude of the peak has been divided by the corresponding amplitude of fig. 3.1, meaning output divided by input. The full results can be found in appendix A. Each identified eigenfrequency is discussed separately in the text underneath.

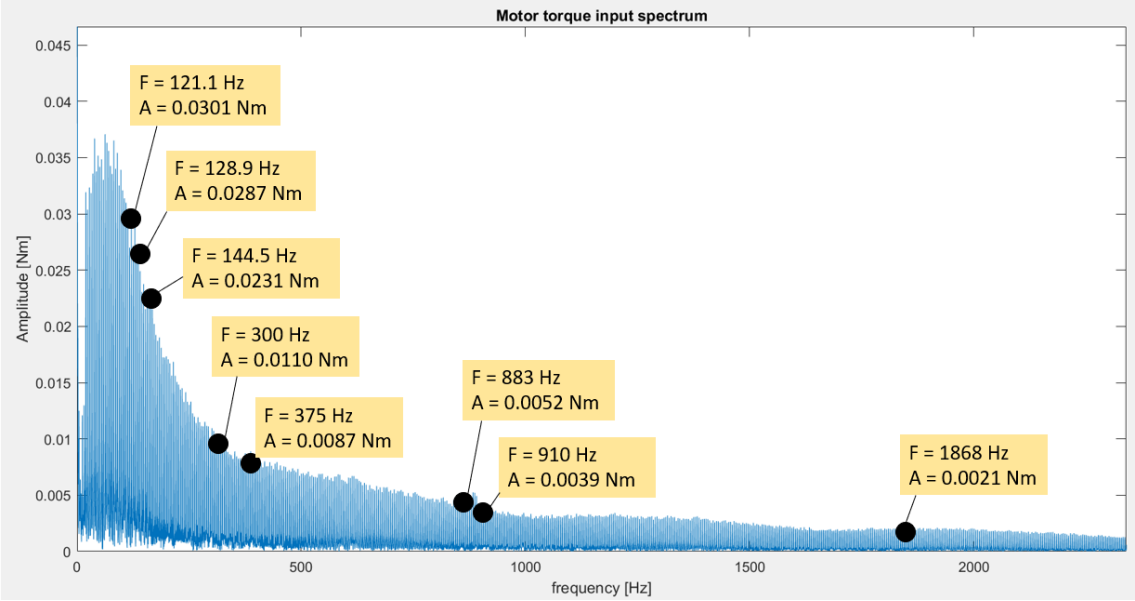

Figure 3.1: The frequency spectrum of the motor torque, used as in input signal to determine natural frequencies. The values that will appear later in this chapter as a measured natural frequency are already marked.

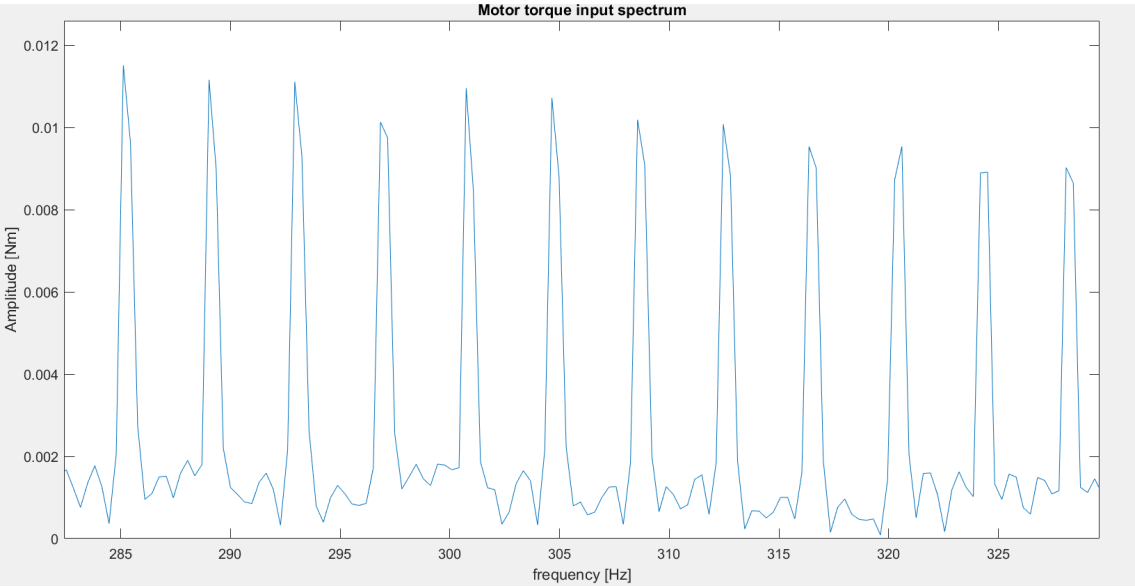

Figure 3.2: A zoom in of fig. 3.1 to highlight the sharp peaks in the frequency spectrum.

Measurement	excitation motor	measurement point	measurement direction
1	x	x-slide near the nut	x
2	x	tool tip	x
3	x	tool tip	y
4	x	tool tip	z
5	z	z-slide near the nut	z
6	z	tool tip	x
7	z	tool tip	y
8	z	tool tip	z

Table 3.1: Series of measurements performed to determine natural frequencies.

	z-position		
x-position	A:190;160 (1;0)	B 190;288 (1;0.4)	C 190;480 (1;1)
	D 88;160 (0.4;0)	E 88;288 (0.4;0.4)	F 88;480 (0.4;1)
	G 20;160 (0;0)	H 20;288 (0;0.4)	I 40;480 (0;1)

Table 3.2: The combinations of x- and z-positions for the execution of measurements. The first number indicates the absolute x-position, the second number indicates the absolute z-position. Within the round brackets the normalized position is indicated.

121 - 145 hz This is the structural resonance frequency of the z-slide, that can be excited with the z-motor. The frequency varies with the axial position of the z-slide. This resonance frequency can be seen at the (linear) encoder of the Z-axis, and at the turning tool in z- and y-direction. When normalizing the response at the slide in Z-direction, the response found at turning tool in z-direction is between 1.25 en 1.51. The response at the turning tool in y-direction is between 0.33 and 0.72, depending on the axial positions of both the x- and Z-axis. The response measured in the x-direction is neglectable.

203 Hz This is the structural resonance frequency of the x-slide, that can be excited witht the x-motor. It does not vary with axial position of the slide. This resonance frequency can be found at the (linear) encoder of the x-slide and at the turning tool in x- and y-direction. When normalizing the response at the slide in x-direction, the response found at turning tool in x-direction is between 1.39 en 1.46. The response at the turning tool in y-direction is between 0.45 and 0.58, depending on the axial positions of both the x- and z-slides. The response measured in the z-direction is neglectable.

305 Hz This resonance frequency is the bending of the cover plate, that can be excited with the z-motor. The resonance frequency can only be seen at the turning tool in y-direction.

375 Hz Likely this is a combined eigenmode and rigid body vibration, that can be excited with the x-motor. Compared to the other relevant modes, the amplitude of this mode is small. The amplitude is approximately a factor 10 smaller than the structural resonance frequency of the x-slide (203 Hz). This mode is mainly seen at the linear encoder of the x-slide and at the turning tool in x-direction.

880 Hz This is the first torsional mode of the x ball-screw that can be excited with the x-motor. Using a first order approximation this mode was predicted at 800 Hz. This mode can be seen at the x-slide at the (linear) encoder and at the turning tool in all positions. When normalizing the response at the slide in x-direction, the response found at the turning tool in x-direction is between 3.91 en 4.51. The response at the turning tool in y-direction is between 11.16 and 13.94. The response at the turning tool in z-direction is between 2.65 and 4.1, depending on the axial positions of both the x- and z-slides.

910 Hz This is the first torsional mode of the z ball-screw that can be excited with the z-motor. Using a first order approximation this mode was predicted at 750 Hz. This mode can be seen at the z-slide at the (linear) encoder and at the turning tool in all positions. When normalizing the response at the slide in z-direction, the response found at turning tool in x-direction is between 0.55 en 3.33. The response at the turning tool in y-direction is between 2.74 and 6.33. The response at the turning tool in z-direction is between 0.84 and 6.43, depending on the axial positions of both the x- and z-slides.

1852 - 1868 Hz This is the second torsional mode of the z ball-screw that can be excited with the z-motor. Using a first order model, it was predicted at 1500 Hz. The amplitude of this vibration is small. Also, the frequency of this vibration is that high, that it is considered to be an unimportant frequency.

2240 Hz This is the second torsional mode of the x ball-screw that can be excited with the x-motor. Although this mode has not been found with the accelerometers, it did appear on the rotary encoder of the motor. Using a first order model, it was predicted at 1600 Hz. This is quite a large discrepancy. However, the importance of the second torsional mode is considered to be that small that it is not a large problem. Nevertheless, using a more complicated higher order model the predictions can likely be improved.

3.2. Determination of transfer functions

For the x-slide very little variation in eigenfrequencies has been found for varying slide-positions. Therefore, the experimental transfer functions are only given for position G (the position where the turning tool is closest to the spindle) as described in table 3.2. The transfer function from motor torque to motor shaft speed is given in fig. 3.3 and the transfer function from motor shaft position to slide position is given in fig. 3.4.

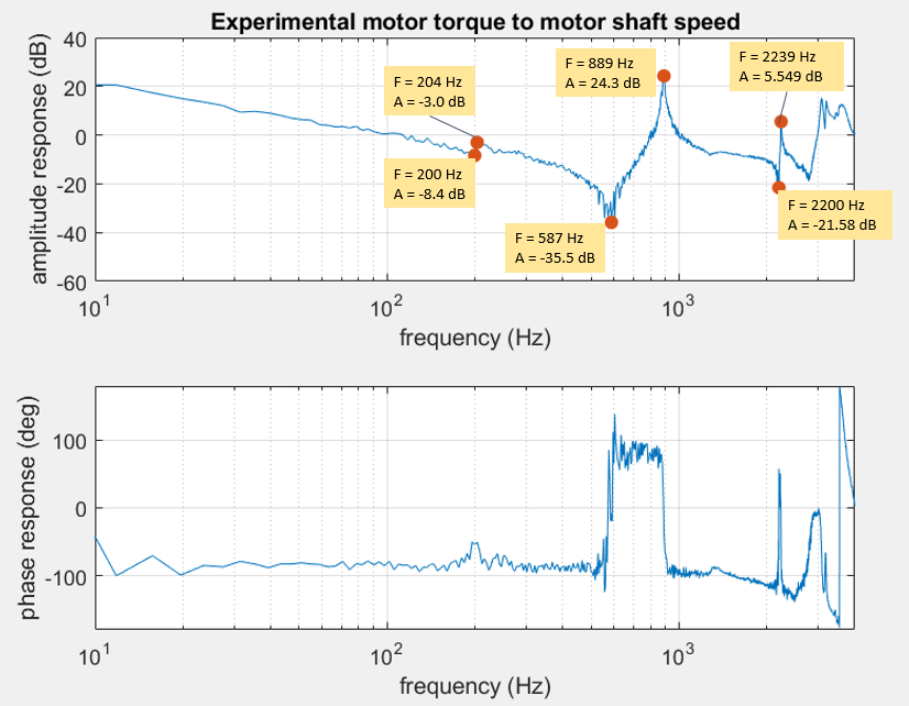

Figure 3.3: A bode diagram of the experimentally determined transfer function from motor torque to motor shaft speed for the x-direction.

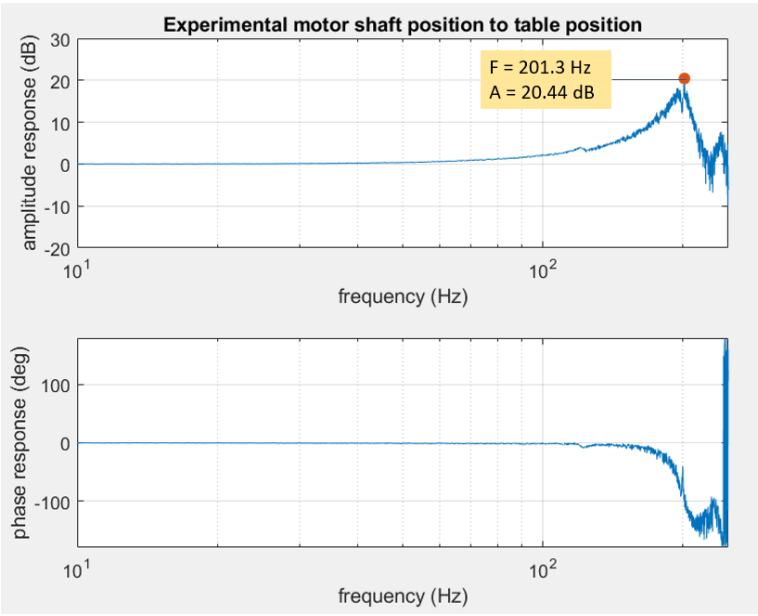

Figure 3.4: A bode diagram of the experimentally determined transfer function from motor shaft position to slide position of the x-slide.

For the z-slide variation in eigenfrequencies can be seen for varying z-positions. Therefore, in fig. 3.5 up to fig. 3.7 the transfer functions from motor torque to machine shaft speed are given for positions G, H and I. The transfer functions from motor shaft position to slide position are given in in fig. 3.8 up to 3.10. It can be seen that the frequency of the axial mode increases, while the torsional modes remain at a constant frequency. Since the experimentally derived functions show some noisy behaviour, it has been chosen not to plot multiple functions in one graph, to improve readability.

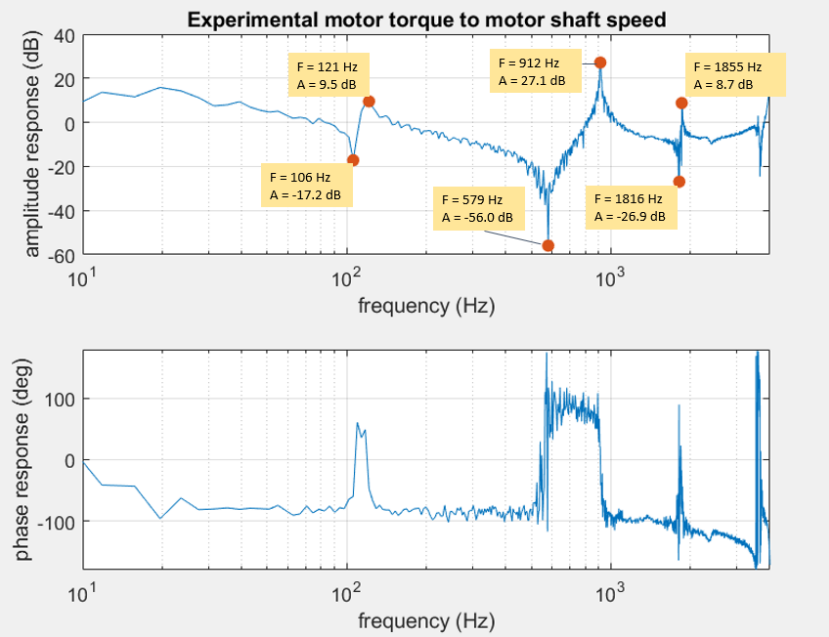

Figure 3.5: A bode diagram of the experimentally determined transfer function from motor torque to motor shaft speed for the z-axis (position G).

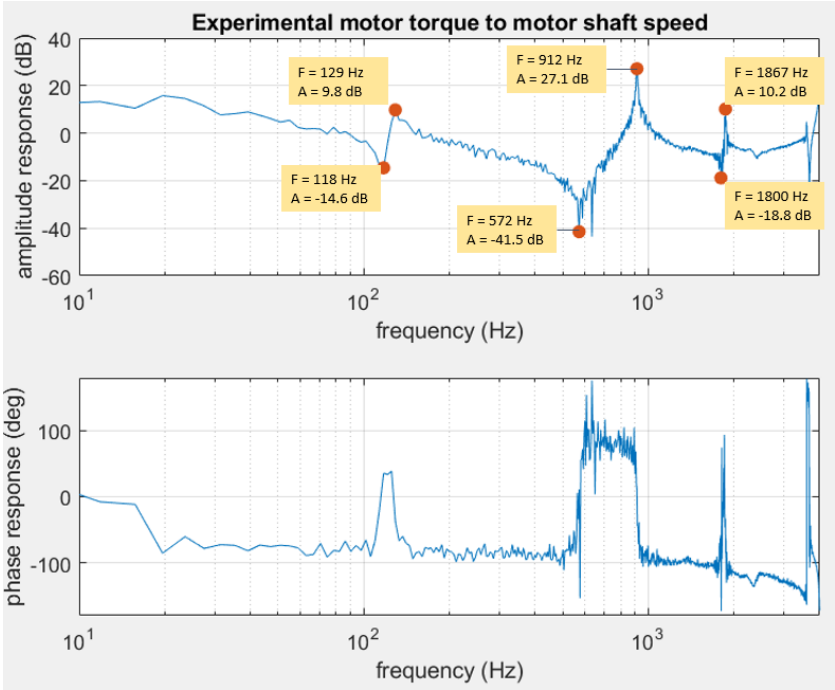

Figure 3.6: A bode diagram of the experimentally determined transfer function from motor torque to motor shaft speed for the z-axis (position H).

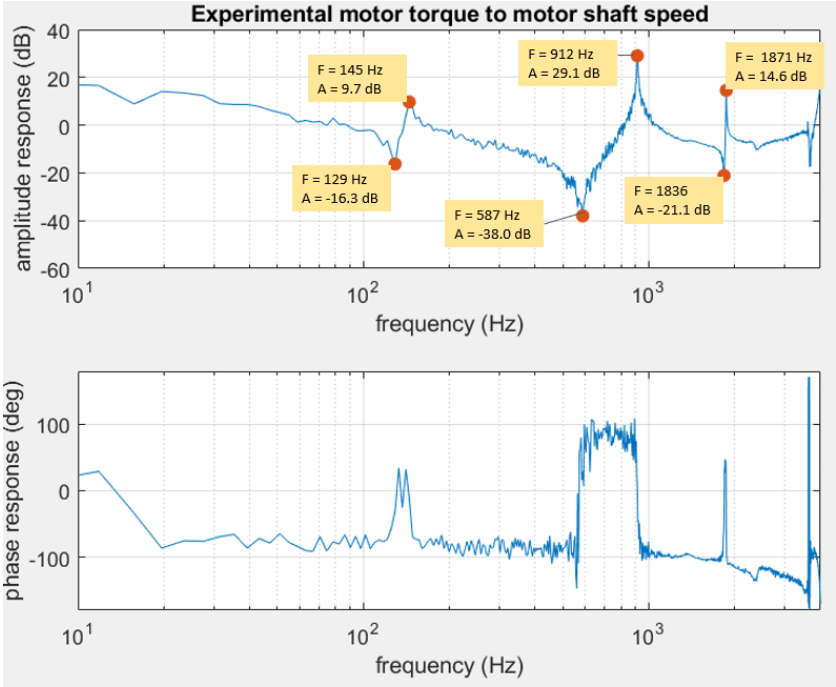

Figure 3.7: A bode diagram of the experimentally determined transfer function from motor torque to motor shaft speed for the z-axis (position I).

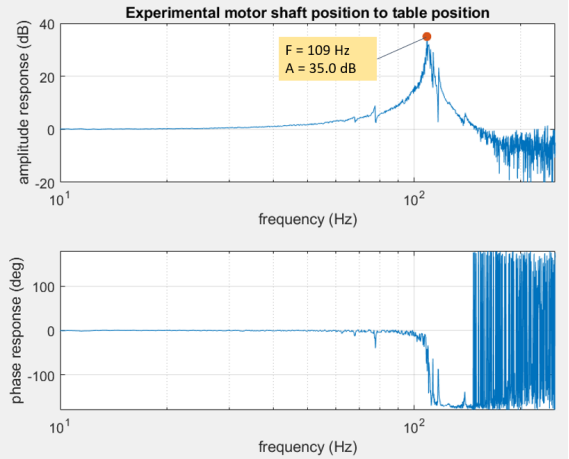

Figure 3.8: A bode diagram of the experimentally determined transfer function from motor shaft position to slide position for the z-axis (position G).

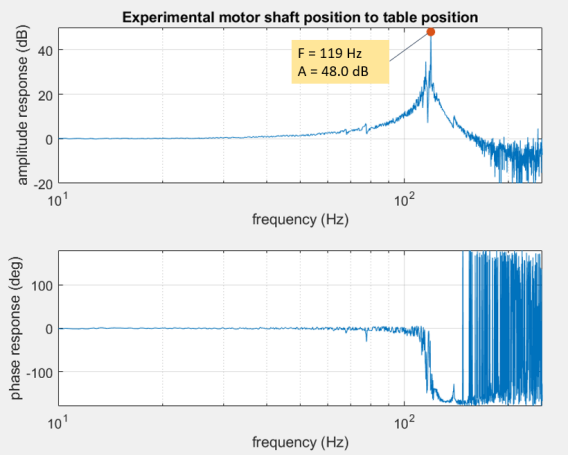

Figure 3.9: A bode diagram of the experimentally determined transfer function from motor shaft position to slide position for the z-axis (position H).

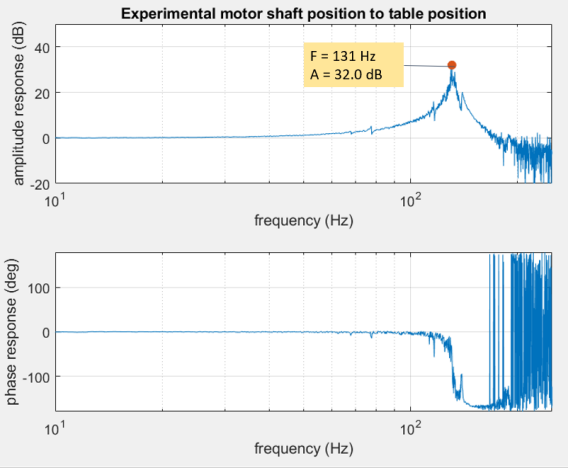

Figure 3.10: A bode diagram of the experimentally determined transfer function from motor shaft position to slide position for the z-axis (position I).

3.3. Determination of amplitude amplification at the turning tool for low frequency excitation

The previous sections were focused on the resonance frequencies and the response at the encoders. In this section response at the turning tool for the low frequency regime will be studied, specifically the region from 30 - 100 Hz. This is below the first resonance frequency. Two effects will be discussed, namely: (1) the response at the turning tool will be amplified relative to the slide in the direction of excitation and (2) the turning tool shows response in the y-direction. A third effect, namely a turning tool showing response in the x-direction while excited by the z-motor or visa versa will not be discussed here. It is known from measurements that this response is small and during normal operation it can partly be rejected as disturbance. However, the quantification and verification of this assumptions is left for future work. This section is limited to position G as described in table 3.2. Position G is the position closest to the spindle. The region around this position is used very often during machining.

3.3.1. Amplification at the turning tool in the x- and z-direction

Two types of measurements has been performed and the experimental data have been fitted to a second order polynomial. The x-slide has been excited and response is measured both at the x-slide and at the turning tool in x-direction. Also, the z-slide is excited and response has been measured at the z-slide and at the turning tool in z-direction. The results are shown in fig. 3.11.

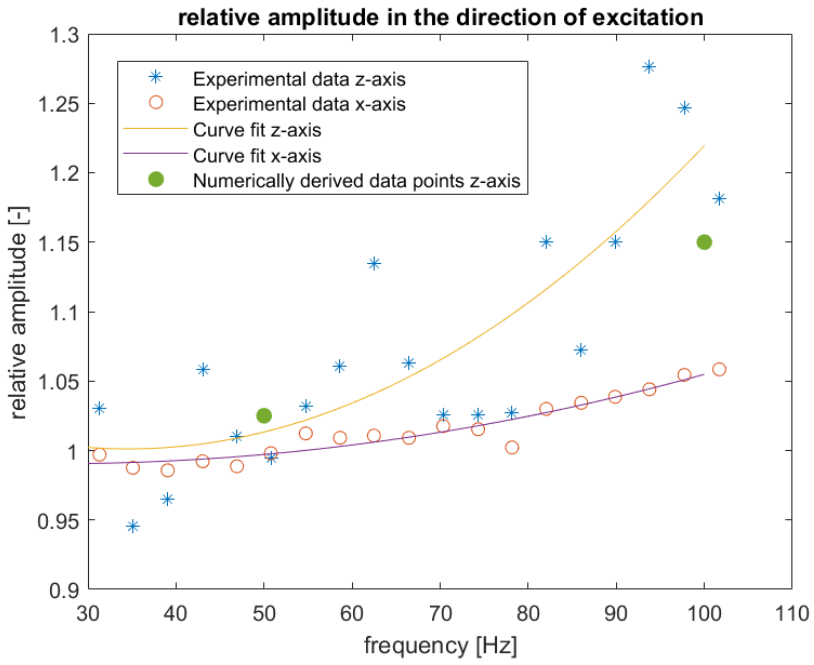

Figure 3.11: A diagram showing experimentally determined amplification factors for the x- and z-slide. A second order polynomial has been fitted to the data.

Studying the behaviour of the x-axis it can be seen that the data fit relatively well to the second order polynomial. A threshold of 40 - 50 Hz seems to be an acceptable bound for which the turning tool accurately follows the slide. At a 100 Hz the amplification is still quite low, no more than a 5 percent. Studying the behaviour of the z-slide, the data do not fit very well to the polynomial. Although the relative amplitude is clearly higher for higher frequencies the experimental data show a very chaotic behaviour. A possible explanation for the chaotic behaviour is that in between the z-slide and the turning tool there is a x-axis. Since the centre of gravity of this axis is not in line with the z-axis, the x-axis works as a pendulum, creating chaotic behaviour. The relative amplitude of the z-axis is much higher than the x-axis. This can be explained by the axial resonance frequency of the slides. At the axial resonance frequency the amplification factor for both the x- and z-axis is about 1.4. For very low frequencies the factor is roughly 1.0. In between the low frequencies and the resonance frequencies the factor climbs from 1.0 to 1.4. The z-axis has a much lower resonance frequency than the x-axis. Therefore, the

factor related to the z-axis climbs faster than the factor related to the x-axis. For completeness, the numerically derived data points (see section 2.4) by exciting the model twice with a single excitation frequency are also plotted in the figure.

3.3.2. Amplification at the turning tool in y-direction

Again two types of measurements have been performed. The x-slide has been excited and response has been measured at the x-slide in the x-direction and at the turning tool in y-direction. Also the z-slide has been excited and response has been measured at the z-slide in z-direction and at the turning tool in y-direction. The results are shown in fig. 3.12.

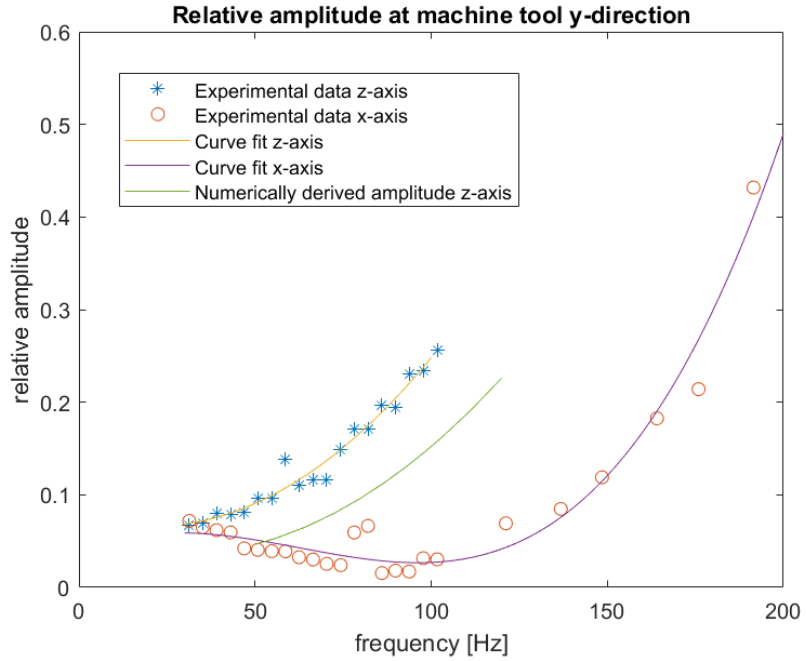

Figure 3.12: A diagram showing experimentally determined amplification factors for the x- and the z-slide. A second and third order polynomial has been fitted to the data.

For a good understanding of the behaviour of the x-axis, a few extra datapoints have been added up to the axial mode. It is very remarkable that the data points reach a local minimum in the region around 100 Hz. For an unidentified reason, turning the tool experiences a high dynamic stiffness for this region. A possible explanations might be the axial resonance frequency of the z-axis which is also around this frequency. When excited at 100 Hz, all energy might go to the axial resonance frequency of the z-axis, resulting in only very small movement of the x-axis. To be able to capture this local minimum in the curve fit, a third order polynomial has been used to fit the data. Around the axial resonance the relative amplitude reaches 0.5. Studying the behaviour of the z-axis, the second order polynomial fits the data quite well. This is remarkable because in the z-direction (discussed in the previous section) there was a much more chaotic behaviour. Around the axial resonance the relative amplitude reaches 0.3. For completeness the numerically derived amplitude (see section 2.4) by exciting the model with a frequency bandwidth are plotted in green. Although the numerically derived data points show a clearly increasing amplitude, they are too low. The discrepancy is likely due to the low order of the numerical model, as discussed in section 2.4. Also, the CAD model of the tool changer may include some modelling error because the manufacturer of the tool changer did not include a full detail CAD model, a simplified version has been created.

3.4. Comparison of theoretical and experimental results

In this section the theoretical predictions in chapter 2 will be compared with the experimental results in paragraph 3.1 and 3.2.

3.4.1. Resonance frequency comparison

First and second resonance frequency The first resonance frequency (seen during z-excitation) and the second resonance frequency (seen during x-excitation) is undoubtedly the axial resonance frequency. In x-direction the frequency is determined to be around 200 Hz independently of its axial position, meaning that the screw is not a significant factor in the axial stiffness. In Z direction the axial resonance frequency is determined to be between 109 and 131 hZ depending on the axial position, meaning that the screw is a significant factor in the axial stiffness. As expected, the axial resonance frequency has the greatest amplitude in the direction of excitation, but can also be seen in other directions. The experimental and theoretical results show no significant difference.

Third resonance frequency The third natural frequency of about 300 Hz is mainly seen during excitation of the z-motor and measuring response at the turning tool in y-direction (measurement series 7). This makes it very likely to be the third natural frequency as predicted in chapter 2. The experimental and theoretical results show no significant difference.

Fourth natural frequency The fourth natural frequency is determined to be about 375 Hz and only seen in x-direction during excitation of the x-motor. Likely this corresponds to the fourth natural frequency as determined in chapter 2. Theoretically this frequency was predicted at 475 Hz. This is a large discrepancy, possibly caused by the complexity of the modeshape.

Fifth and sixth natural frequency The fifth and sixth natural frequency are the torsional modes of the ball-screw. The experimental and theoretical results are given in table 3.3.

	z-axis I	x-axis I	z-axis II	x-axis II
Theoretical	750 Hz	800 Hz	1500 Hz	1600 Hz
Experimental	912 Hz	889 Hz	1867 Hz	2239 Hz
Error	22 %	10 %	20%	29%

Table 3.3: The theoretical and experimental results of the first and second torsional modes in the ball-screw.

For the torsional modes there is discrepancy between the theoretical and experimental results. This is likely due to the low order modelling and neglecting the presence of the slide. On average the error is the largest for the second torsional mode, likely because this mode has the most complex modeshape. The modeshape of the first torsional mode is expected to be a quarter of a sine wave. This is a modeshape with a relatively low slope (first derivative), therefore it is hard to draw conclusions from the measured amplitude. The modeshape of the second torsional mode is expected to be a three quarter sine wave, meaning a modeshape with more slope (higher first derivative) and a node in the middle of the screw. Studying the response of the second torsional mode of the z-axis at the turning tool in z-direction, it can be seen that the amplitude is low when the slide is around the midpoint of the screw, and high when the slide is at its ends. This is shown in fig. 3.13.

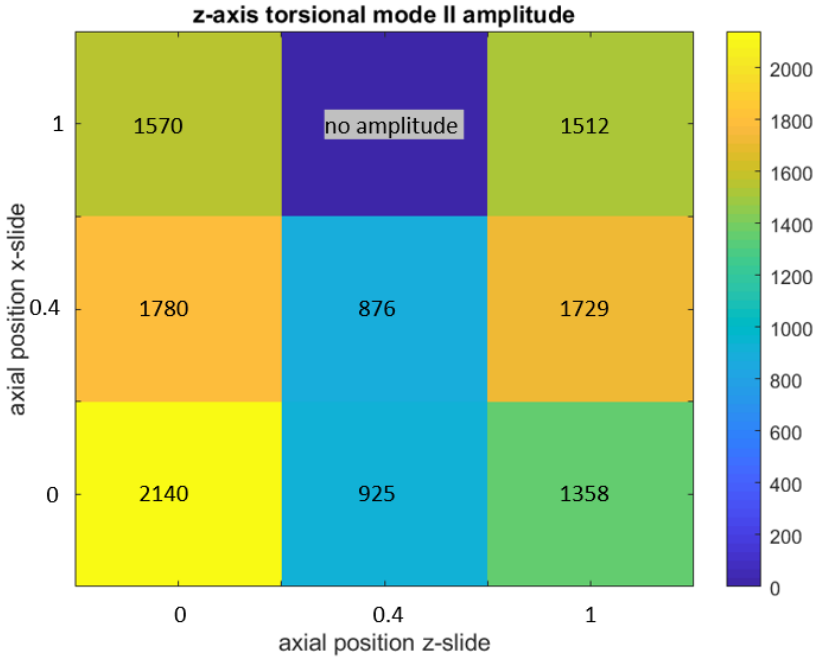

Figure 3.13: A heatmap of the amplitude $[(mm/s^2)/Nm]$ of the second torsional mode of the z-axis excited by the z-motor and measured at the turning tool in z-direction. The amplitude $[mm/s^2]$ is given per unit motor torque [Nm].

3.4.2. Bode plot motor torque to motor shaft speed comparison

First the predictions of eq. 1.32 are compared with the measured results. (Eq. 1.32 is fully based on the mass, stiffness and damping parameters given in table 2.4.) In fig. 3.14 the comparison is shown for the x-slide, in fig. 3.15 the comparison is shown for the z-slide. Eq. 1.32 provides good approximations up to 400 Hz.

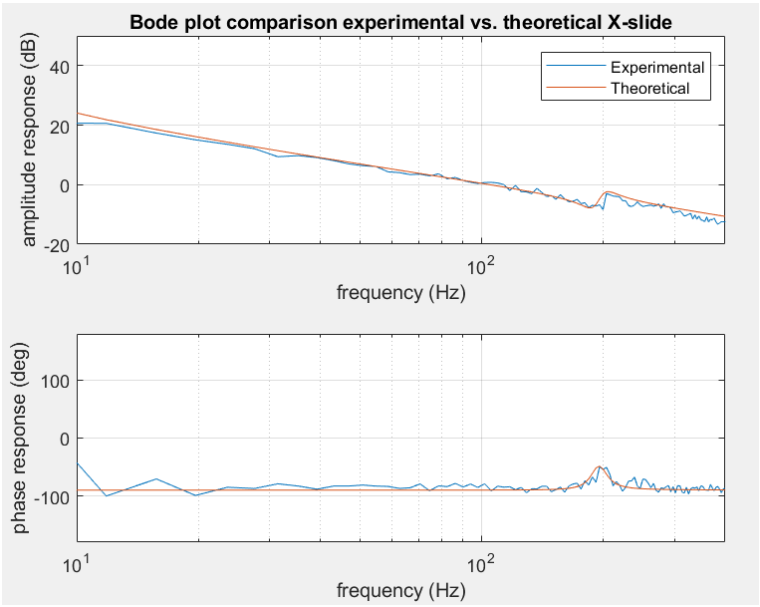

Figure 3.14: A bode diagram comparing the experimentally determined transfer (motor torque to motor shaft speed) with its theoretical equivalent.

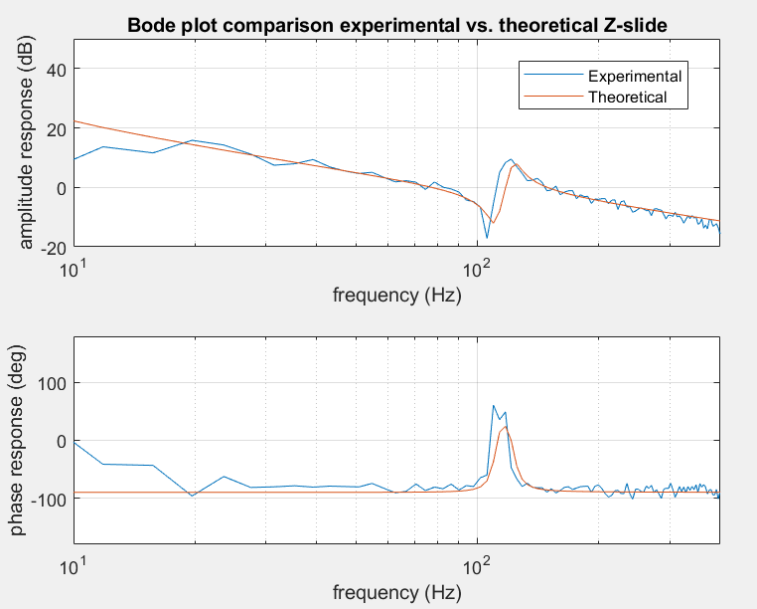

Figure 3.15: A bode diagram comparing the experimentally determined transfer (motor torque to motor shaft speed) with its theoretical equivalent.

To go a step further and also include the torsional modes in the transfer function, eq. 1.35 will be fitted to experimental data. The procedure for this fit is to use data points around the resonance and anti-resonance frequencies and find values for α_0 up to α_3 and ξ_1 up to $\xi 3$. At least seven data points need to be included to fit seven parameters. However, more parameters make the curve fitting more accurate. ω_1 up to ω_3 are read from the figure. It should be noticed that the frequency read from the figure is the damped eigenfrequency. The frequency that has to be filled in the formula is the undamped eigenfrequency. The relation is given in eq. 3.2

$$\omega_n = \frac{\omega_d}{\sqrt{1-\xi^2}} \tag{3.2}$$

The curve fit for the x-slide based on 1.35 is shown in fig. 3.16. The corresponding parameters are given in table 3.4. The curvefit for the z-slide is shown in fig. 3.17. Its corresponding parameters are given in table 3.5. The curve fit has been performed in Matlab with the algorithm fminsearch. This is nonlinear programming solver that minimizes an unconstrained multi-variable function. In this case it minimizes the discrepancy between the experimental data and the curve fit.

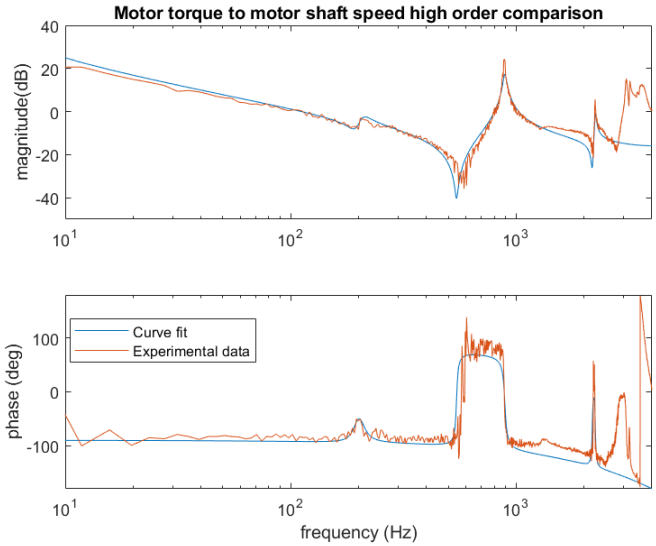

α_0	729
α_1	74.3
α_2	1424
α_3	205
ξ_1	0.133
ξ_2	0.034
ξ_3	0.0148

Table 3.4: Parameters used in fig. 3.15.

Figure 3.16: A bode diagram showing the experimental results in red and the theoretical parameterized fitted function in blue.

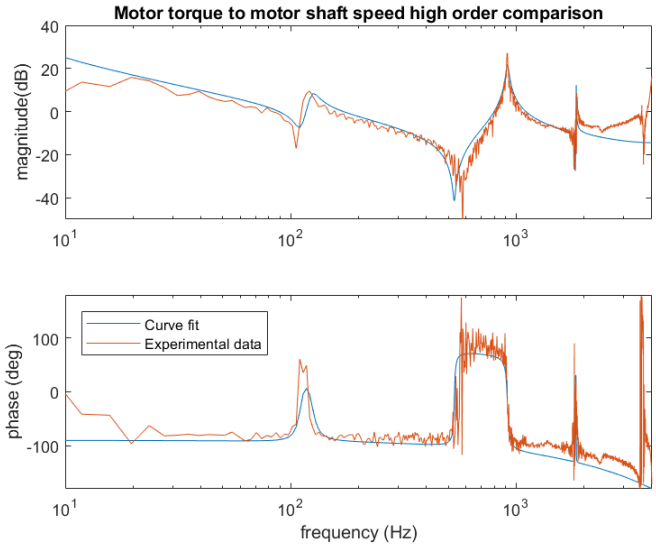

α_0	455
α_1	122
α_2	1698
α_3	172
ξ_1	0.060
ξ_2	0.020
ξ_3	0.0148

Table 3.5: Parameters used in fig. 3.16

Figure 3.17: A bode diagram showing experimental results in red and the theoretical parameterized fitted function in red.

3.4.3. Bode plot comparison motor shaft position to slide position

In the figures below the experimental transfer function from motor shaft position to slide position is compared with the theoretical transfer function given in eq. 1.37. (The theoretical transfer function given in eq. 1.37 is fully based on the mass, stiffness and damping parameters given in table 2.4 and is valid for frequencies well below the torsional modes.)

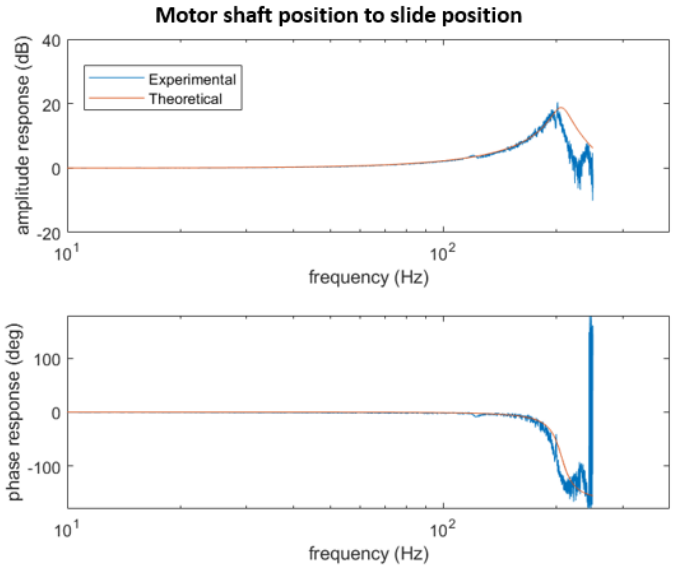

Figure 3.18: A bode diagram comparing the theoretical transfer function with the experimental transfer function for motor shaft position to table position of the x-axis.

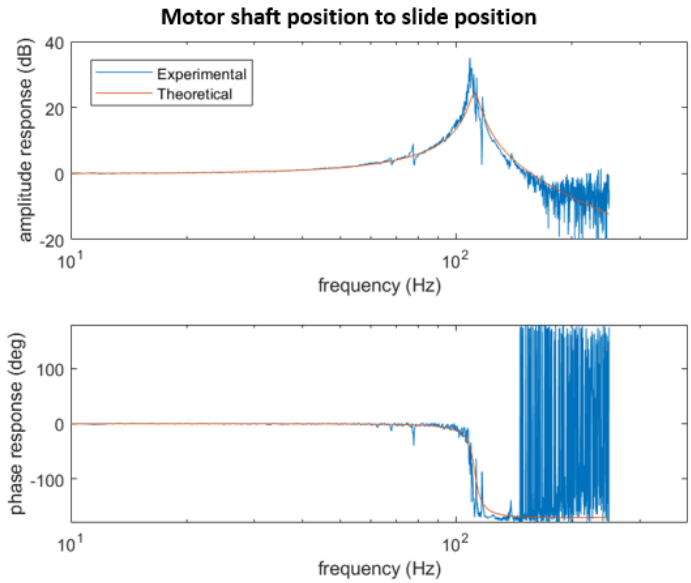

Figure 3.19: A bode diagram comparing the theoretical transfer function with the experimental transfer function for motor shaft position to table position of the z-axis.

3.5. Experimental load side disturbance response

To study experimental load side disturbance response a cylindrical workpiece has been created with 4 cutting interruptions. The workpiece before the experiments is shown in fig. 3.20. During the experiment the turning tool had an axial feed direction. For 12 different diameters a square chip has been created of 0.2 x 0.2 mm with constant cutting speed, to ensure constant cutting force. A decreasing workpiece diameter allows for an increasing rotational speed of the main spindle. The primary disturbance frequency (which equals the spindle frequency times four) varied between 70 and 127 Hz. This allows for studying the disturbance response around the axial resonance frequency. The workpiece after the experiments is shown in fig. 3.21.

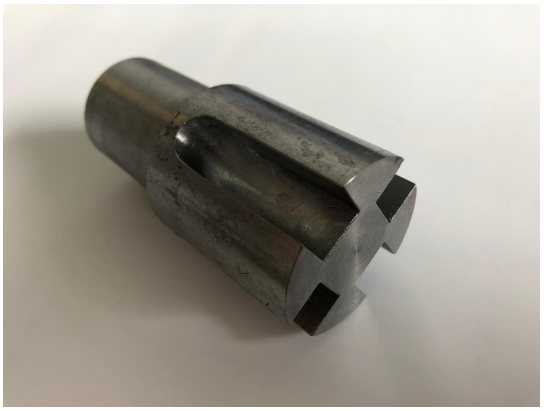

Figure 3.20: The workpiece before the experiments

Figure 3.21: The workpiece after the experiments

The cutting force as a function of time can be written as a pulse train. Defining F_0 as the cutting force when the turning tool is in contact with the material and d as the percentage of time the turning tool is in contact with the workpiece. The cutting force as a function of time is given in eq. 3.3. f is four times the spindle frequency. (Four interruptions per revolution.)

$$F(t) = F_0 d + \sum_{n=1}^{\infty} A_0 cos(2\pi f t n) \tag{3.3}$$

With A_0 defined as:

$$A_0 = \frac{2F_0}{n\pi} sin(n\pi d) \tag{3.4}$$

During the cutting process a trace has been made of the position error of the slide (position setpoint minus actual position) with a sample rate of 500 Hz. Therefore, disturbances up to 250 Hz are accurately captured in the trace. A Fourier analysis has been applied on the trace to create a frequency spectrum. The primary excitation frequency and its second order become clearly visible in the frequency spectrum. The cutting force in the z-direction is estimated to be 15 N. The disturbance response [m/N] is calculated and compared with the theoretical prediction defined in paragraph 2.3.2. The results are shown in fig. 3.22. For the region 70 - 90 Hz the experimental data are decreasing, while the response of the model is increasing. Around or below 70 Hz there is low dynamic stiffness. Further research, including studying disturbance response below 70 Hz is needed to explain this result. For the region 90 - 130 Hz the experimental data closely follow the model. For the region 130 - 200 Hz, the experimental data points are decreasing in magnitude, but not as strong as the model. For an unidentified reason, the experimental data do not closely follow the load inertia. After 200 Hz, the experimental data sharply increase, showing a peak at the structural resonance frequency of the x-axis. This effect is not included in the model, since the model describes the axis as if there is no other axis.

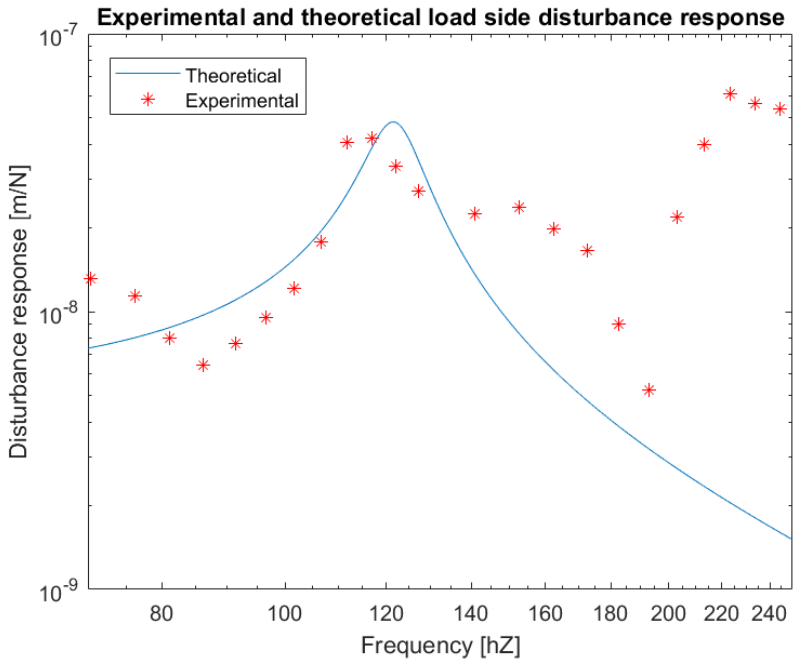

Figure 3.22: A bode diagram (magnitude only) of the load side disturbance rejection. The theoretical transfer function is shown in blue. The experimentally derived data points are shown in red.

4

Machine optimisation with a cycle of optimal design

The P-PI ball-screw drive control strategy as described throughout this thesis is the most widely used strategy for ball-screw drive control because of its high adaptability, simplicity, and ease of understanding, designing, and tuning. [26] Although many more control strategies are possible, this thesis remains limited to the P-PI strategy. The objective of the machine optimisation is to maximise the closed loop control bandwidth in terms of magnitude and phase. In this chapter several options will be discussed to increase the closed loop bandwidth. At the end of this chapter, the influence of design changes on disturbance rejection and (quasi-)static position accuracy will be discussed. To come up with optimal design a loop is proposed in fig. 4.1. As a (possible) first step a design is chosen or created. The sec-

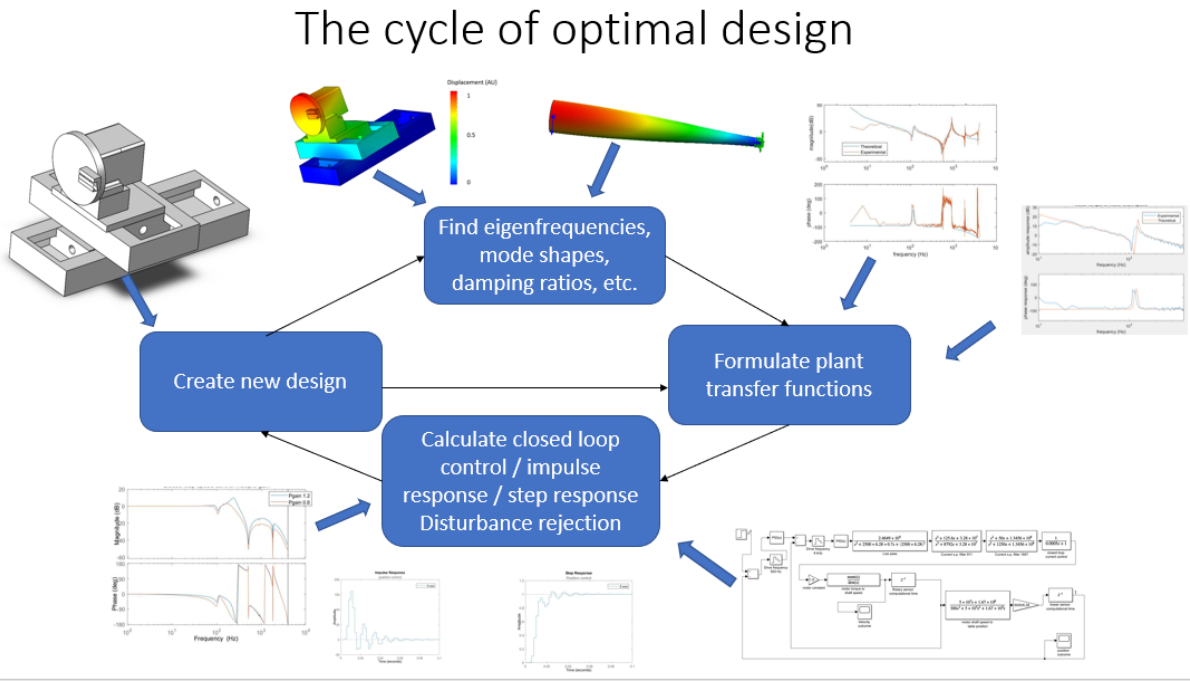

Figure 4.1: The cycle of optimal ball screw drive design

ond step is to find eigenfrequencies and corresponding damping ratio's and modeshapes. Based on this information plant transfer functions can be formulated in step 3. In step 4 the closed loop behaviour can be calculated, typically by considering the closed loop control bandwidth. Also other measures are possible, for example the step response or impulse response. In case of a non-geometrical design

change, step 2 can be skipped. For the optimisation, boundary conditions and assumptions have been defined:

1. The ratio between the translating mass and the equivalent rotary mass should not be smaller than 0.1. (As discussed in paragraph 1.7.)

2. The mass of the slides ($1.2 * 10^2$ kg for the x-axis and $3.5 * 10^2$ kg for the z-axis) is kept constant. Also the geometry of the slides is kept constant, except for adjustments to fit a different diameter screw. Nevertheless there is a possibility for dynamic improvement optimising the geometry of the slides. One objective could be to minimize the translating mass. (Decreasing the mass of the slide with a factor α roughly allows for a decrease in screw diameter with a factor $\sqrt{\alpha}$ maintaining the axial resonance frequency constant. The equivalent rotating mass decreases with a factor α^2. Therefore, a better mass ratio between translating mass and equivalent rotary mass can be realized or a possibility is created to decrease the lead of the screw to improve position accuracy.) A second objective of geometrical changes could be to minimize discrepancy between movement of the slide with respect to movement of the turning tool in the feed direction and minimize movement of the turning tool in the non-feed direction.

3. The stiffness of a nut is proportional with the diameter of the screw. (Increasing the diameter of the screw either increases the number of balls or the diameter of the balls in the nut, making the nut stiffer.)

4. All damping in a ball-screw drive system is realised in the screw-nut contact. The damping is proportional with the stiffness of the nut. (As discussed in paragraph 1.7.)

5. The buckling load should not be exceeded [13], e.a.:

$$SF_{bl} * F_{axial} < \frac{\pi^2 * EI}{\lambda_{bl} L^2} \tag{4.1}$$

   With SF_{bl} is the safety factor related to the buckling load (common factors range from 0.5 - 0.7), F_{axial} the axial force (composed out of gravitational forces, cutting forces and forces related to the acceleration of the slide), λ_{bl} the effective length correction factor (the factor typically varies between 1 and 2 depending on the fixation of translations and rotation at the boundaries), E the Young's modulus, I the moment of inertia and L the effective length of the screw.

6. The critical speed should not be exceeded to avoid excitation of the first bending mode of the shaft [13], e.a.:

$$SF_{cs} * \omega_c < \lambda_{cs} * \sqrt{\frac{EI}{ML^3}} \tag{4.2}$$

   With SF_{cs} the safety factor related to the critical speed (common values range from 0.7 to 0.8), ω_{cs} the critical speed, λ_{cs} the support bearing factor (for fixed-free $\lambda_{cs} = 3.5$, for fixed-supported $\lambda_{cs} = 15.4$) and M the mass of the shaft.

7. The proportional gain in the position control and the lead should be equal for the x-axis and the z-axis. This is because for a given speed the following error is proportional with the proportional gain in the position control. To avoid contour error, it is required to have identical proportional gain and lead in the x- and the z-axis

8. For each configuration the control parameters have been optimised. It is assumed that the discrepancy between the found optimum and the true optimum is neglectable. However, in specific cases the found optimum might be closer to the true optimum than in other cases.

4.1. Increasing closed loop cut-off frequency

The goal of this paragraph is to find a configuration that has the highest closed loop position control cut-off frequency. The cut-off frequency is defined as the point that crosses either the -3 dB line or the -180 degree line. Given the P-PI control strategy a top level choice that has to be made is whether to use Dynamic Stiffness Control (DSC) or not. When DSC is active, the feedback of the position control is at the drive frequency of the velocity control. Which means the timedelay in the in the position control is the inverse of the drive frequency of speed control. When DSC is not active, the feedback of the position control is just at the drive frequency of the position control.

4.1.1. Dynamic Stiffness Control inactive

The optimisation starts by studying a variation in drive frequencies. The results are shown in fig. 4.2 for the z-axis and in fig. 4.3 for the x-axis. For the z-axis there is a large potential for improvement when

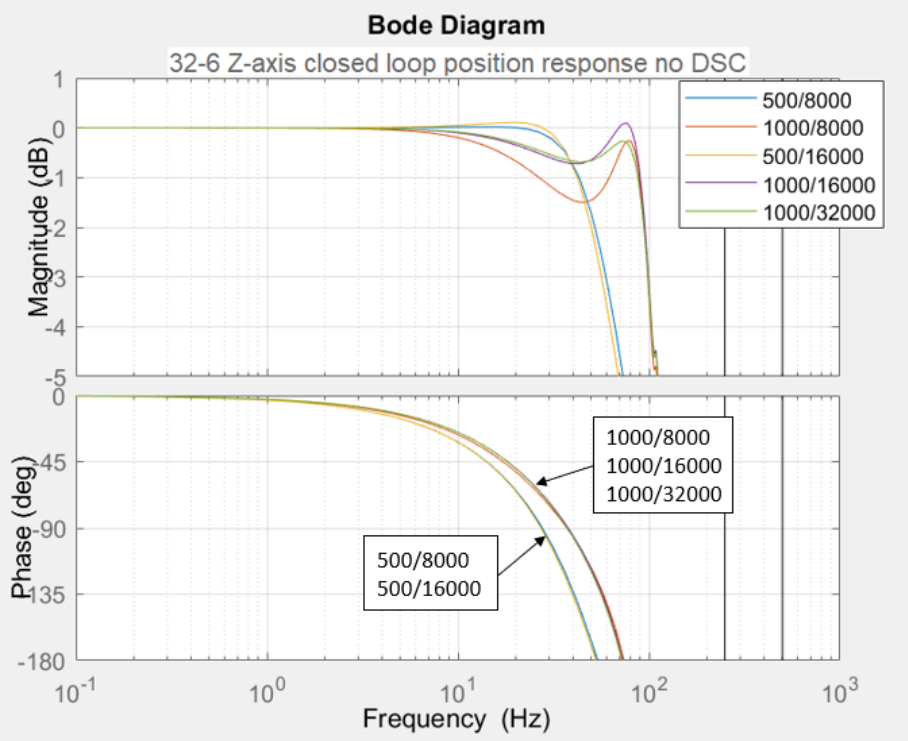

Figure 4.2: A bode diagram comparing the closed loop position control for different combinations of drive frequencies for a z-axis, position control drive frequency [Hz] / velocity control drive frequency [Hz]. The blue line represents the current configuration.

using an increased drive frequency in the position control. However, an increased drive frequency in position control introduces an additional maximum and minimum in the magnitude plot for the closed loop position control instead of a smoothly declining magnitude. The peak and the valley can be made less sharp by increasing the drive frequency in the speed control (leading to additional costs) or by choosing a smaller value for the proportional gain in the velocity control (leading to a decrease in phase margin). Alternatively, a notch filter in position control could be used to suppress the peak in the magnitude plot. As a drawback, a notch filter causes a decreased phase margin.

On the contrary, in the x-axis a problem appears when increasing the drive frequency, namely the gain margin decreases. This problem is closely related to the maximum value for the proportional gain in the position control. This value is limited in the z-axis. Therefore the x-axis is forced to use a too low proportional gain, leading to a decrease in gain margin.

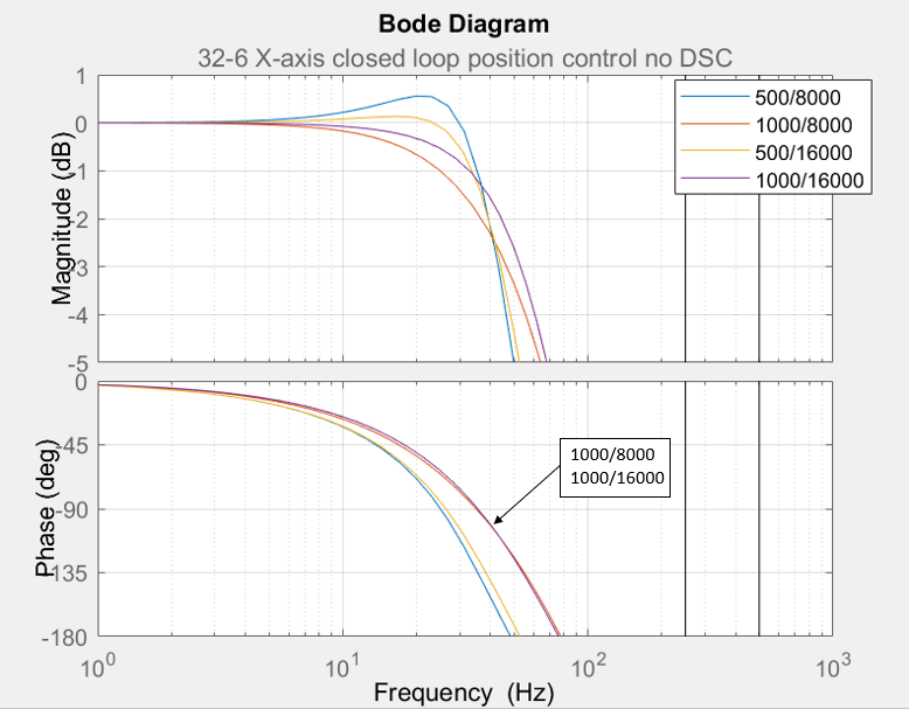

Figure 4.3: A bode diagram comparing the closed loop position control for different combinations of drive frequencies for a z-axis, position control drive frequency [Hz] / velocity control drive frequency [Hz]. The blue line represents the current configuration.

A next step in the optimisation process is to make some geometrical changes. It is desired to study the effect of an increased axial resonance frequency in the z-axis. This will be studied by increasing the diameter of the screw. In order to avoid a large decrease in the mass ratio, the lead is increased to 8 mm. (In both x- and z-direction.) The results are shown in fig. 4.3 (for the z-axis) and fig. 4.4 (for the x-axis). A few notable effects of this modification are:

1. The axial resonance frequency of the z-axis is increased.
2. The z-axis experiences more mechanical damping.
3. The axial resonance frequency of the x-slide and the z-slide are closer together.
4. The mass ratio in the x-axis has been increased.

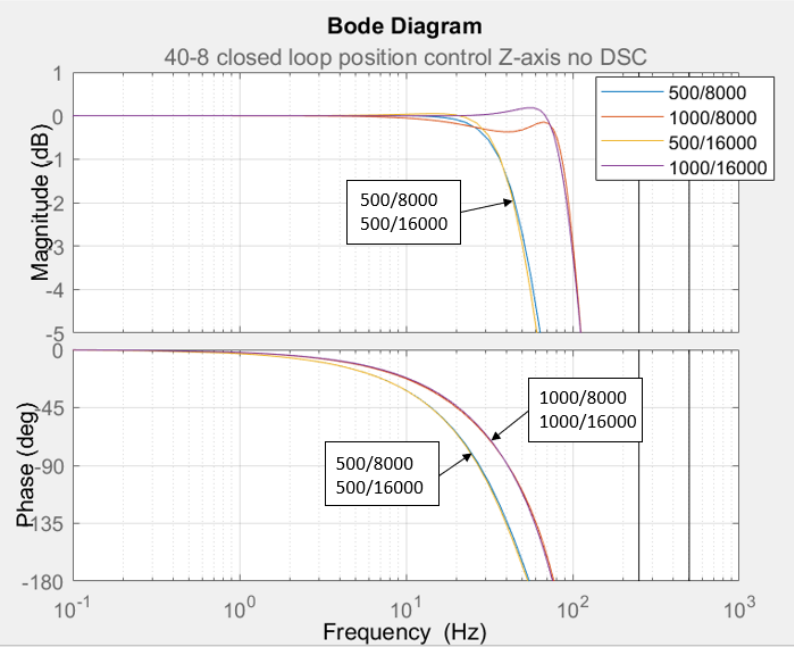

Figure 4.4: A bode diagram comparing the z-axis closed loop position control for different combinations of drive frequencies (position drive frequency [hz] / velocity drive frequency [hz]). The configuration is a 40 mm diameter screw with a 8 mm lead.

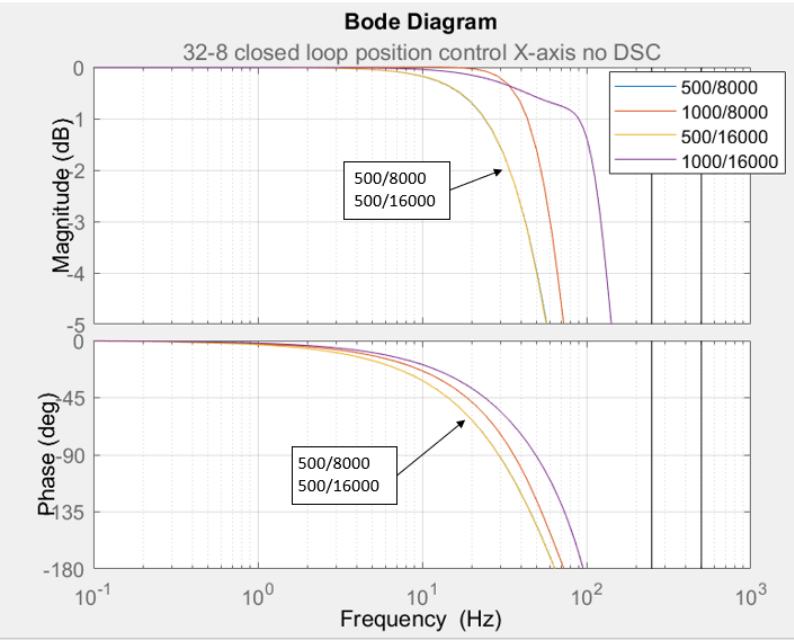

Figure 4.5: A bode diagram comparing the x-axis closed loop position control for different combinations of drive frequencies (position drive frequency [hz] / velocity drive frequency [hz]). The configuration is a 32 mm diameter screw with a 8 mm lead.

The increased axial resonance frequency of the z-axis has a small effect on the cut-off frequency. The shift in resonance frequency is small and due to the drive frequencies there is saturation. Another notable effect in the magnitude plot is that for the 1000 Hz position drive frequency the valleys and the peaks are much less sharp. For the x-axis it can be seen that for this configuration the increase in position drive frequency leads to an increase in the cut-off frequency. The z-axis is still a limiting factor for the proportional gain that can be used in the position control of the x-axis, but the effect has become smaller, because the resonance frequencies are closer together. However, at this point local peaks and valleys appear in the x-axis magnitude plot, the graph is no longer smoothly declining.

At this point the z-axis design will be frozen, and the x-axis will be optimized further. The closed loop bandwidth of the z-axis is roughly 60 percent of the axial resonance frequency. In literature percentages of around 50 percent are given as a maximum achievable closed loop cut-off frequency. [13] Therefore, this is an indication the possibilities for further optimisation are small. Studying the closed loop behaviour of the x-axis, the closed loop bandwidth of the x-axis is still smaller than the closed loop bandwidth of the z-axis, while the axial resonance frequency is larger. The limiting factor here is the proportional gain in the position control. It is desired to find a ballscrew drive geometry with the best performance given the limited proportional in the position control. Therefore, the axial resonance frequency of the z-axis and the x-axis will be brought further together by decreasing the diameter of the screw in the x-axis to 20 mm. The results are shown in fig. 4.6. It can be seen that lowering the axial resonance frequency of the x-axis may improve the closed loop behaviour, depending on de used drive frequencies.

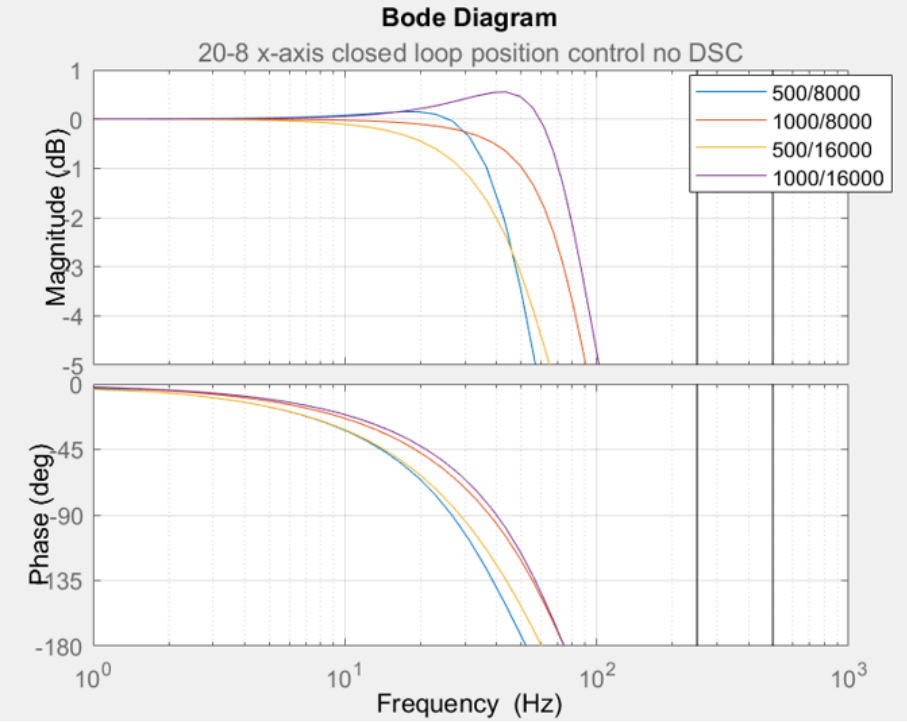

Figure 4.6: A bode diagram comparing the x-axis closed loop position control for different combinations of drive frequencies (position drive frequency [hz] / velocity drive frequency [hz]). The configuration is a 20 mm diameter screw with a 8 mm lead.

4.1.2. Dynamic stiffness control active

As a first iteration step for active DSC the closed loop position control of the z-axis and x-axis will be studied for different drive frequencies. The results are shown in fig. 4.7 and fig. 4.8.

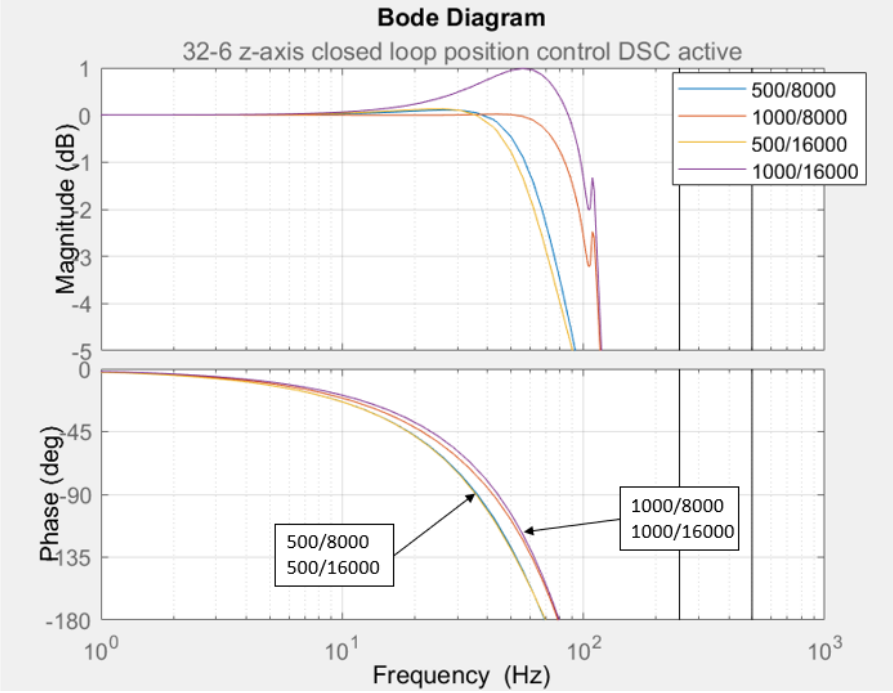

Figure 4.7: A bode diagram comparing the z-axis closed loop position control for different combinations of drive frequencies (position drive frequency [hz] / velocity drive frequency [hz]). The configuration is a 32 mm diameter screw with a 6 mm lead.

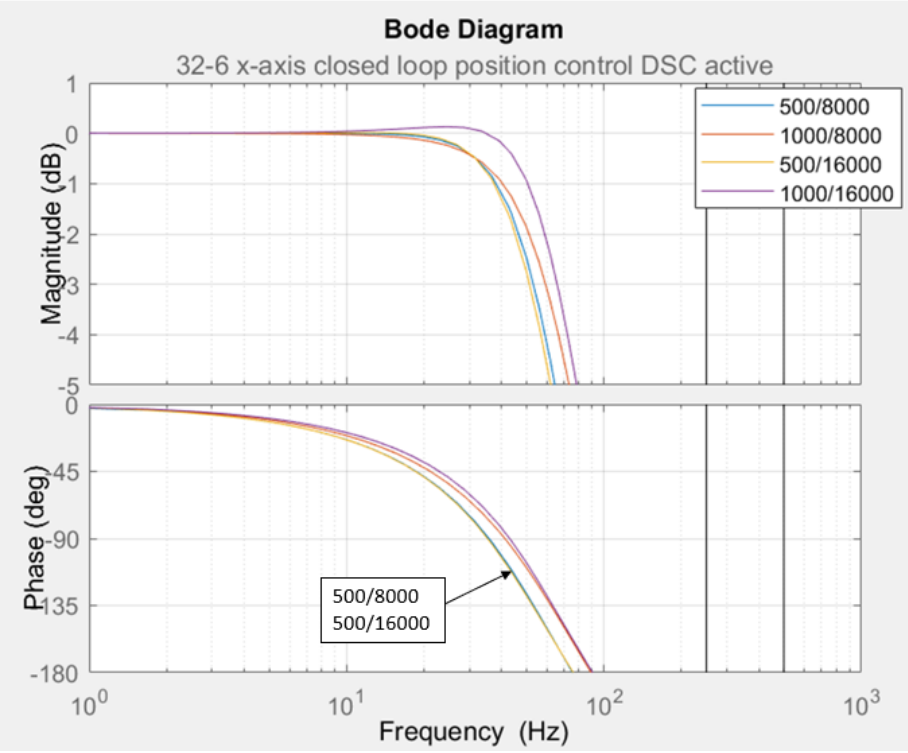

Figure 4.8: A bode diagram comparing the x-axis closed loop position control for different combinations of drive frequencies (position drive frequency [hz] / velocity drive frequency [hz]). The configuration is a 32 mm diameter screw with a 6 mm lead.

Applying active DSC allows for an increased proportional gain in the position control and for an increased phase margin. Applying active DSC often causes undesired peaks in the magnitude plot. Selecting control parameters in the speed controller very properly, the magnitude of these peaks can be minimized. Also, a notch filter could be used to damp the peak. As a drawback, a notch filter causes a decrease in phase margin. As an illustration to indicate what happens when active DSC control is applied with near-optimal control parameters, fig. 4.9 shows what happens. To continue the iteration process, an increased lead in combination with a larger diameter screw in the z-axis will be studied. This is similar to the previous subparagraph. The results are shown in fig. 4.10 for the z-axis and in fig. 4.11 for the x-axis.

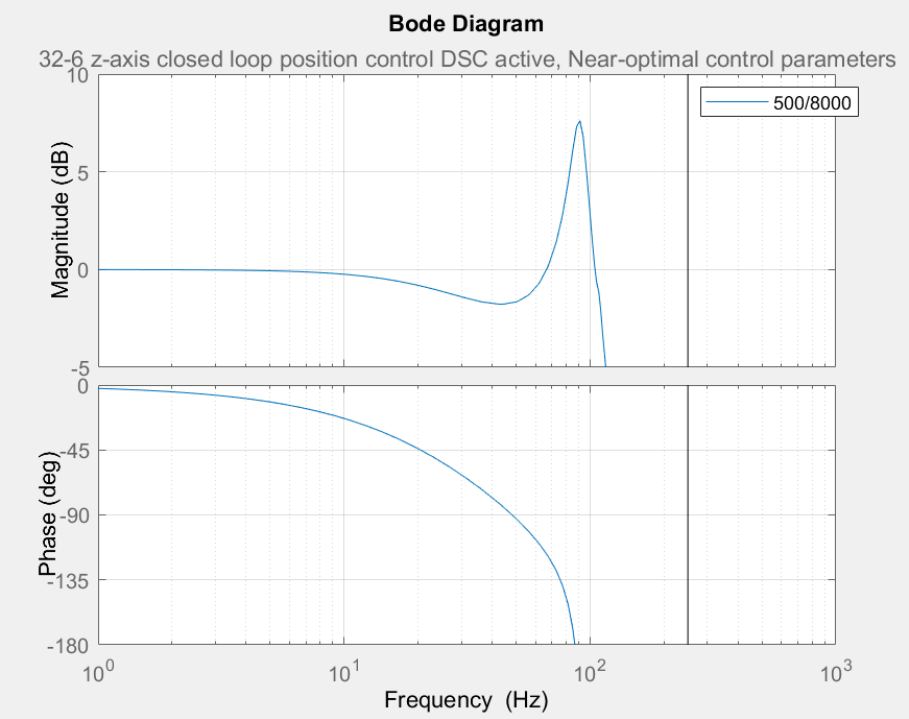

Figure 4.9: A bode diagram of a z-axis with a 32 mm diameter screw and a 6 mm lead. The drive frequencies are 500 Hz in the position control and 8000 Hz in the speed control. Using active DSC with near-optimal control parameters causes sharp peaks in the magnitude plot.

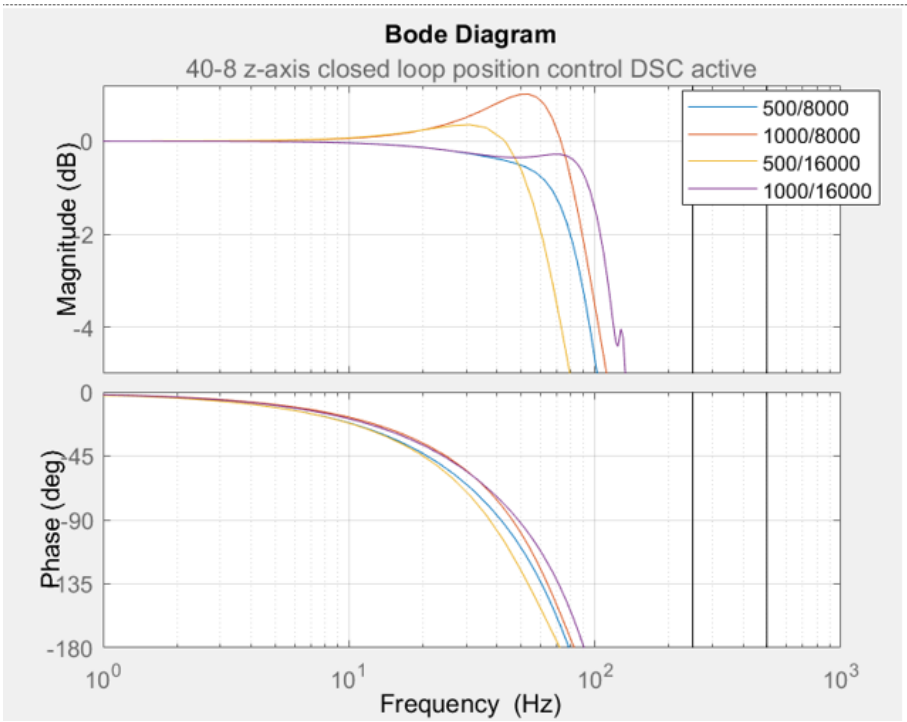

Figure 4.10: A bode diagram comparing the z-axis closed loop position control for different combinations of drive frequencies (position drive frequency [hz] / velocity drive frequency [hz]). The configuration is a 40 mm diameter screw with a 8 mm lead. The configuration in purple has the highest cut-off frequency of all studied z-axis configurations.

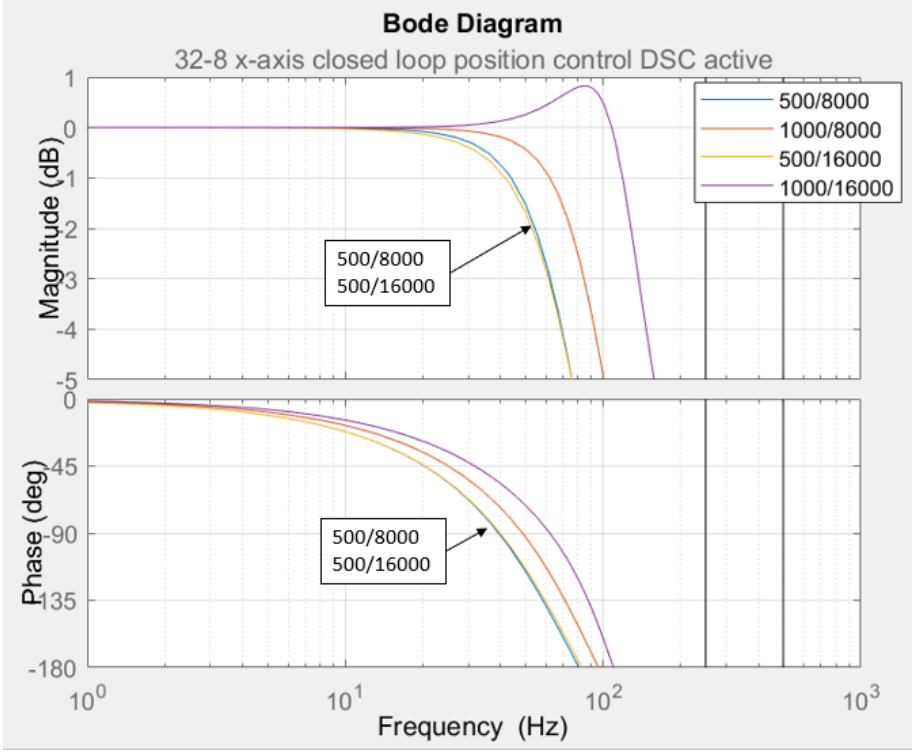

Figure 4.11: A bode diagram comparing the x-axis closed loop position control for different combinations of drive frequencies (position drive frequency [hz] / velocity drive frequency [hz]). The configuration is a 32 mm diameter screw with a 8 mm lead. The configuration in purple has the highest cut-off frequency of all studied x-axis configurations.

The results for the z-axis are quite similar to the previous iteration, the cut-off frequency slightly

increased due to the increased axial resonance frequency. The behaviour of the x-axis significantly improved due to the x- and z-axis axial resonance frequencies which are close together.

Therefore, the z-axis design will be frozen at this point and the x-axis will be optimized further by studying the effect of bringing the axial resonance frequencies of the x-axis and z-axis closer together by decreasing the diameter of the screw of the x-axis. The results are shown in fig. 4.12.

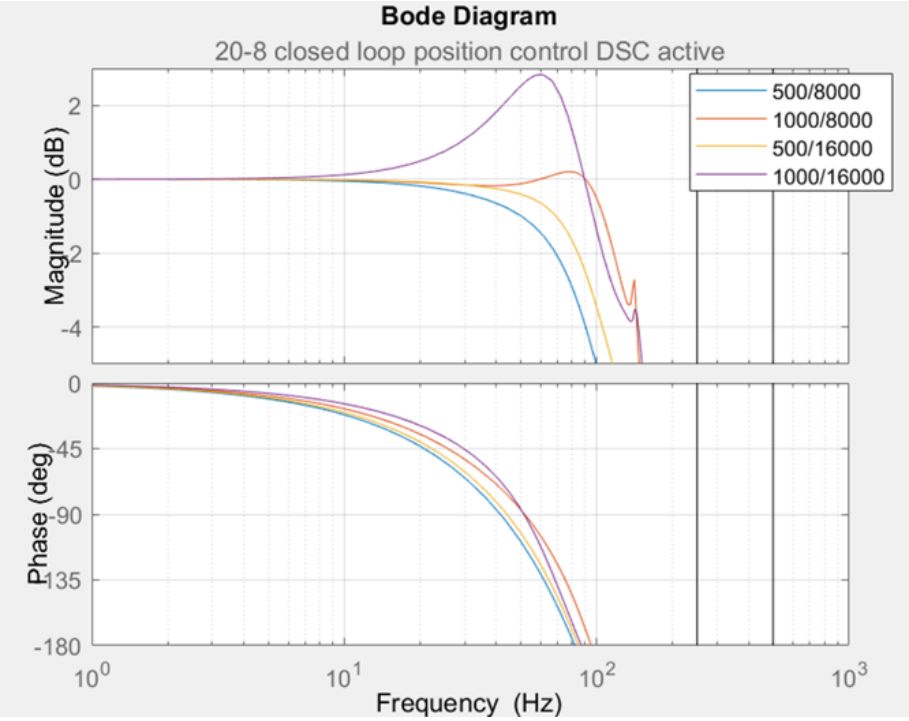

Figure 4.12: A bode diagram comparing the x-axis closed loop position control for different combinations of drive frequencies (position drive frequency [hz] / velocity drive frequency [hz]). The configuration is a 20 mm diameter screw with a 8 mm lead.

4.1.3. Performance summary of the evaluated concepts

For a good comparison, table 4.1 provides a summary of the performance of all evaluated concepts.

A reasonable design improvement could be a configuration with active DSC and drive frequencies of 1000 Hz (position control) and 16 kHz (speed control) in combination with a screw diameter of 40 mm in the z-axis and 32 mm in x-axis with a lead of 8 mm (both axis). The usable frequency bandwidth in z-axis could be improved from 50 to 90 Hz and in the x-axis the usable frequency bandwidth could be improved from 40 to 110 Hz.

					No DSC		Active DSC	
	screw diameter [mm]	lead [mm]	position drive freq [Hz]	speed drive freq [kHz]	cut-off freq [Hz]	smoothly declining	cut-off freq [Hz]	smoothly declining
z-axis	32	6	500	8	50	yes	70	yes
			1000	8	70	no	80	no
			500	16	50	yes	70	yes
			1000	16	70	no	80	no
x-axis	32	6	500	8	40	no	50	yes
			1000	8	40	yes	60	yes
			500	16	40	no	50	yes
			1000	16	50	yes	70	no
z-axis	40	8	500	8	50	yes	80	yes
			1000	8	80	no	80	no
			500	16	50	yes	70	no
			1000	16	80	no	90	no
x-axis	32	8	500	8	40	yes	60	yes
			1000	8	60	yes	90	yes
			500	16	40	yes	60	yes
			1000	16	90	yes	110	no
x-axis	20	8	500	8	50	yes	80	yes
			1000	8	70	yes	90	no
			500	16	50	yes	80	yes
			1000	16	70	no	90	no

Table 4.1: A summary of the performance of the closed loop position control of the evaluated concepts. The control is characterized by the cut-off frequency and by indicating if the magnitude plot declines smoothly. The current configurations are marked in yellow. The configurations with the highest closed loop position control usable frequency bandwidth are marked green.

4.2. Performance comparison for different configurations

To show the increased performance in setpoint tracking of the previously described adjustments a case study will be performed. The performance of two x-axis configurations will be compared, the properties of the configurations are given in table 4.2. The control parameters for both configurations have been optimized for response around the 30 Hz region. This is different compared to paragraph 4.1 where the control parameters have been optimised for a full frequency range e.a. a frequency range from zero up to half the drive frequency. The error that will be studied is the error related to the 'slow' dynamic response of the slides. Any other errors, for example discrepancy between movement of the turning tool with respect to the slide, disturbances and sensor error are not taken into account.

	configuration 1	configuration 2
Screw diameter [mm]	32	32
Screw lead [mm]	6	8
Drive frequency position control [Hz]	500	1000
Drive frequency speed control [Hz]	8000	16000
Use of DSC	no	no

Table 4.2: The properties of the two configurations that will be compared for the setpoint tracking.

The case study that will be performed is eccentric turning. An artist impression of the desired workpiece geometry is shown in fig. 4.13.

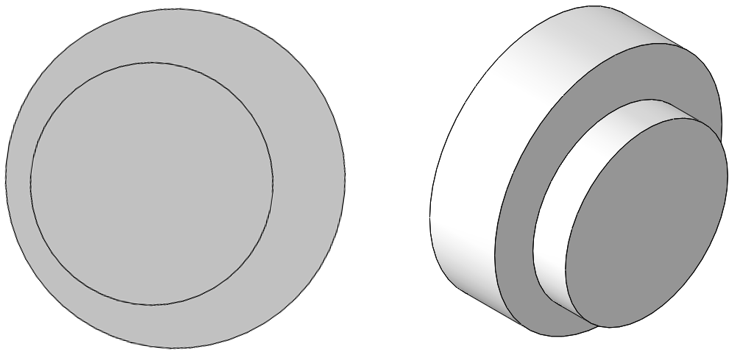

Figure 4.13: A CAD model of an eccentric workpiece geometry. The left figure shows a top view, the right figure shows an isometric view.

The workpiece is clamped on the large diameter circle. The axis of rotation of the workpiece is the axis of the cylinder of the large diameter. The focus for the comparison is the manufacturing of the small cylinder on top of the large cylinder. It is assumed the small cylinder has a radius R of 5000 μm. The axis of the small cylinder and the axis of the large cylinder are parallel, but spaced with a distance d of 100 μm. Assuming constant angular velocity of the workpiece, the position setpoint P(t) for the x-axis as a function of time and angular velocity ω [rad/s] is given in eq. 4.3.

$$P(t) = -d\cos(\omega t) + \sqrt{R^2 - d^2\sin^2(\omega t)} \tag{4.3}$$

The setpoint tracking will be studied for an angular velocity of 188 rad/s (1800 rpm). It has been checked that the maximum slide acceleration remains below the maximum of 4 m/s^2. For the comparison the discrepancy between slide movement and turning tool movement is not taken into account. First the setpoint tracking as a function of time will be studied. The results are shown in fig. 4.14. Comparing configuration one with configuration two, a clear improvement in amplitude can be seen. Considering the phase, there is still a delay. The delay in phase is closely related with the control strategy, which controls the position only proportional. The delay is reduced because the increased position drive frequency allows for a higher control parameter for the position proportional gain. The setpoint tracking can also be characterized with a polar plot, where the radius of the circle is plotted as

a function of angular position, the results are shown in fig. 4.15. Fig. 4.15 has been created neglecting error between the spindle position setpoint and the spindle actual position.

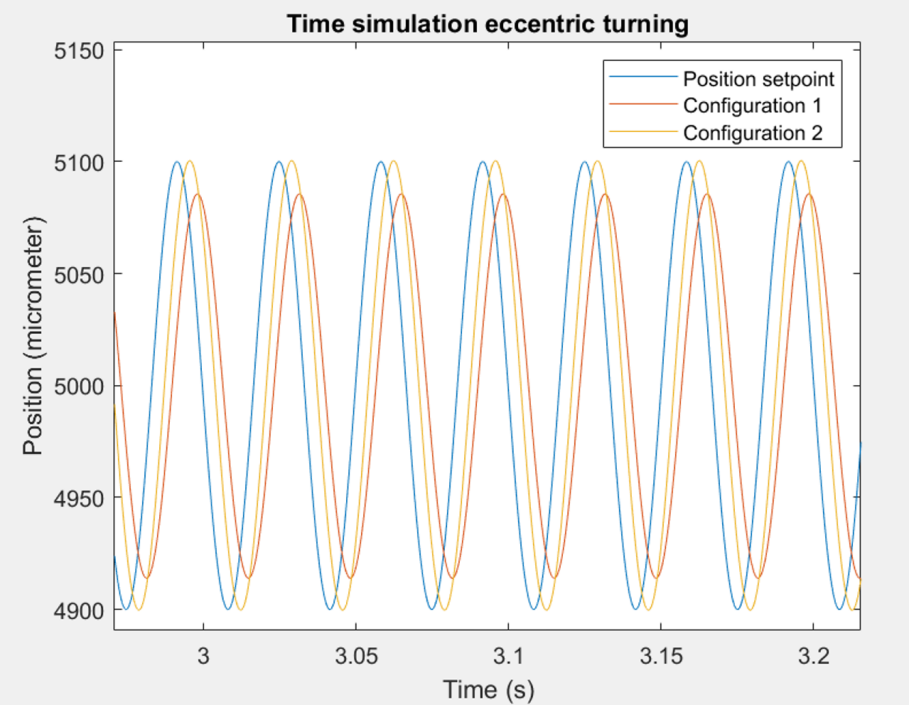

Figure 4.14: A time domain setpoint tracking simulation comparing configuration one with configuration two.

Fig. 4.15 will be studied further by applying a least square circle fit on the contours realized with configurations 1 and 2. The results of the circle fit are given in table 4.3.

	position setpoint	configuration 1	configuration 2
Radius [μm]	5000	4999.868	5000.0037
Radius error [μm]	0	0.132	0.0037
Midpoint position x-direction [μm]	-100	-26.13	-70.98
Midpoint position y-direction [μm]	0	-81.75	-70.97
Midpoint angular position [deg]	180	252.3	225.0
Eccentricity [μm]	100	85.82	100.37
Peak-peak maximum roundness error [μm]	0	0.244	0.10

Table 4.3: A summary of the circle fit parameters of configuration 1 and 2.

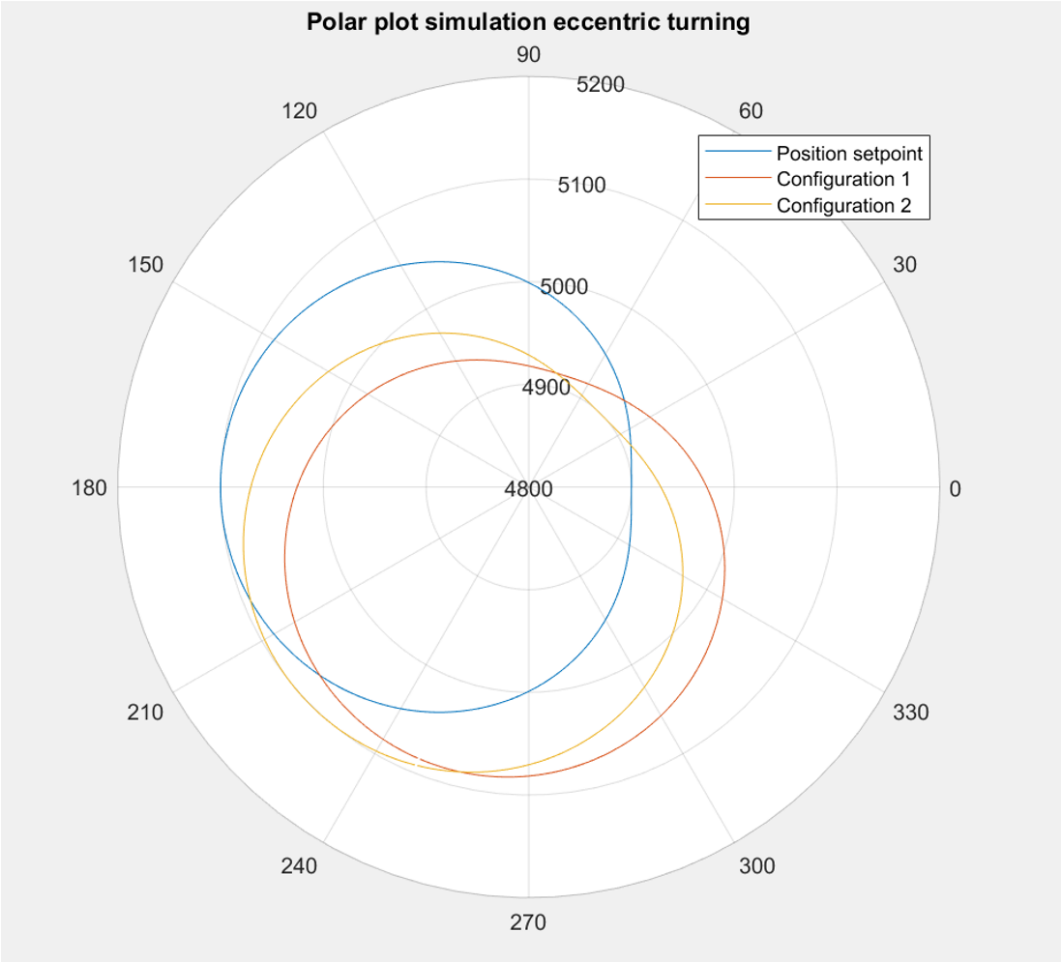

Figure 4.15: A polar plot conparing the setpoint tracking of configuration one with configuration two.

The distribution of the roundness error for a full circle is given in fig. 4.16.

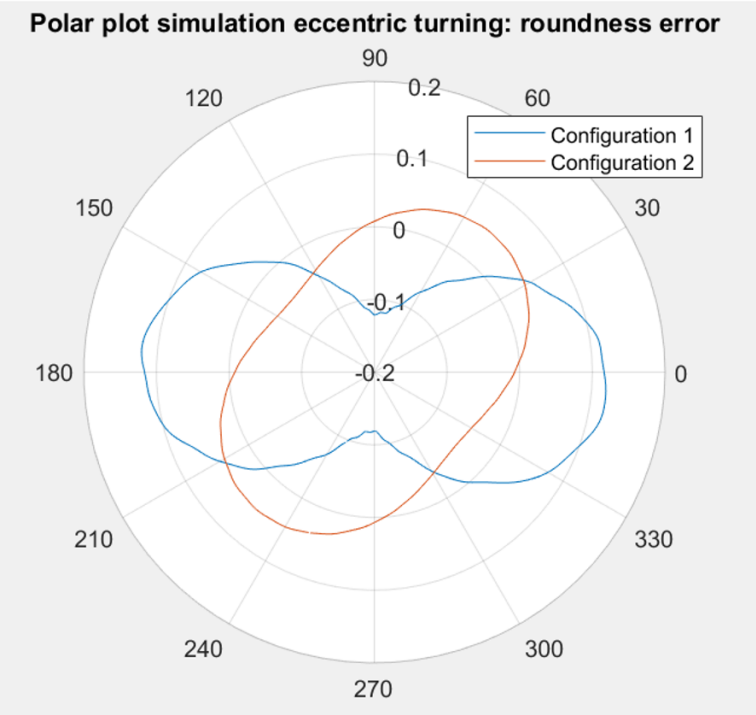

Figure 4.16: The roundness error of configuration one and configuration two.

4.3. Quasi-static behaviour and disturbance rejection

For the quasi static behaviour (positioning accuracy) it is important to study the effect of the relative accuracy of the rotary encoder. In principle, increasing the lead causes an increased error in relative accuracy. However, the dynamics and the error distribution of the rotary encoder make it more complicated. As explained in the Simulink model, the signal of the Heidenhain rotary encoder will first be differentiated using an Euler backward algorithm before it is send back as a feedback signal. The rotary encoder measures the angular position of the motor shaft in two steps. [20] As a first step a full revolution is divided into signal periods. An artist impression of the distribution of the error of one signal period is shown in fig. 4.17. The error within one revolution will always be in between -a and +a. a is usually expressed in microradians.

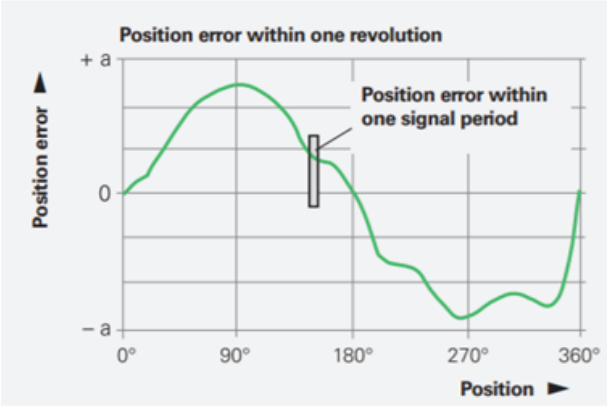

Figure 4.17: An artist impression of a typical position error within one revolution. [20]

During the second measurement step interpolation will take place within the signal period. An artist impression of the error within one signal period is shown in fig. 4.18. The error is always in between -u and +u. Usually u is 1 - 3 percent of the signal period.

For the quantification of the relative error in the context of a varying lead and varying drive frequen-

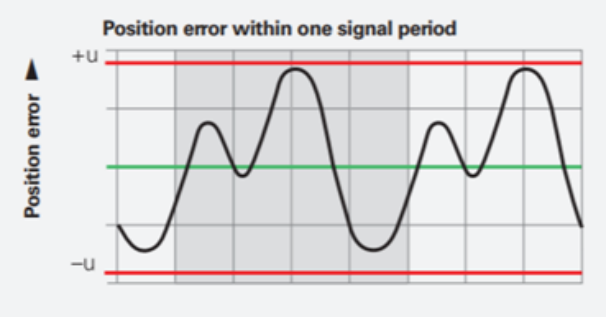

Figure 4.18: An artist impression of a typical position error within one signal period. [20]

cies, a number of considerations are important.

1. When the lead increases, the rotary speed of the screw for a given slide velocity decreases. The difference in angular position between two subsequent measurement points decreases. Finally, the error in the calculated velocity decreases.

2. Similar to the previous item, an increased drive frequency in the velocity control causes the angular position between two subsequent measurement points to decrease, causing a smaller error in the feedback signal of the velocity control.

Unfortunately, the commercial catalogues of Heidenain do not provide information of the first derivative of figures 4.17 and 4.18. Therefore, the influence of a varying lead and drive frequency on the (low frequency) position accuracy can not be quantified.
For the load side disturbance rejection a transfer from disturbing force [N] towards displacement [m] will be calculated. For optimal disturbance rejection this transfer should go to 0 in absolute values for all frequencies, or to minus infinity expressed in decibels. For a good understanding, table 4.4 provides a conversion between the decibel scale and absolute values.

Value (dB)	Value ($\mu m/N$)
-140	0.1
-160	0.01
-180	0.001

Table 4.4: (Dynamic) compliance conversion between decibels [dB] and absolute values [μm/N] for selected values

The disturbance rejection of the z-axis will be studied for two concepts, namely the 32-6 configuration and the 40-8 configuration. The results are shown in fig. 4.19. It can be seen that for the low frequency range the 40-8 configuration is slightly worse than the 32 - 6 configuration. Although the screw is stiffer, the increased lead requires a decreased proportional gain in the position control, therefore, the 40-8 configuration rejects low frequency disturbances slightly worse. Also due to the low proportional gain in the position control of the 40-8 configuration the is the tendency to follow the plant anti-resonance frequency more closely than the 32-6 configuration. Around the axial resonance frequency, the peak of the 32-6 configuration is much higher than the peak of the 40-8 configuration. After the axial resonance frequency the drive becomes dynamically very stiffness after a certain threshold, for example two times the axial resonance frequency, disturbances will not disturb the slide any more (until the next (torsional) resonance frequency). It can be seen that the threshold becomes higher.

For the x-axis also two configurations are shown. The 32-6 configuration and the 20-8 configuration can be found in fig. 4.20.

Using active DSC and / or higher drive frequencies usually allows for the use of a slightly higher proportional gain in the position control. These effect are quite small. For low disturbing frequencies the rejection improves and the tendency to follow the plant anti-resonance frequency becomes smaller.

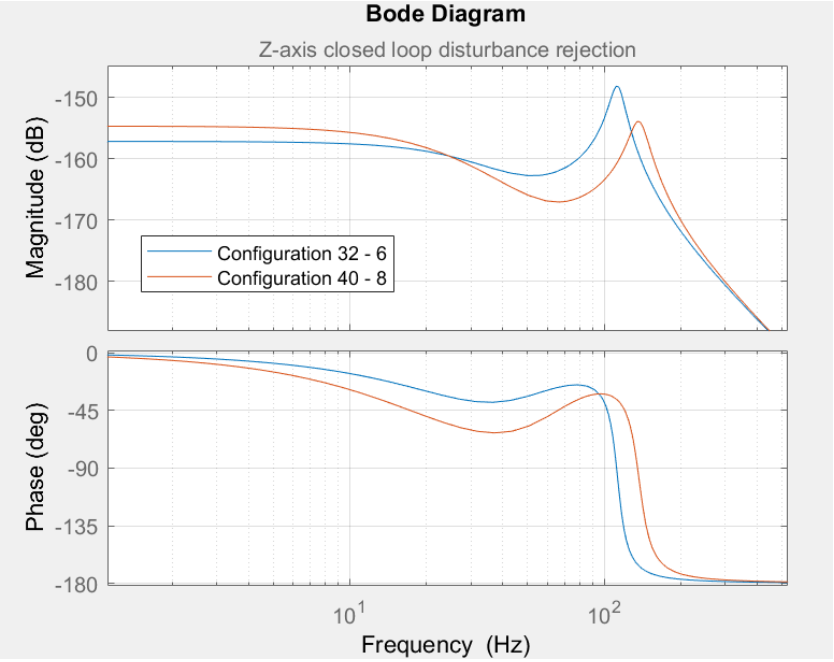

Figure 4.19: Closed loop disturbance rejection for a Z-axis with drive frequencies 500 Hz (position loop) and 8000 Hz (velocity loop).

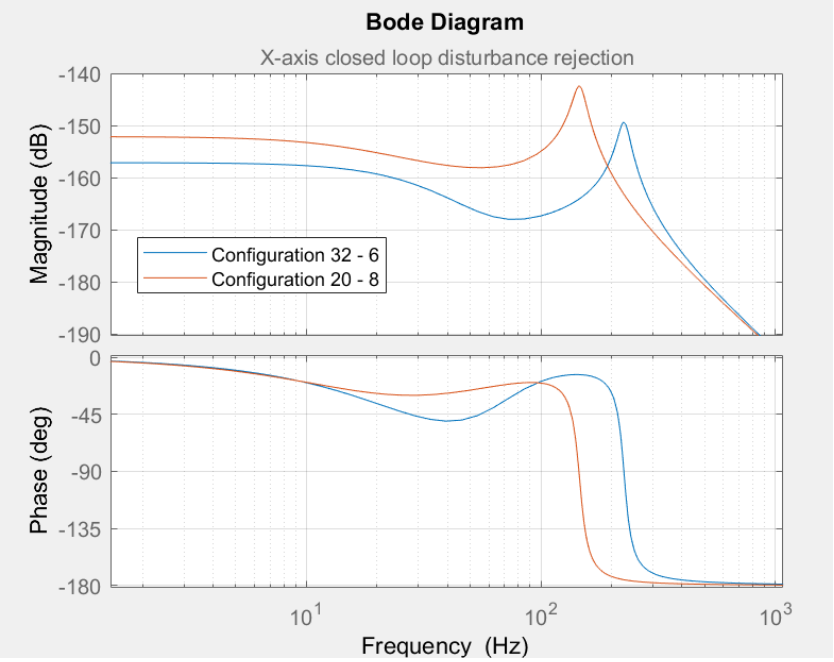

Figure 4.20: Closed loop disturbance rejection for a x-axis with drive frequencies 500 Hz (position loop) and 8000 Hz (velocity loop).

5

Conclusions and recommendations for future work

The subject of this thesis is the dynamic behaviour of a slide assembly consisting of two orthogonal ball-screw drives stacked on top of each other used in a CNC controlled hard turning machine. The slides assembly allow for linear movement of a turning tool in two directions.

The most important resonant frequencies are the axial modes, the first and second torsional modes of the screws and a bending mode of the cover plate. The eigenmodes are determined both experimentally and numerically. Subsequently, transfer functions are formulated. Starting at a motor current, the transfer functions determine response at the motor axis, at the slide and at the turning tool.

Implementing the control elements, the closed loop control of a hard turning machine can be modeled.

It has been shown that the usable frequency bandwidth can be improved by (1) increasing the lowest axial resonance frequency, (2) bringing the axial resonance frequencies of the two axis closer together, (3) increasing the lead and (4) increasing the drive frequencies. In the x-axis (lateral), the usable frequency bandwidth could be improved from 40 to 110 Hz, in the z-axis (axial) the usable frequency bandwidth could be improved from 50 to 90 Hz. Also, the influence on the disturbance rejection has been studied.

5.1. Future work

With this thesis a design cycle for optimal stacked ball-screw drives design is proposed. Executing this cycle, several concepts have been proposed and its pro's and con's have been discussed. There is a possibility for future work to closely study the effect of an increasing lead on the quasi-static performance. Improving the dynamic behaviour is in many proposed designs based on an increase of the lead, but the effect of the increased lead on the quasi-static behaviour is not fully understood. A next step could be to manufacture (one of) these concepts and experimentally verify the results. There are also possibilities for future work to go (fully) automatically through the design cycle to gain more insight in how (combinations of) design changes influence the performance. Code that could automatically create designs, evaluate its (closed loop) performance and eventually come up with a new design to go again through the cycle will likely have the potential to greatly speed up the design process and more clearly predict the influence of design changes on the performance. Several design objectives and variables could be included.

So far only optimisation for general purposes has been discussed. When selecting the geometry of a specific workpiece to be machined an optimal design could be created for optimal setpoint tracking.

For the calculation of closed loop control and setpoint tracking this thesis remained to the classical P-PI control strategy. Although this control strategy is the most widely used strategy for ball-screw drive control, there is likely a great potential for more advanced control. For example higher order or non-linear controllers, making use of acceleration, jerk and snap feedback and using feed-forward controllers. Filters could be used to suppress noise in a feedback loop. Specific values could be

artificially limited, for example current, jerk and acceleration. Also setpoint filtering may offer a potential for improving control.

In this thesis it has been shown that above certain frequencies the linear encoder (at the slide) is no longer a good representation for the movement of the turning tool. There are possibilities for future (experimental) work to better understand the relationship between the position of the slide and the position of the turning tool. One approach could be to create a new design with the goal to minimise the difference between movement of the slide and movement of the turning tool. This implies that the mass and the geometry of the slides and its attached components become design variables. Another approach would be to compensate for the discrepancy in the control, requiring very good knowledge about the discrepancy between slide movement and turning tool movement, possibly in combination with the use of an extra sensor.

When optimising disturbance response, the model in this thesis could be used to select optimal spindle frequencies. Also control parameters could be selected to optimise disturbance response, for example by maximally taking advantage of the load-side anti-resonance frequency.

6

Self-reflection

When I started my thesis project in September 2019 it became clear that the dynamics of the slides-assembly is a very broad research topic. My first attempt to narrow the research topic was to focus on the mechanics and not so much on the control. However, this was no success since the performance of a turning machine is determined by the combination of the mechanics and the control. Fortunately, just in time I discovered the field of ball-screw drive dynamics which provided a useful starting point.

The formulation of the finite element model was challenging. Especially the connection of the different components of the turning tool changer was difficult since the manufacturer did not include a full detail CAD-model in the documentation. After manually decomposing a turning tool changer and measuring all it's components, it took a lot of effort to discover how the rigidity of all connections was created. Modelling the screws as a linear spring may be a problematic simplification, since the structural resonance frequency and the torsional modes are not in the model with this simplification.

Apart from the finite element model a Simulink model was also created. The Simulink model only considers response at the machine shaft and at the slide in axial direction. This is a clear limitation of the Simulink model, but certain design changes can be implemented very easily and the computational time is in the order of seconds. The finite element model considers response at a wide variety of locations and in combination with the substructuring a great number of design changes can be evaluated. However, the finite element model is much more complicated and the computational time is in the order of an hour. The combination of the simulink model and the finite element model was powerful to model complex behaviour (for example response at the turning tool in the y-direction) but it also allowed for a quick evaluation of small design changes, for example varying the drive frequencies.

The developed modelling tools easily produce a large amount of data. Structuring these data and presenting them in an organized fashion could have been better.

Apart from the theoretical side and statically studying a turning tool changer, also experimental dynamic work has been done, which was fun! By creatively using machine functions the dynamic behaviour of the slides has been studied. I think the good correlation between experimental data and theoretical models is a strong aspect of the thesis.

The last part of the thesis that tries to find an optimal design could be much more automated, allowing for a larger number of iterations. At this moment the iterations are based on increasing the axial resonance frequency and the drive frequencies while maintaining a lower bound for the mass ratio and the lead. However, the iterations could be much more advanced.

The contact with my supervisors, both my TU-supervisor as well as my company supervisor was regular and useful. For the Dynamics of Micro- and Nanostructures (DMN) group the project was slightly irregular, since most of the DMN research is focused on the micro- and nanoscale. For Hembrug Machine Tools the dynamics of the slides was a mostly unexplored field of research.

A

Accelerometer response

For all 72 electromechanical shaker experiments a frequency spectrum has been calculated. The tables below provide the full extrated data. The frequency f has corresponding units of [Hz] and the response A has corresponding units of $[(mm/s^2)/(Nm)]$

1A	1B	1C
f_1 = 203 A_1 = 1999	f_1 = 203 A_1 = 1830	f_1 = 203 A_1 = 1762
f_2 = 375 A_2 = 522	f_2= 371 A_2= 590	f_2 = 371 A_2 = 698
f_3 = 883 A_3 = 5814	f_3 = 879 A_3 = 5941	f_3 = 879 A_3 = 5341
1D	1E	1F
f_1 = 203 A_1 = 2346	f_1 = 203 A_1 = 2215	f_1 = 203 A_1 = 2139
f_2 = 375 A_2 = 469	f_2 = 371 A_2 = 537	f_2 = 371 A_2 = 571
f_3 = 883 A_3 = 6492	f_3 = 879 A_3 = 5955	f_3 = 879 A_3 = 5598
1G	1H	1I
f_1 = 203 A_1 = 2356	f_1 = 199 A_1 = 2337	f_1 = 199 A_1 = 2337
f_2 = 375 A_2 = 469	f_2 = 371 A_2 = 532	f_2 = 371 A_2 = 635
f_3 = 883 A_3 = 5600	f_3 = 879 A_3 = 6008	f_3 = 879 A_3 = 5482

Table A.1: Results measurement serie 1 (x-motor to x-slide)

2A	2B	2C
f_1 = 203 A_1 = 2866	f_1 = 207 A_1 = 2636	f_1 = 203 A_1 = 2560
f_2 = 375 A_2 = 1108	f_2= 375 A_2= 1158	f_2 = 371 A_2 = 1252
f_3 = 883 A_3 = 23596	f_3 = 879 A_3 = 25424	f_3 = 879 A_3 = 25595
2D	2E	2F
f_1 = 203 A_1 = 3308	f_1 = 203 A_1 = 3134	f_1 = 203 A_1 = 3066
f_2 = 375 A_2 = 967	f_2 = 375 A_2 = 971	f_2 = 371 A_2 = 948
f_3 = 879 A_3 = 27176	f_3 = 879 A_3 = 23292	f_3 = 879 A_3 = 24167
2G	2H	2I
f_1 = 203 A_1 = 3275	f_1 = 199 A_1 = 3253	f_1 = 199 A_1 = 3284
f_2 = 375 A_2 = 827	f_2 = 375 A_2 = 897	f_2 = 371 A_2 = 1015
f_3 = 879 A_3 = 25706	f_3 = 879 A_3 = 23959	f_3 = 879 A_3 = 24363

Table A.2: Results measurement serie 2 (x-motor to turning tool x-direction)

3A	3B	3C
f_1 = 203 A_1 = 992	f_1 = 207 A_1 = 876	f_1 = 207 A_1 = 920
f_2 = 879 A_2 = 81035	f_2= 879 A_2= 66168	f_2 = 879 A_2 = 69463
3D	3E	3F
f_1 = 203 A_1 = 1063	f_1 = 203 A_1 = 1153	f_1 = 203 A_1 = 1015
f_2 = 879 A_2 = 72481	f_2 = 879 A_2 = 81506	f_2 = 879 A_2 = 71484
3G	3H	3I
f_1 = 203 A_1 = 1250	f_1 = 199 A_1 = 1271	f_1 = 193 A_1 = 1348
f_2 = 879 A_2 = 71401	f_2 = 879 A_2 = 74086	f_2 = 879 A_2 = 66224

Table A.3: Results measurement serie 3 (x-motor to tool y-direction)

4A	4B	4C
f_3 = 883 A_3 = 22586	f_3 = 883 A_3 = 21955	f_3 = 883 A_3 = 19665
4D	4E	4F
f_3 = 879 A_3 = 18018	f_3 = 883 A_3 = 18400	f_3 = 879 A_3 = 20615
4G	4H	4I
f_3 = 879 A_3 = 16863	f_3 = 879 A_3 = 15891	f_3 = 879 A_3 = 22472

Table A.4: Results measurement serie 4 (x-motor to turning tool z-direction)

5A	5B	5C
f_1 = 121 A_1 = 2589	f_1 = 129 A_1 = 2362	f_1 = 145 A_1 = 2693
		f_2 = 308 A_2 = 382
f_2 = 910 A_2 = 710	f_2= 910 A_2= 475	f_3 = 910 A_3 = 1555
5D	5E	5F
f_1 = 121 A_1 = 2747	f_1 = 129 A_1 = 2174	f_1 = 145 A_1 = 2484
		f_2 = 308 A_2 = 375
f_2 = 910 A_2 = 834	f_2 = 910 A_2 = 677	f_3 = 910 A_3 = 1438
5G	5H	5I
f_1 = 121 A_1 = 2654	f_1 = 129 A_1 = 2494	f_1 = 145 A_1 = 2516
		f_2 = 308 A_2 = 352
f_2 = 910 A_2 = 831	f_2 = 907 A_2 = 513	f_3 = 910 A_3 = 1781

Table A.5: Results measurement serie 5 (z-motor to z-slide)

6
The spectrum contains only very low peaks, with a dominant role for noise.

Table A.6: Results measurement serie 6 (z-motor to turning tool x-direction)

7A	7B	7C
f_1 = 121 A_1 = 992	no data	f_1 = 145 A_1 = 1549
f_2 = 304 A_2 = 715	no data	f_2 = 308 A_2 = 1501
f_3 = 910 A_3 = 2710	no data	f_3 = 910 A_3 = 5581
7D	7E	7F
f_1 = 121 A_1 = 847	f_1 = 129 A_1 = 934	f_1 = 149 A_1 = 1431
f_2 = 304 A_2 = 685	f_2 = 304 A_2 = 874	f_2 = 308 A_2 = 1381
f_3 = 910 A_3 = 2284	f_3 = 910 A_3 = 4294	f_3 = 910 A_3 = 4533
7G	7H	7I
f_1 = 121 A_1 = 1087	f_1 = 129 A_1 = 1203	f_1 = 145 A_1 = 1819
f_2 = 304 A_2 = 560	f_2 = 304 A_2 = 817	f_2 = 308 A_2 = 1395
f_3 = 910 A_3 = 2466	f_3 = 910 A_3 = 2894	f_3 = 910 A_3 = 5278

Table A.7: Results measurement serie 7 (z-motor to turning tool y-direction)

8A	8B	8C
f_1 = 121 A_1 = 3239	f_1 = 129 A_1 = 3054	f_1 = 145 A_1 = 3806
f_2 = 910 A_2 = 1894	f_2 = 910 A_2 = 3054	f_2 = 910 A_2 = 3314
f_3 = 1852 A_3 = 1570		f_3 = 1868 A_3 = 1512
8D	8E	8F
f_1 = 121 A_1 = 3504	f_1 = 129 A_1 = 2904	f_1 = 145 A_1 = 3647
f_2 = 910 A_2 = 1289	f_2 = 910 A_2 = 2342	f_2 = 910 A_2 = 1902
f_3 = 1852 A_3 = 1780	f_3 = 1864 A_3 = 876	f_3 = 1868 A_3 = 1729
8G	8H	8I
f_1 = 121 A_1 = 3461	f_1 = 129 A_1 = 3413	f_1 = 145 A_1 = 3787
f_2 = 905 A_2 = 695	f_2 = 910 A_2 = 1765	f_2 = 910 A_2 = 1655
f_3 = 1852 A_3 = 2140	f_3 = 1864 A_3 = 925	f_3 = 1868 A_3 = 1358

Table A.8: Results measurement serie 8 (z-motor to turning tool z-direction)

Bibliography

[1] Function of tool features for face milling. http://www.mitsubishicarbide.com/en/technical_information/tec_rotating_tools/face_mills/tec_rotating_function_cutting_edge/tec_milling_function_cutting_edge_angle. online accessed 21 October 2019.

[2] Mechanics of metal cutting. https://slideplayer.com/slide/13333805/. online accessed 29 June 2020.

[3] Transfer function estimation. https://nl.mathworks.com/help/ident/ref/tfest.html/. online accessed 16 October 2019.

[4] Fluid bearing. https://en.wikipedia.org/wiki/Fluid_bearing. online accessed 17 October 2019.

[5] How to find the transfer function of a system. https://x-engineer.org/graduate-engineering/signals-systems/control-systems/find-transfer-function-system/. online accessed 16 October 2019.

[6] Torque ripple. https://en.wikipedia.org/wiki/Torque_ripple. online accessed 8 November 2019.

[7] M. Abu-Hilal. Forced vibrations of euler-bernoulli beams by means of dynamic green functions. *Journal of sounds and vibrations*, 267:191–207, 2003. doi: 10.1016/S0022-460X(03)00178-0.

[8] ABDELWAHAB ABDELKARIM H. Zhu H. Elkariem H. A. Ahmed, A. Modeling and analysis of three-degree of freedom regenerative chatter in the cylindrical lathe turning. *Viborengineering*, 2017.

[9] Golnaraghi M. F. Alkhatib, R. Active structural vibration control: A review. *The shock And Vibation Digest*, 35:367–383, 2003.

[10] Amin Alsolami. *Precision Control of High Speed Ball Screw Drives*. PhD thesis, University of Waterloo, 2008.

[11] Francisco Campa J. Ansoategui, I. Mechatronics of a ball screw drive using an n degrees of freedom dynamic model. *International journal of advanced manufactering Technology*, 93(1), 2017.

[12] S. Brouwer. Stijfheidsonderzoek hembrug 100 cnc. unpublished.

[13] Richiede D. Caracciolo, R. Optimal design of ball-screw driven servomechanisms through an integrated mechatronic approach. *Mechatronics*, 24, 2014.

[14] Zhang L. Man J. Chen, L. Effect of nominal chip thickness on stability of interrupted turning. *Advances in mechanical engineering*, 2014.

[15] Do Nascimentio L. A. D. dos Santos hoefel S. Da Silva, J. F. Free vibration analysis of euler bernoulli beams under non-classical boundary conditions. *Congresso nacional de engenharia mechanica*, August 21-25, 2016.

[16] Sencer B. Dumanli, A. Optimal high-bandwidth control of ball-screw drives with acceleration and-jerk feedback. *Precision engineering*, 54, 2018.

[17] L. Euler. De motu vibratorio laminarum elasticarum, ubi plures novae vibrationum species hactenus non pertractatae evolvuntur. *Novi Commentarii academiae scientiarum Petropolitanae*, 17:449–487, 1773.

[18] W. K. Gawronski. *Advanced Structural Dynamics and Active Control of Structures*. Springer Verlag, 2004. ISBN 0-387-40649-2.

[19] Lockwood S. Ford D.G. Haase, F. Vibration modelling in machine tool structures. *Transactions on Engineering Sciences*, 34:3533–3541, 2001.

[20] *Encoders for Servo Drives*. HAINDENHAIN, 2019.11 edition.

[21] Y. Hosseinkhani. *Control Methods for Improving Tracking Accuracy and Disturbance Rejection in Ball Screw Feed Drives*. PhD thesis, University of Waterloo, 2014.

[22] Buiting-Csikos Cs. Luttervelt van C.A. Moulijn K.A. Ponsen J. M. Streppel A.H. Kals, H.J.J. *Industriele productie*. Boom uitgevers, 2015. ISBN 978-90-395-2673-6.

[23] J. L. Lagrange. *Mechanique analytique*. Tome Premier, 1811.

[24] Stepan-G. Insperger T. Mann, B.P. Increased stability of low-speed turning through a distributed force and continuous delay model. *Journal of Computational and Nonlinear Dynamics*, 4:583–591, 2009.

[25] W.B. Rowe. *Hydrostatic, Aerostatic and Hybrid Bearing Design*. Butterworth-Heinemann, 2012. ISBN 978-0-12-396994-1.

[26] S. Pastorelli S. Mauro and E. Johnston. Influence of controller parameters on the life of ball screw feed drives. *Advances in mechanical engineering*, 7(8), 2015.

[27] Paurobally R. Siddhpura, M. A review of chatter vibration research in turning. *International journal of machine tool and manufacture*, August 27-47, 2012.

[28] *SINUMERIK 840D sl Servo Tuning with AST*. SIEMENS, 2019.03 edition, .

[29] *Sinumerik sinamics*. SIEMENS, .

[30] Agapiou A. S. Stephenson, D. A. *Metal cutting: theory and practise*. CRC press, 2016. ISBN 978-1-4665-8757-3.

[31] Maarten van der Seijs. *Experimental dynamic substructering*. PhD thesis, Delft University of Technology, 2016.

[32] Bond I. P. Waever M. Friswell Wagg, D. *Adaptive structures engineering applications*. Wiley, 2007. ISBN 978-0-470056-974.

[33] Zhang W. Xu Y.S. Zhang, Q. Identification method of structure transfer function for machine tools based on pseudo-random process. *Key Engineering Materials*, 315–316:366–369, 2006.